Variations of Solar Wind Parameters over a Solar Cycle: Expectations for NASA's Solar TErrestrial RElations Observatory (STEREO) Mission

Catherine C. Walker
Mount Holyoke College 2007
Department of Astronomy

Advisors:
Professor M. Darby Dyar
Department of Astronomy
Mount Holyoke College

Antoinette B. Galvin
Department of Physics
STEREO/PLASTIC Principal Investigator
Space Science Center
Institute for the Study of Earth, Oceans, and Space
University of New Hampshire

Mark A. Popecki
STEREO/PLASTIC Co-Investigator
Space Science Center
Institute for the Study of Earth, Oceans, and Space
University of New Hampshire

ACKNOWLEDGEMENTS

To start off, I would like to thank Dr. George Hurtt of the Complex Systems Center at the University of New Hampshire's Institute for the Study of Earth, Oceans, and Space for allowing me to have such a wonderful research opportunity through the UNH-NASA Research & Discover Program. It has become apparent to me that the experience and connections that I gained through this program have brought me closer to my goal than I thought I would be at this point in life!

In that vein, I need to express my sincere gratitude to Dr. Antoinette Galvin and Dr. Mark Popecki, first of all for taking me as a Research & Discover intern. Second, I need to thank them for allowing me to continue my research with them throughout the year, allowing me to become part of the UNH-PLASTIC team, flying me down to see the launch of STEREO, and accompanying me to the American Geophysical Union Fall meeting in San Francisco where I was able to present my research. Also, thanks are in order for the rest of the PLASTIC team, whom I had the pleasure of working with this past summer and school year. In addition, I also need to thank the rest of the folks in the Space Science Center at UNH for letting me take up desk space while I am there.

I would like to thank my advisor here at Mount Holyoke, Darby Dyar, for allowing me to complete my thesis on the Sun and the solar wind even though it's a bit unrelated to research that goes on here. I also need to thank her for reading all these pages many times! Thanks are in order for her constant help and friendly manner.

I also want to thank those who agreed to sit on my committee – Suzan Edwards, Shubha Tewari, and Tom Burbine – and apologize in advance for the excessive page number. They are very kind to offer their time as they have.

Lastly, I need to thank my family and friends. My parents, Cheryl and George, and my sister, Cynthia, have always been very supportive of my education and research, even when it means driving to and from New Hampshire multiple times in one day, driving to various different airports in the small hours of the morning, or listening endlessly to presentation rehearsals. I know that they have given me every chance to succeed. I would like to thank my supportive friends at Mount Holyoke, who help out even when they're too busy to sleep, and my friends from UNH and the Research & Discover Program, for proving to me that the scientists are the cool kids. I look forward to meeting more of these inspiring individuals in the future.

CONTENTS

CHAPTER 1

INTRODUCTION

The solar wind is composed of plasma that flows outward from the Sun into the heliosphere. Plasma consists of energetic particles, or electrically charged gas. The heliosphere is the bubble created by the solar wind that travels with the Sun through interstellar space – it includes everything that is under the influence of the Sun. This bubble extends far past the orbits of the planets in the solar system. At some point within the heliosphere, the solar wind speeds drop (producing a sonic boom) as the effects of the interstellar wind predominate. This is called the termination shock. Finally, there is a boundary at which the pressure of the solar wind is equal to that of the interstellar winds; there, the solar wind is stopped completely and flows back into the tail of the heliosphere. This boundary is the heliopause, or, more accurately, the interstellar boundary. Past this point is interstellar space. As the heliosphere moves through interstellar space, it causes a buildup of particles in front of it – much like water building up around a boulder in the middle of a stream. This is called the bow shock. The man-made object that has traveled farthest into this region is NASA's Voyager 2. It is currently in the heliosheath, where interstellar gas and solar wind start to mix. It took Voyager 2 almost thirty years to approach the end of the Sun's influence in

space.[i] Because the boundary is defined by the solar wind, then in turn, it fluctuates in position as the solar wind varies in strength. This leads to the question: how does the solar wind change over time?

In fact, the solar wind varies with a noticeable pattern every 11 years. Since the solar wind is a product of the Sun, it follows the solar cycle; the solar cycle is 11 years (i.e. 11 years between peaks). Early astronomers who noted the changing numbers of sunspots that appeared on the Sun first observed the solar cycle. At any given time, there would be many spots; a few years later, significantly fewer spots; and a few years after that, there would be many once again. These variations in sunspot numbers indicate the level of solar activity. At solar maximum, the Sun is covered in sunspots and is very active; at solar minimum, the Sun lacks sunspots and is relatively dormant. The most recent solar minimum occurred in 1996, and the most recent solar maximum occurred in 2001. The upcoming solar minimum is set for early 2007.

There are three types of solar wind, each of which is present at all stages of solar activity. These types are fast solar wind, slow solar wind, and transient solar winds. Fast solar wind has speeds of approximately 600 to 800 km/s, whereas slow solar wind has speeds of approximately 200 to 600 km/s. Transient solar winds contain several sub-categories of solar wind, for instance Coronal Mass Ejections (CMEs), which are sudden ejections of a large amount of radiation from the Sun's corona, and Solar Energetic Particle events (SEPs), in

which particles are emitted during solar activity and travel up to 90% of the speed of light.

Not only does the solar wind affect the location of the interstellar boundary, but it also interacts with the planets as it travels past them. Because the Earth has a magnetic field, the electrically charged plasma traveling outward from the Sun can affect the Earth quite magnificently. The most visible of these interactions between the solar wind and the Earth's magnetic field are the aurora borealis and the aurora australis. Also, because of satellite locations, the solar wind can greatly affect satellite communications, and can limit the possibilities for human spaceflight, especially outside of the Earth's protective magnetic field. The magnetic field can be greatly disrupted by the solar wind, causing geo-magnetic storms and sub-storms in the magnetosphere.

The Solar Terrestrial Relations Observatory (STEREO) is the latest of NASA's Solar Terrestrial Probes missions.[1] Like other missions before it, for instance the Solar and Heliospheric Observatory (SOHO), the Advanced Composition Explorer (ACE), and Cluster, the STEREO mission is designed to orbit the Sun and study the Earth-Sun connection. Unlike these past missions, however, the STEREO mission consists of not one, but two nearly-identical satellites that will orbit the Sun from Earth-orbital distance at the same time – one observatory will lead the Earth (orbit in front of the Earth), the other will trail it (orbit behind the Earth). Prior to STEREO, there have only been two-dimensional

[1] STEREO Official Mission Website, http://stereo.gsfc.nasa.gov/

images of the Sun. For the first time, data will be collected from two locations simultaneously, creating the first-ever three-dimensional views of the Sun. The purpose of STEREO is to study the solar wind at Earth's orbit. Particularly crucial to the STEREO mission will be its observations of coronal mass ejections, whose origins, as of yet, are unknown.

Each STEREO observatory (called STEREO-A and STEREO-B) carries four instrument packages. The first package is the Sun-Earth Connection Coronal and Heliospheric Investigation (SECCHI), which has an Extreme Ultraviolet Imager (EUVI), two white light coronagraphs (COR1 and COR2), and the Heliospheric Imager (HI). The STEREO/WAVES (SWAVES) instrument is an interplanetary radio burst tracker. The third instrument package is the *In-situ* Measurements of Particles and CME Transients (IMPACT), which carries six instruments that will provide measurements of the solar wind plasma and local magnetic field: the Solar Wind Electron Analyzer (SWEA), the Suprathermal Electron Telescope (STE), a Magnetometer (MAG), the Solar Electron Proton Telescope (SEPT), the Suprathermal Ion Telescope (SIT), a Low Energy Telescope (LET) and an High Energy Telescope (HET). Finally, the Plasma and SupraThermal Ion Composition Investigation (PLASTIC), the instrument that is the focus of this thesis, will provide plasma characteristics of protons, alpha particles, and heavy ions. It will provide measurements of mass and charge state composition of heavy ions, and also differentiate between the CME plasma and the ambient solar wind.

The purpose of this thesis is to investigate the relationships between the ambient solar wind, the transient solar wind, and the solar cycle. It examines the variations in the solar wind over an entire solar cycle using results from previous solar missions spanning 11 years. Also, these data will be used to predict space weather conditions that will be met by the STEREO spacecraft after it launches into solar minimum in the fall of 2006.

CHAPTER 2

BACKGROUND: The Science of the Sun

There are many parts of the Sun and solar environment that must be discussed prior to the presentation of results based on solar wind data. For instance, what is the wind made of? Where does it come from? These questions must be answered and understood before any further discussion can progress. The first four sections of this background chapter focus on the Sun itself – its composition, structure, its variable magnetic field, and features of its corona, which becomes relevant later in the discussion of solar wind. The next section focuses on the types of solar wind and their origins, whether these origins are proven or theoretical. Following this discussion, section six aims to describe the Sun-Earth connection and the role of the solar wind in that relationship. The last two sections of the background section will cover NASA's Solar TErrestrial RElations Observatory (STEREO) mission and the PLasma And SupraThermal Ion Composition (PLASTIC) instrument, which is the focus of this thesis, and past solar missions that paved the way for STEREO observations.

2.1. SOLAR COMPOSITION

The composition of the solar wind is, of course, strongly related to the composition of the Sun. The most common elements in the Sun are shown in Table 1.

Element	Parts per million Hydrogen atoms
Hydrogen	1,000,000
Helium	98,000
Oxygen	850
Carbon	360
Neon	120
Nitrogen	110
Magnesium	40
Iron	35
Silicon	35

Table 1. This table show the most common elements in the Sun compared to the most common element, hydrogen.

As shown, hydrogen makes up for approximately 94% of all atoms.[ii] As a light element, however, it only makes up for about 72% of the mass of the Sun. A note should be made here that these data are for the Sun overall; in reality, different sections, or layers, of the Sun have different chemical abundances. In order to illustrate the composition of the solar wind, an overview of the interior structure of the Sun is useful.

2.2. SOLAR STRUCTURE

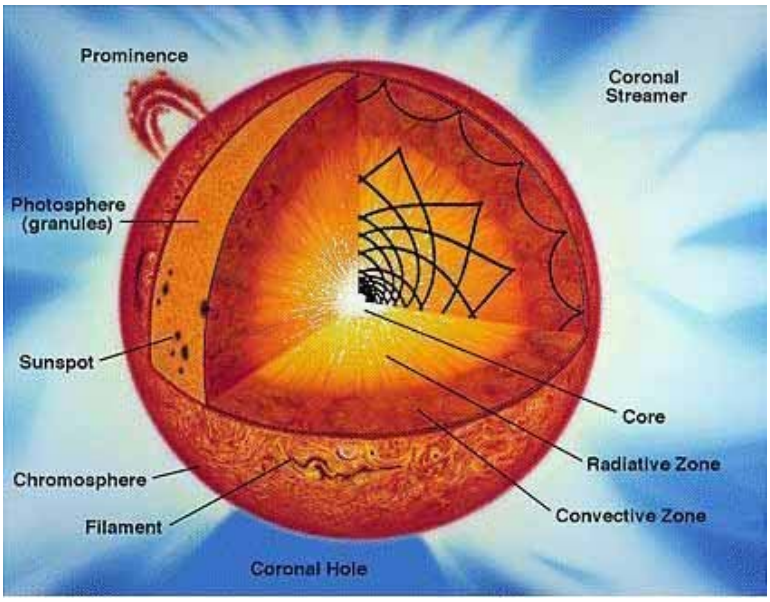

Figure 1. A diagram of the sections of the interior of the Sun.[2]

The interior of the Sun, shown in Figure 1, cannot be directly observed. To study the interior, scientists would have to observe its emergent radiation; however, no measurable radiation emerges from the solar interior due to the extreme brightness and temperatures of the photosphere.[iii] The basic structure of the Sun can be described in layers of varying activity.

The *core* of the Sun reaches out to approximately one quarter of the way to the surface. All of the nuclear fusion that takes place in the Sun occurs here in the core. The core is very dense, almost 15 times the density of lead (approximately 150 grams per cubic centimeter), and because of this, although it only encloses about two percent of the Sun's total volume, it holds almost half of

[2] Image credit: "The Sun Acts Up", B. Giles, NASA GSFC, http://pwg.gsfc.nasa.gov/istp/outreach/actsup.html

the Sun's mass. The pressure inside the core, which keeps the Sun from collapsing, is close to two hundred billion times the pressure at Earth's sea level.

Outside of the core is the *radiative zone*, which encircles the Sun's mass to within seventy percent of the distance to the surface. The radiative zone holds forty-eight percent of the Sun's mass. Although the radiative zone is made up of stable gas, there is a large temperature and density gradient across it. At the bottom of the zone, the density can be as high as twenty-two grams per cubic centimeter, with temperatures at about eight million Kelvin. At the top of the radiative zone, these measurements shrink to approximately two-tenths of a gram per cubic centimeter and two million Kelvin, respectively. The radiative zone gets its name because of the way the energy from the core radiates through it. Although the photons of energy from the core pass through stable layers of gas in the radiative zone, it can take up to one million years for the photon to pass through the zone, due to the high density particles with which they collide.

The *convection zone* begins where the radiative zone ends, and extends to the Sun's surface; it is the outermost layer of the Sun's interior. It holds the largest volume of the interior of the Sun – approximately 66% , but only two percent of the Sun's mass. At the surface, the density of the convection zone is very close to zero, with a temperature of about 5800 K. Photons traveling outward from the radiative zone heat the convective cells within this region and cause these cells to boil to the top of the convective zone. There are two types of convection cells on the Sun's surface: granulation cells, which are approximately

one-thousand kilometers in diameter, and supergranulation cells, which are approximately thirty-thousand kilometers in diameter.

The Sun's atmosphere, like its interior, also consists of layers. The lowest layer of the atmosphere, just above the convection zone, is *the photosphere*. This is the part of the Sun that emits the light seen on Earth. This section is approximately 500 km thick, although most of the light emanating from the Sun comes from the first 100 km. Often, scientists consider this to be part of the Sun's surface. The temperature of the photosphere ranges from 6400 K at the bottom to 4400 K at the top. The photosphere, although consisting of trillions of individual particles, also has extremely low density at only about one-millionth of a gram per cubic centimeter. The photosphere is made up of granules that lie atop of the granulation cells of the convective zone. These granules are typically visible for fifteen to twenty minutes before dissipating.

The second layer of the Sun's atmosphere is the *chromosphere*. The chromosphere is somewhat less understood than other sections of the Sun, because it is not easily visible. It can only be observed during an eclipse of the Sun, and even then, only for a few seconds – its spectrum, for this reason, is called *the flash spectrum*. From observations, scientists have concluded that the chromosphere is made up of spicules, which are spike-shaped features measuring approximately 1000 km wide and up to 10,000 km high. The main characteristic of the chromosphere is its high temperatures, which jump up from the relatively

cool photosphere to temperatures between ten-thousand and twenty-thousand Kelvin.

Between the chromosphere and the corona, the outermost layer of the Sun, is a thin layer called the *chromosphere-corona transition region*, or just the *transition region*. This region serves as a buffer between the hot chromosphere and the extremely hot corona. The transition region receives most of its energy from the corona, and emits the majority of its energy in the ultraviolet.

The outermost layer of the Sun is called *the corona*. In this discussion of the solar wind, the corona is the focus of solar surface studies, since it is the source of the solar wind. The corona's temperatures soar to above 500,000 K – in some areas close to the solar surface, temperatures can be as high as 6 million K, whereas in active regions, like solar flares, temperatures can reach astronomically high into the tens of millions of Kelvins. The corona consists of structures like loops and streams of ionized gas. These structures are shaped by the magnetic fields of the Sun. Temperatures vary greatly between sections of the corona.

Due to the extreme heat of the corona, the region continually expands. This outflow of hot solar gases is called *the solar wind*. In essence, the solar wind is a continuation of the Sun's atmosphere throughout the region of space previously referred to as *the heliosphere*. Within the corona, the density of particles ranges from one-million to one-billion particles per cubic centimeter,

whereas in the solar wind, the density ranges between ten and one-hundred particles per cubic centimeter.[3]

The solar wind in and of itself is a complex structure with many variants and contributing factors. The elements most commonly found in the solar wind were described by Meyer in 1985 as follows: hydrogen, helium, oxygen, neon, silicon, argon, and iron[iv]. These heavy ions are also joined by suprathermal ions and alpha particles to complete the makeup of the solar wind.

2.3. THE SOLAR MAGNETIC FIELD

A simplified view of a dipole magnetic field is shown in Figure 2.

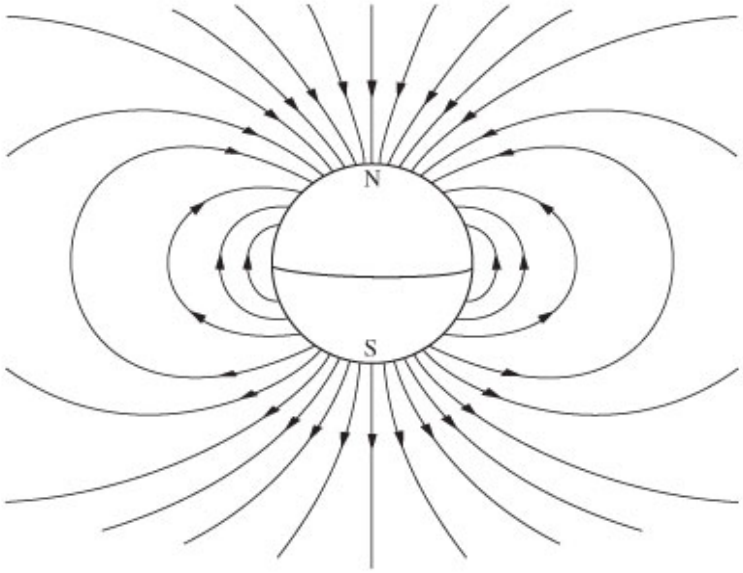

Figure 2. This figure shows a "normal" dipole magnetic field, such as the Earth's magnetic field. This is *nearly* the state of the solar magnetic field at solar minimum.[4]

[3] The density of the solar wind ranges between ten and one-hundred particles per cubic centimeter at Earth orbit, 1 AU.
[4] Image credit: "A Brief Introduction to Geomagnetism", United States Geological Survey, 2005.

The magnetic fields of the Sun play a dominant role in the solar cycle. Sunspots are locations of strong magnetic fields, and other features in the outer layers of the atmosphere (e.g. solar flares) are also associated with the fields. Like other bodies with a magnetic field, the Sun's field is caused by the dynamo mechanism. By this action, the kinetic energy of an electrically conducting matter is converted to magnetic energy. The Sun is made up of plasma, which is a highly charged conducting gas with freely moving electrons, protons, and ions. A byproduct of such a highly conducting body is that any magnetic field present is "frozen" into the plasma, and so when the plasma moves, the field must move along with it. Swedish Novel laureate Hannes Alvén first introduced this concept. It has been shown that certain motions of the plasma within the Sun can create much larger fields than the original field implanted within it, and thus, the Sun's interior acts as a dynamo.[v]

The outer parts of the Sun experience differential rotation. The inner portions may also experience this, but because these sections (as discussed previously) are not observable, we know that at least the outer layers of the Sun rotate at different velocities. That is, the angular velocity W is dependent upon the solar latitude φ_0.[vi] The equatorial regions rotate faster than the polar regions – this is because the solar surface is not rigid. Unlike Earth and the other rocky planets, the Sun is gaseous, and therefore not held together in uniform motion. This differential motion twists and magnifies the magnetic fields of the Sun. The

torsional oscillations, or differential velocities of the Sun's rotation, are shown in Figure 3.

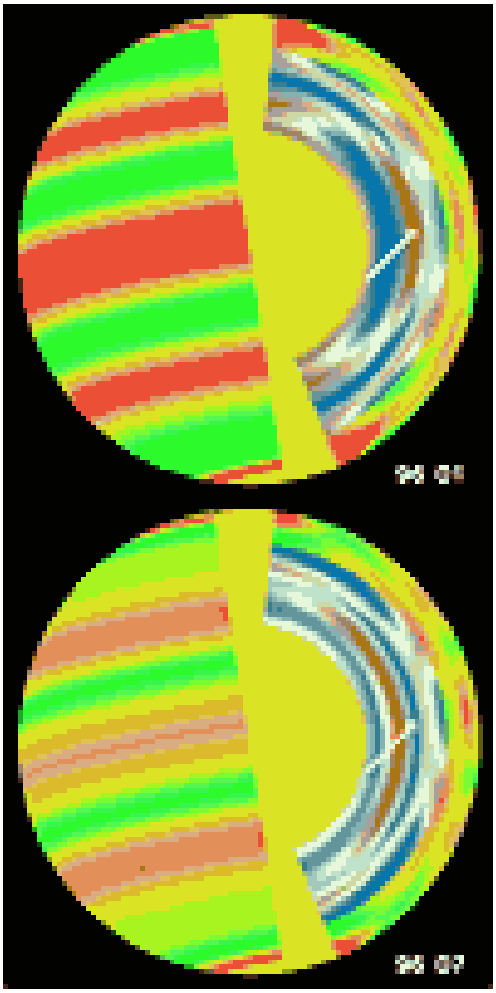

Figure 3. These cutaway images show snapshots of the changing solar rotation at two different times about six months apart, on the surface (left side of images) and below the solar surface. Near the surface the rotation is faster than average in the red areas and slower in the green; deeper down red indicates faster than average rotation and blue indicates slower rotation.[5] [vii]

There have been many theories proposed about the operation of the solar dynamo mechanism, to aid in explaining how a field that starts with lines of force parallel

[5] Image credit: Leibacher, J. NOAO/NSO Newsletter, June 2000, Number 62

to lines of longitude (called a *poloidal* field) changes to a field with lines of force oriented parallel to lines of latitude (called a *toroidal* field), which are exemplified in Figure 4.

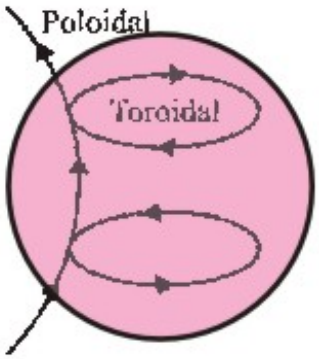

Figure 4. This is a simple figure showing a poloidal field line (in the north-south direction) and toroidal field lines (in the east-west direction).[6]

The generally accepted model of this process was suggested by H.W. Babcock in 1961, and has since been modified by R.B. Leighton and others.[viii] The Babcock model begins with the postulate that at some point in time, the Sun's magnetic field is poloidal (i.e. magnetic field lines only in the north-south direction). The differential rotation of the Sun causes the plasma at the equator to rotate faster than that at the poles, and as such, the magnetic field at the equator rotates equally as fast, due to the field lines being "frozen" in the plasma, as proposed earlier by Alvén. Because of this motion, the Sun develops a toroidal component of the magnetic field, and the magnetic field strength is increased.

[6] Image credit: Meert, J., "Is the Earth's Magnetic Field Young?", 08/2004, http://gondwanaresearch.com/hp/magfield.htm

Observationally, Babcock noted that every 3 years, the Sun's equatorial magnetic field rotates 5.5 more times than the magnetic fields at the poles. This result is illustrated in Figures 5a through 5c.

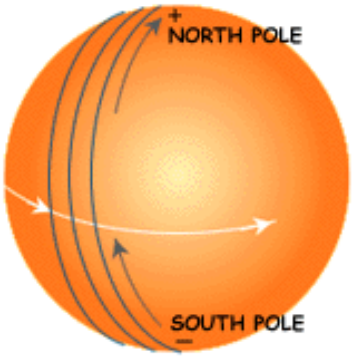

Figure 5a. At the start of the solar cycle, field lines are poloidal, in the north-south direction. The Sun's equator rotates faster than the poles, and here that is signified by the horizontal arrow across the equator.

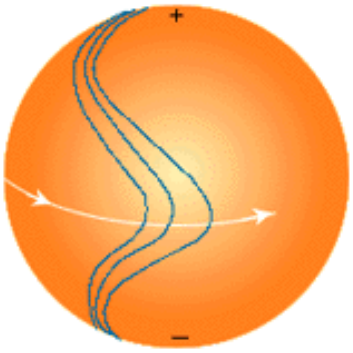

Figure 5b. As the equator regions rotate faster, the field lines attached to these regions bend and stretch with this differential movement and begin to become toroidal.

Figure 5c. As the rotational difference between the poles and the equatorial region increases, the magnetic field lines become increasingly horizontal, or toroidal.[7]

When this toroidal magnetic field becomes sufficiently stretched and twisted, it erupts to the surface and forms active regions, which are visible as sunspots. The peak in sunspot activity is called the solar maximum. As the solar cycle declines, opposite polarities migrate towards the poles and equator, and eventually begin to neutralize each other's polarities. The Sun then returns to a relatively poloidal field, and this is called solar minimum. At solar minimum, polarity is concentrated at the north and south poles. This new poloidal field, however, has the opposite polarity as the poloidal field seen at the previous solar minimum. Thus, the rising phase of the solar cycle is referred to as the period in which magnetic field lines are increasingly twisted and perturbed. The declining phase of the solar cycle is the period when the Sun sheds its perturbed magnetic field and begins its journey back to the "normal" poloidal field.

[7] Image credit: Transition Region and Coronal Explorer (TRACE) mission, Lockheed Martin Solar and Astrophysics Labs, Dr. Neal Hurlburt, Educational Resources, "The Sun's Magnetic Personality", http://trace.lmsal.com/

Although the Babcock model does not completely explain the processes of the Sun during the solar cycle - for instance, the process of deep fields erupting to the surface - it has been the most successful in accounting for much of the observed solar activity within the solar cycle. It successfully explains the Hale-Nicholson Polarity Law, which describes the east-west components of the magnetic polarities of sunspots. The sunspot polarity law states that active regions tend to be bipolar, with one magnetic polarity predominantly at the leading edge of the region and the other polarity predominantly at the trailing edge, and that the leading polarity in the northern hemisphere is the opposite that of the leading polarity in the southern hemisphere.[ix] This is typically called a bipolar sunspot group.[x] These groups can either be concentrated regions of polarities right next to each other, or regions of one polarity followed closely by a region of the opposite polarity. The Michelson Doppler Imager (MDI) magnetogram instrument on the Solar Heliospheric Observatory (SOHO) mission currently studies sunspot polarity. An example of sunspot polarity as imaged by the MDI instrument is shown in Figure 6.

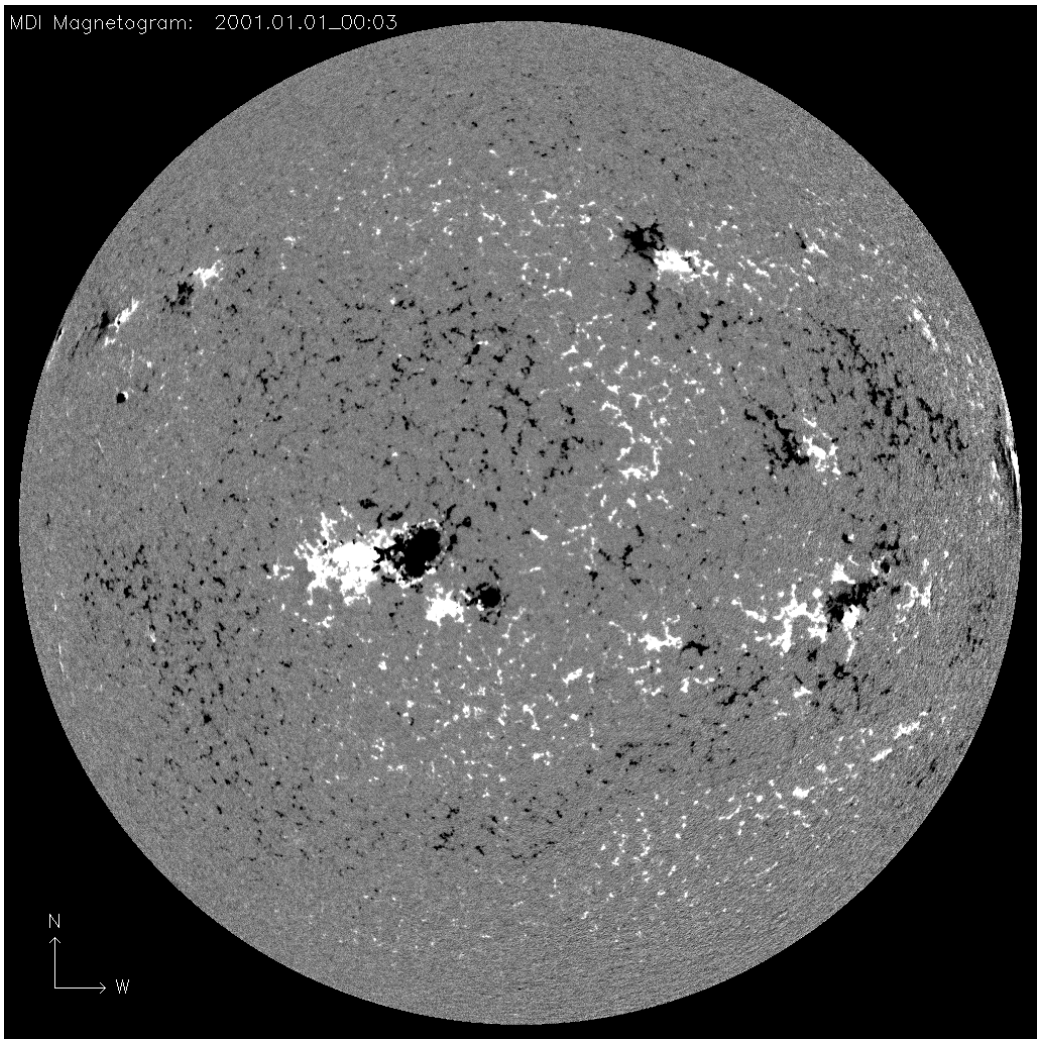

Figure 6. This image from the MDI magnetogram instrument on SOHO shows the opposite polarities of various sunspots, and also less-organized regions of polarities, followed by regions of the opposite regions. In this image, white regions are magnetic field lines extending out of the Sun, black regions are magnetic field lines that are going into the Sun. This image is from January 2001, during the most recent solar maximum.[8]

The Babcock model is also successful in explaining Spörer's law of spot migration. As the field lines with maximum strength (i.e. those that have been extremely contorted) move towards the equator, the sunspots also appear to migrate towards the equator around solar maximum. As the polarized spots travel

[8] Image credit: SOHO/MDI, Stanford-Lockheed Institute for Space Research

towards the equator, they neutralize upon contact with opposite polarities.[xi] The Babcock model is generally the most accepted model because of its success in modeling the visible solar cycle.

Richard Carrington, an amateur astronomer between 1853 and 1861, made many observations of the Sun and sunspot cycle. He measured sunspot latitudes and longitudes with remarkable precision, and although these measurements have since been updated, the notion of the Carrington longitude of the Sun is still in use today. The solar longitude system has no convenient zero point, like the Greenwich meridian on Earth, and so Carrington measured the movements of sunspots and eventually adopted the period of 25.38 days as the rotation time for the Sun on its axis. In reality, sunspots at the equator rotate around the Sun in about 25 days, and spots at the poles rotate in about 27 days. However, as the Earth revolves around the Sun, it appears from Earth that sunspots take a small amount of time longer to revolve around the Sun. Relative to fixed stars, the so-called sidereal period is 25.38 days, whereas one Carrington rotation relative to observers on the Earth becomes 27.28 days, which is called the synodic period.[xii]

The 11-year cycle of the Sun causes changes in all regions of the Sun. However, the variations in the solar corona over the solar cycle are of specific interest to studies of the solar wind. Figure 7 shows the changing Sun over the solar cycle.

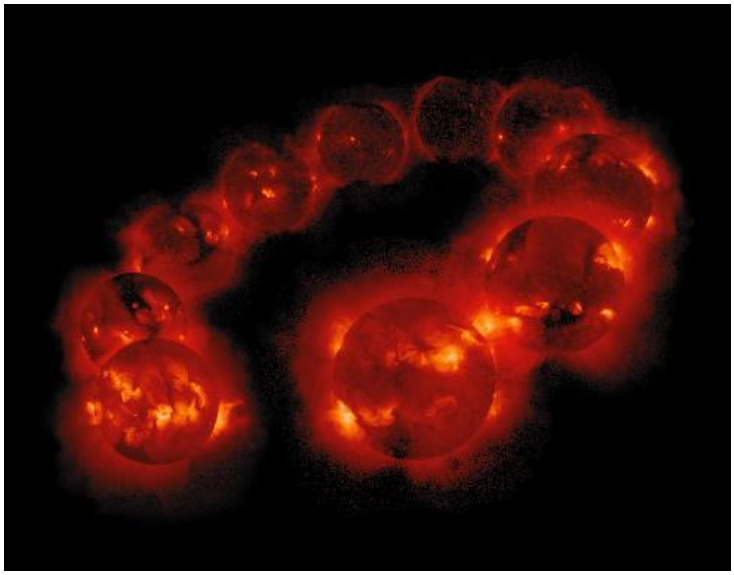

Figure 7. This image features chronological images of the solar corona over the 11-year solar cycle. Starting at the left, in solar maximum, the Sun goes into the declining phase towards solar minimum, at the back of the image, and back into the rising phase towards the next solar maximum, at front right.[9]

2.4. CORONAL FEATURES

Active regions are manifested in a few different ways. Over the solar cycle, sunspots, solar flares and prominences, and coronal holes become visibly more common. Each of these processes is a result of the complex rotation of the Sun as discussed previously.

2.4.1. SUNSPOTS

The first manifestation of activity in the photosphere is the appearance of a magnetic field. If the strength in the magnetic plage surpasses a certain threshold, there occurs a brightening of the photospheric plage. A local magnetic field can

[9] Image credit: Montana State University Solar Physics Group

form within the plage, and this creates a sunspot. A sunspot starts as a "pore", much darker than the surrounding photosphere. Most of these spots fade away after a few hours or days; the localized field sinks below observational photospheric levels. The localized field strength is on the order of 10 gauss. In other cases, the magnetic field increases far past the threshold, and a full sunspot group forms. Most often, one spot at each end of the group is more developed than others, causing the group to become a bipolar sunspot group.

A fully developed sunspot consists of two regions: the umbra and the penumbra. Most of the magnetic flux is channeled through the umbra, and much less passes through the penumbra. Figure 8 shows a fully developed sunspot and its structure.

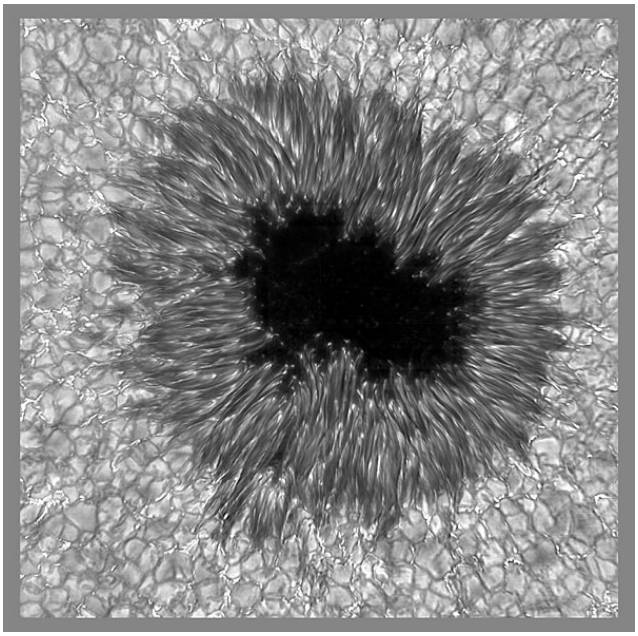

Figure 8. This figure shows an image from the National Solar Observatory (NSO), exhibiting the dark inner umbra of the sunspot, and the penumbra surrounding it radially. Outside of the penumbra is the photosphere.[10]

[10] Image Credit: F. Woeger, KIS. C. Berst & M. Komsa, NSO/AURA/NSF

The magnetic field through the umbra is strongest through the core of the umbra, but is mainly constant throughout the umbra. The field drops through the penumbra and eventually merges with the plage field. The relationship between the magnetic field of the umbra and penumbra and that of the photosphere is not well known. The penumbra is made up of narrow radial bright filaments and a dark background. These filaments are 5000 to 7000 km long and 300 to 400 km wide. Figure 9 shows the relative size of a sunspot compared with the Earth.

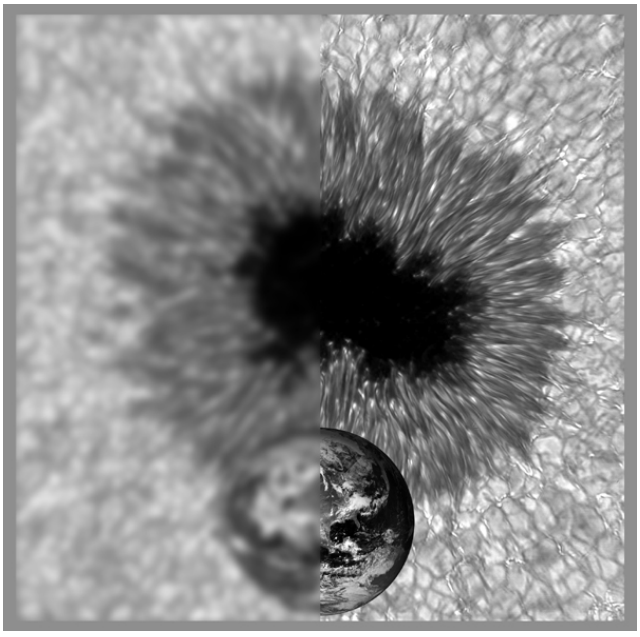

Figure 9. This image from the National Solar Observatory (NSO) shows the relative size of the Earth compared to the size of a normal sunspot. (The blurring of the left side of the image is intentional, to show the improved quality of this NSO telescope.)[11]

At the border of the penumbra and umbra, these filaments end abruptly, and at the end of each filament are bright granules (as noted by Secchi in 1975). Much of the basic structure of sunspots is not understood, but scientists do know that convection is active in the umbra region, and that it is coupled with the

[11] Image Credit: F. Woeger, KIS. C. Berst & M. Komsa, NSO/AURA/NSF

magnetic field there. These full spots last for days, weeks, or months at a time. As discussed above, the field in the sunspot eventually decreases and diffuses. In essence, the three fundamental properties of sunspot activity are: the 11 year cycle, the latitude drift described by Carrington, and the change of polarity of sunspots at solar minimum. Figure 10 shows an excerpt of Maunder's butterfly diagram, which exhibits the migration, or latitude drift, of sunspots toward the equator during the declining phase of the solar cycle.

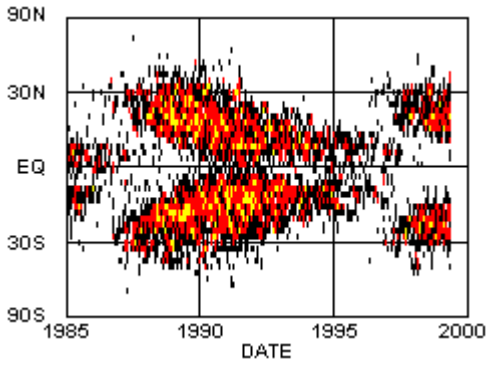

Figure 10. This figure shows a section of the Maunder butterfly diagram, representing the last solar cycle. It is a plot of observed sunspot latitudes as a function of the time (date). As shown, sunspots move toward the equator as the Sun moves into its minimum phase in 1996.[12]

2.4.2. SOLAR FLARES AND PROMINENCES

Solar flares and prominences are also coronal features. Historically, these two aspects of solar activity have been considered separately, but it has become more common to discuss them together, as they are most often connected. A solar flare is a transient, sudden release of energy occurring in and above an active region.[xiii] Flares occur higher in the solar atmosphere than do sunspots. They are

[12] Image credit: NASA, http://science.nasa.gov/newhome/headlines/images/SolarCycle/bfly_recent.gif

a chromospheric phenomenon, as inferred by their name in French, "éruption chromosphérique". They are often seen in either rapidly developing regions, or they appear as the last gasp of a diminishing active region.[xiv] There are only a few phenomena in astronomy that are as fast as solar flares.

Flares generally occur over the umbra and penumbra of the associated sunspot. The flare starts in the active region as a darkening and rising motion along a magnetic field line. The flare proper then begins when two bright areas appear at either side of the line, most often in the form of 'ribbons', which are shown in Figure 11.

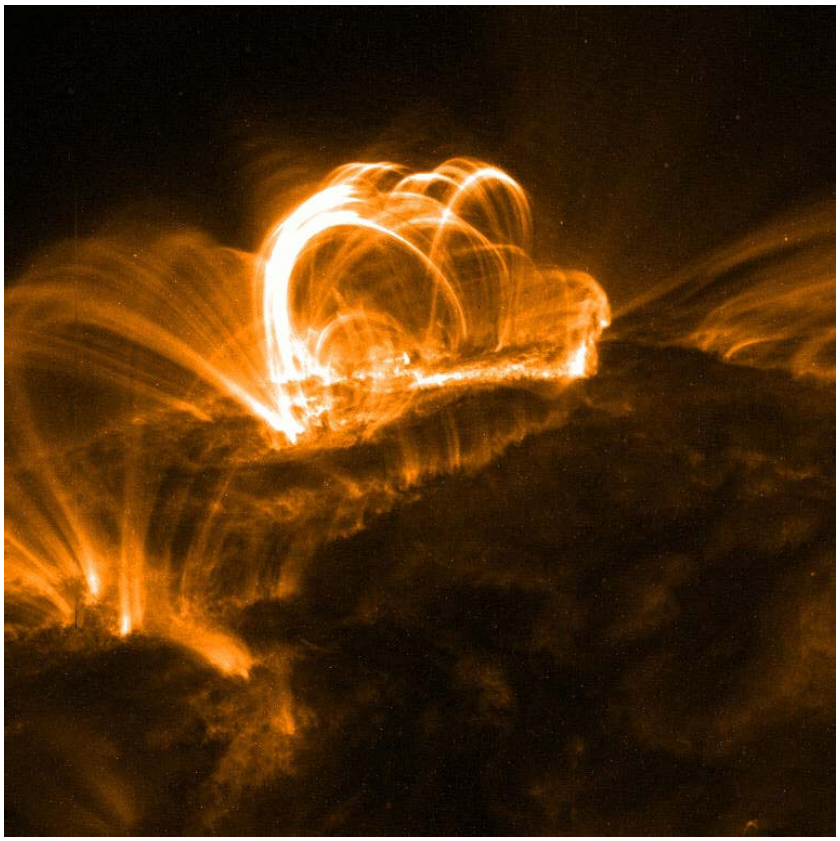

Figure 11. This image from the TRACE spacecraft shows a close-up of a flare observed on September 9, 2005. The "ribbons" of plasma following magnetic field lines can be seen in this close-up view.

Suddenly, these areas experience a rapid expansion, and increase in brightness. This is called the 'explosive' or 'flash' phase. At the explosive phase, shown in a SOHO image in Figure 12, the active region filament is ejected completely from the Sun, upon which time the magnetic energy stored in the twisted structure of the filament is suddenly converted to kinetic and thermal energy. The energy freed during this event can range from 10^{29} to 10^{33} ergs, which is equal to the energy of about 10^{7} to 10^{11} megaton H-bombs.[xv]

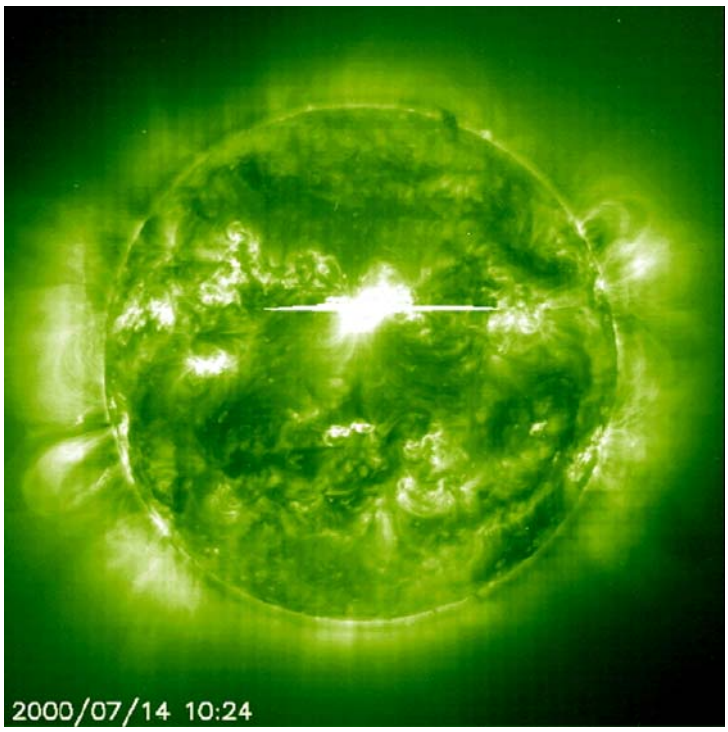

Figure 12. This full-Sun image (UV 195A) from the EIT instrument on the SOHO spacecraft exhibits the massive solar flare observed on July 14, 2000. The image shows the "explosive" phase of the flare in the center of the Sun as it ejects energy and material away from the surface of the Sun.

This energy is transferred to the solar wind and interstellar magnetic field (IMF). The two ribbons separate at high speeds after this event. The presence of

sunspots or high concentrations of magnetic field can hinder the passage of the ribbons, and cause them to die away sooner.

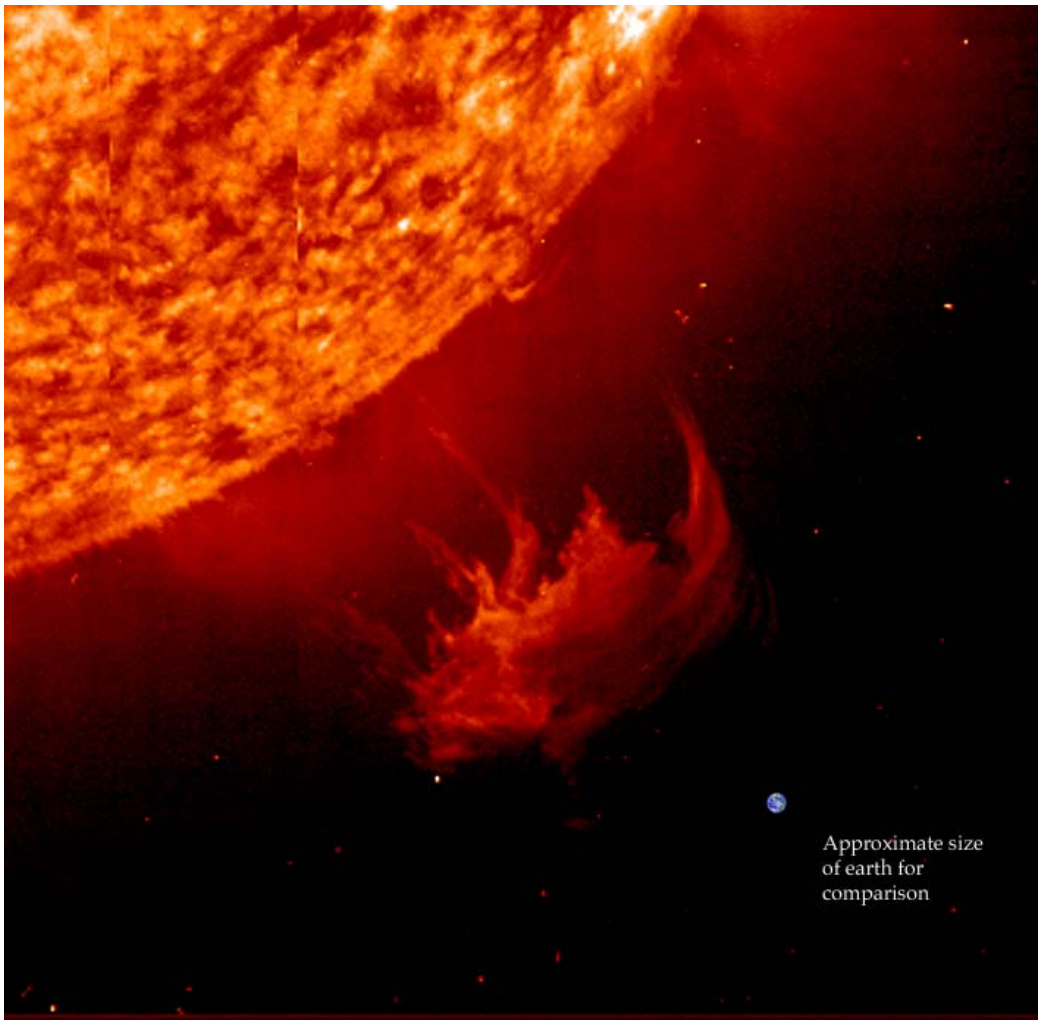

Figure 13. This image from the SOHO spacecraft shows the ejection of material from an explosive solar flare. It also exhibits the massiveness of a single solar flare compared to the size of the Earth.[13]

Under large flares, the size capacity of which is shown in Figure 13, and between the two bright ribbons, dark loops form across the filament. These are called loop prominences[xvi], an example of which is shown in Figure 14. At late stages of a

[13] Image credit: NASA/ESA SOHO EIT, http://umbra.nascom.nasa.gov/eit/images/Sun_and_earth.jpg

flare, the previously invisible loop prominences can occasionally be seen as successive bright loops; other times, they can only be inferred from the path of bright blobs of material that fall back to the solar surface, which is called coronal rain.

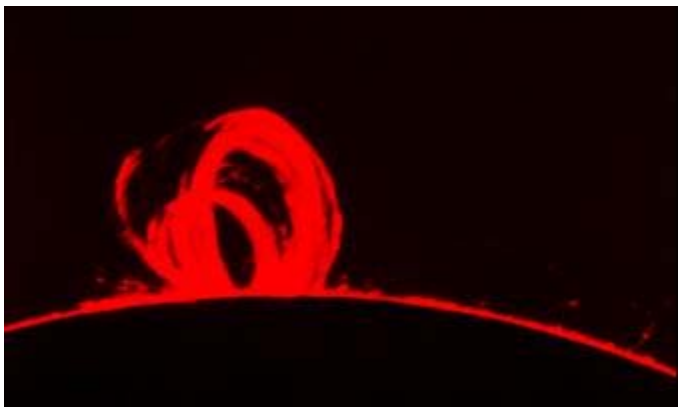

Figure 14. This image exhibits a loop prominence.[14]

The ejection of solar material by these flares adds to the normal solar wind flux from the corona. A new epoch in solar-terrestrial physics began in 1972 when Pioneer 9 and 10 observed four sequential flares on August 2, 4, and 7. The flare especially has been the focus of much research recently, as scientists search for the mechanism by which energy can be so suddenly released. The freed energy from a solar flare creates a shockwave that expands and propagates and is super-imposed on, or "rides over", the previously emitted solar wind. Flares are rarely visible in white light, because most are monochromatic. They can also be observed using ultraviolet, radio, or X-ray radiation.

[14] Image credit: National Optical Astronomy Observatory

2.4.3. CORONAL HOLES

Another coronal feature visible especially by X-ray imagery is the coronal hole. Coronal holes were first discovered using early X-ray images. Scientists observing X-ray images of the corona observed sharply defined areas of little to no X-ray emission on the Sun, and called them coronal holes. A coronal hole is always present at each of the Sun's poles, and they also form at the lower latitudes, most often during the declining phase of the solar cycle, right before solar minimum. An example of a coronal hole image is shown in Figure 15.

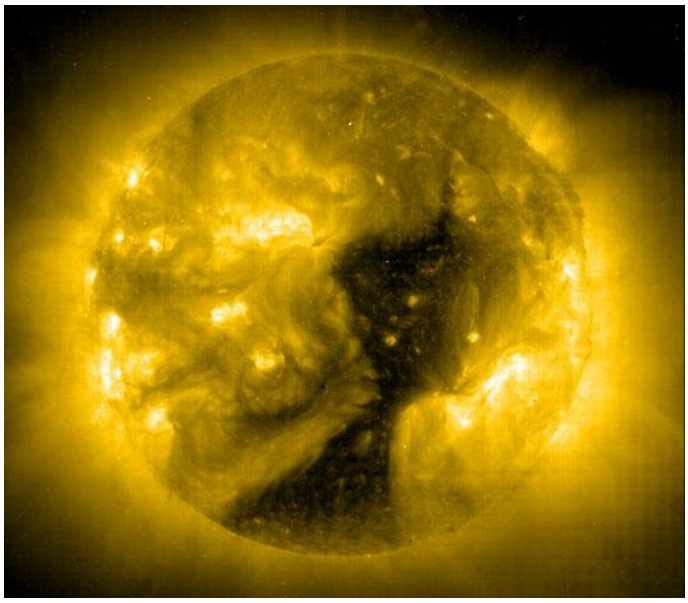

Figure 15. An image showing a polar coronal hole.[15]

Coronal holes start as isolated features, grow larger over the declining phase, and eventually merge with the polar holes. Coronal holes are areas of the corona in which there exist open magnetic field lines. In reality, these magnetic fields are not truly open, but close far enough away from the surface of the Sun

[15] Image credit: SOHO – EIT Consortium, ESA, NASA

that the areas containing coronal holes can be considered as having open magnetic field lines, i.e. there is no end with opposing polarity of a magnetic field line originating from this area. This open magnetic field structure allows a constant stream of high-density plasma to flow out of the coronal holes because there is no magnetic structure to hold it to the solar surface. This causes coronal holes to become less dense and cooler than surrounding regions. At the end of the Skylab mission in 1974, two coronal holes were observed at opposing sides of the Sun. During the following solar eclipse, two streamers connected to the Sun by arch-like structures were observed. These dark structures below are referred to as "Helmet" streamers. Coronal streamers, shown in Figure 16, are the outflow of plasma along the open field lines of the coronal holes.

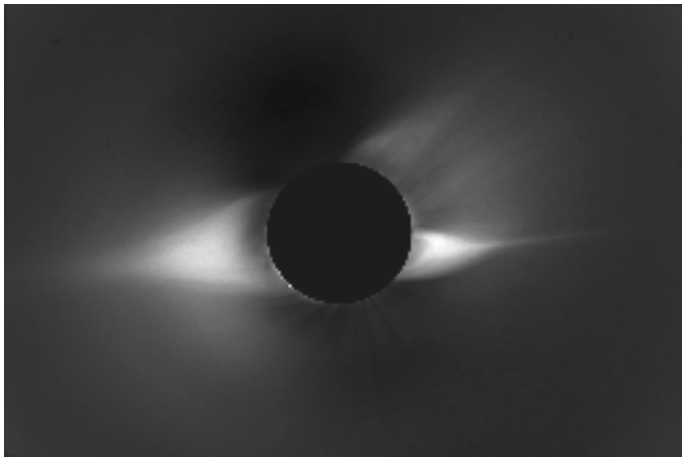

Figure 16. An image from SOHO showing coronal streamers.[16]

Over the portion of the solar cycle observed by the Solar Maximum Mission (SMM), scientists observed a change in positioning of the streamers (and

[16] Image credit: UCAR, University of Michigan, http://www.windows.ucar.edu/spaceweather/aoss335_activesun7.html

therefore coronal holes). During the solar maximum in 1984, the streamers were positioned at angles 30˚ to the solar equator; two years later, in 1986, they were located at angles between 5˚ and 10˚ from the equator[xvii], illustrating the migration, not only of sunspots, but of coronal holes towards the lower latitudes over the solar cycle. Coronal holes are most visible in X-ray imaging, but can also be viewed under ultraviolet light. In the Mg IX line in ultraviolet, occasionally polar plumes are observable; in the He II line, "macrospicules" (large versions of the chromospheric spicules) can be observed. When a coronal hole faces the Earth, there occurs an increase in the intensity of solar wind effects.

2.5. THE TYPES OF SOLAR WIND AND THEIR ORIGINS

There are three different types of solar wind. The *fast solar wind* and the *slow solar wind* are always present in the ambient solar wind, while the *transient solar wind* is usually caused by ejections of material from the Sun by solar flares, solar energetic particle events (SEPs), or coronal mass ejections (CMEs).

The fast solar wind flows away from the Sun at speeds of approximately 700 to 800 km/s. The fast solar wind has long been considered to originate at coronal holes. Beneath the visible coronal hole on the solar surface, there exist "funnels" that originate deeper within the Sun. Convection cells from the convection zone with their associated magnetic fields are brought up by convection to the base of these funnels. Upon reaching the base of the coronal funnel, the convection cell releases its energy upon the funnel, and hence transfers

its energy to flow out of the coronal hole.[xviii] Because of the perturbed magnetic fields of the Sun, coronal holes exist with "open" field lines[17], and therefore, any energy flowing out from these regions is not restricted or contained by a magnetic field. This is what many believe to be the cause of the fast solar wind[xix]. Because of its dependence on the fraction of the solar surface covered by coronal holes, the fast solar wind should be more dominant during the solar maximum and the declining phase of the cycle, when the magnetic fields of the Sun are the most perturbed.

The slow solar wind flows off of the solar corona at lower speeds of approximately 300 to 400 km/s. Unlike the fast solar wind, the origins of the slow solar wind are not very well understood and are still currently an up-and-coming research area in solar physics. Several models for the origins of the slow wind exist, however. One model associates the slow solar wind with the magnetic neutral sheet. It can be mapped back onto loop structures of coronal magnetic fields on the Sun, which are represented by what have been previously referred to as "helmet streamers".[xx] Another model, by Nakagawa and Uchida, maps farther down onto the solar surface, and finds the boundaries of coronal holes to be the source of the slow solar wind.[xxi] Yet another model, called the "blob-loop-reconnection" model by Wang et al. (1998), states that the slow wind is associated with active regions and the magnetic neutral sheet.[xxii] Generally, the slow solar

[17] Magnetic fields over coronal holes are not actually "open"; they close elsewhere in the heliosphere. However, since they reconnect so far away from the Sun, and even from the Earth, they are referred to as being "open" field lines, since the effect of their distant reconnection is minimal.

wind is taken to be a combination of effects from the boundaries of coronal holes and also active regions, due to the strict magnetic fields at these locations. It is postulated that the slow solar wind is slower than the fast solar wind due to its constrained beginnings in the closed field lines of these boundaries and active regions. A recent study of interplanetary scintillation (IPS) measurements suggests that, possibly, the slow solar wind could be caused by compact coronal holes associated with active regions, not large-scale coronal holes.[xxiii] Figure 17 shows a schematic of the sources of the fast and slow solar winds.

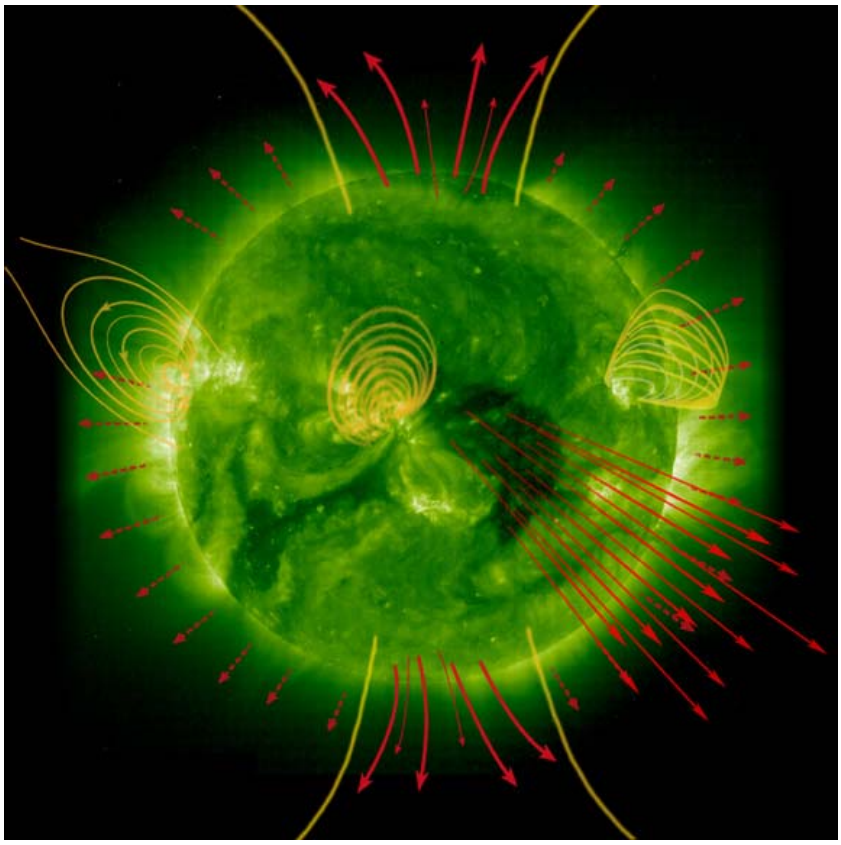

Figure 17. This figure shows the Sun, imaged in ultraviolet light by the SOHO spacecraft. This image shows the origins of the fast and slow solar winds (as they are understood today). The closed field lines over active regions and coronal hole boundaries are the origins of the slow wind; the open field lines coming from the coronal hole regions (especially at the poles) are the causes of the fast solar wind.

The third type of solar wind is the transient solar wind. The transient winds ride over the ambient solar wind, sometimes forming shocks at boundaries between slower-speed streams and the fast stream behind them. The biggest contributor to the transient solar wind (and the main focus of the STEREO mission) is the coronal mass ejections, or CME. Coronal mass ejections are the most powerful explosions in the solar system, yet their origins are not well known. A primary science objective of the STEREO mission is to investigate these elusive origins. Coronal mass ejections consist of about one billion tons of matter traveling at speeds close to one million miles an hour. CMEs are essentially magnetic fields and matter that have been blasted off of the Sun. An image of a CME captured by the LASCO instrument on the SOHO spacecraft is shown in Figure 18, and another by the second LASCO instrument in Figure 19. Figure 20 shows a progression of images so a CME can be observed “in action”.

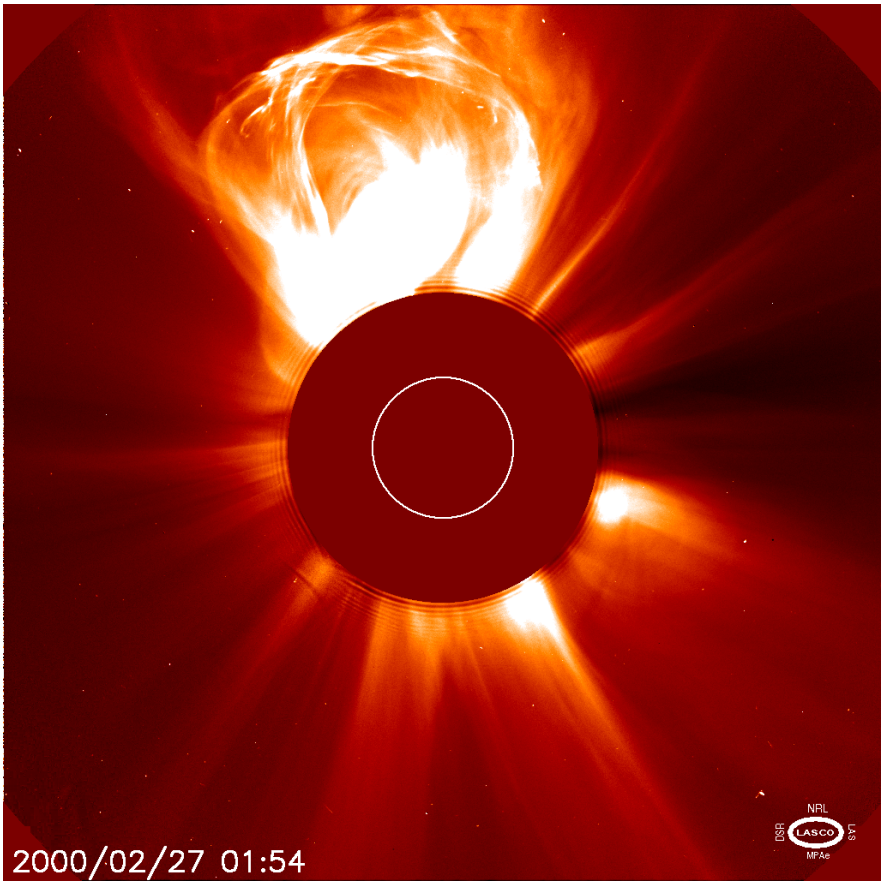

Figure 18. This image, courtesy of the LASCO instrument on the SOHO spacecraft, shows a CME blasting off of the Sun in February of 2000. The CME can be seen at the top of the image, exploding from behind the occulting disc of the instrument.

However, although they are extremely large-scale and strong, they are also thin and spread out, containing only a few particles per cubic centimeter. Most of their power, rather than through shear mass of matter, comes through their strong magnetic fields, which can interact, often extraordinarily, with the Earth's magnetic field.

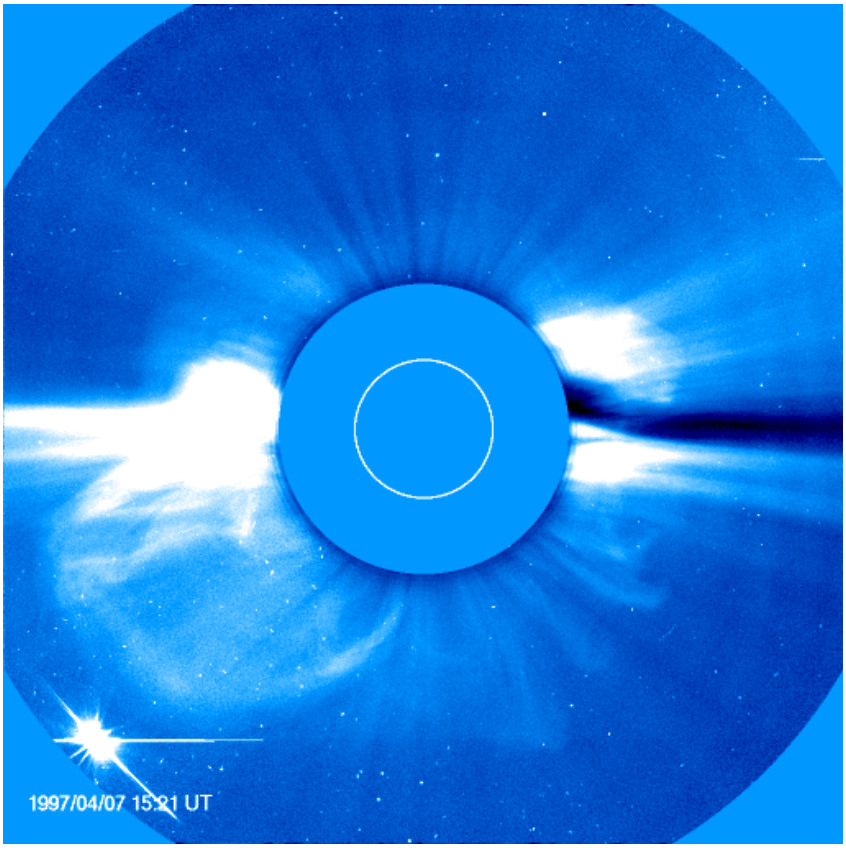

Figure 19. This image shows another view of a coronal mass ejection from April of 1997 by the LASCO2 instrument on board the SOHO spacecraft. The CME can be observed at the mid- to lower-left of the image. Coronal streamers are also observed at the right of the occulting disc.

CMEs are also a source of solar energetic particles, which are a hazard to astronauts. It usually takes CMEs two to four days to reach the Earth, although some extremely high speed ejections have been known to reach the Earth in a little more than one day. CMEs directed straight towards the Earth are observed as halos around the solar disc, and because of this, Earth-directed CMEs are referred to as "halo CMEs" (shown in Figure 20). CMEs are randomly spaced, not following a specific pattern, and are not always present. The numbers of CMEs per day ranges, and on some days, none are observed at all.

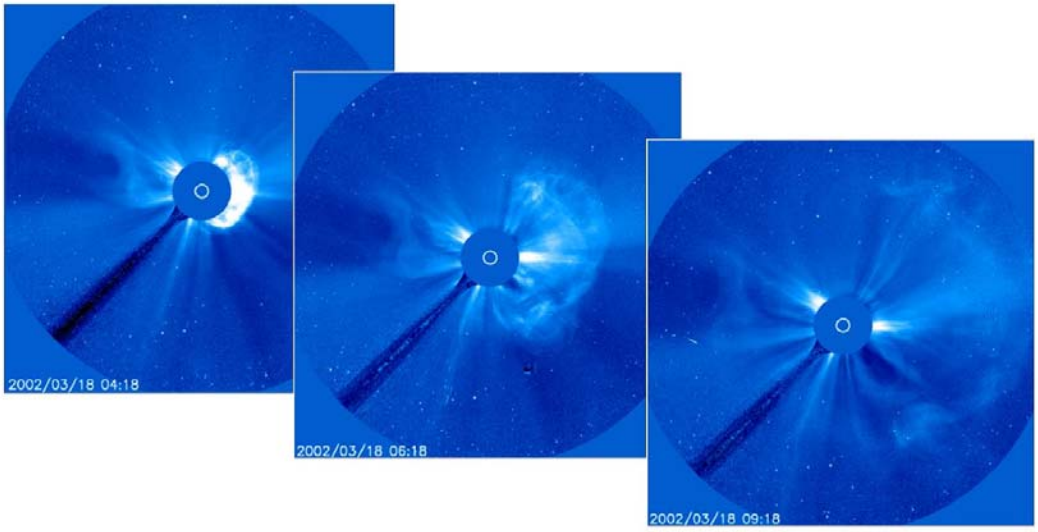

Figure 20. A series of images from the LASCO2 instrument on the SOHO spacecraft serves to exhibit a halo CME in action. Starting at left, an Earth-ward facing CME blasts off of the Sun. Halo CMEs appear this way due to the Earth observer's line of sight. Looking directly at the source region of the CME causes scientists here on Earth to see the CME on all sides of the occulting disc if it is headed towards Earth.

Solar flares can also contribute to the transient solar wind, as discussed above. They can be associated with CMEs, but are not the same thing. Although flares occur lower in the atmosphere than in the corona, they release charged particles that travel along the field lines of the solar wind and can therefore, like CMEs, affect the ambient solar wind state.

The interaction between the fast streams and slow streams of the solar wind exhibits the fluid-like behavior of the overall solar plasma in the heliosphere. To describe the motions of the solar wind, scientists have turned to magnetohydrodynamics, or MHD. The waves caused by the movements of the fast and slow solar winds through the plasma create the "corotating interaction

region". The "ballerina skirt" created by this effect is called the "heliospheric neutral sheet".[xxiv] An image of this phenomenon is shown in Figure 21.

Figure 21. This animation shows the heliospheric neutral sheet, created by the interaction between the fast and slow streams of the solar wind. The waves caused by this interaction are explained by the laws and theories of magnetohydrodynamics (MHD). The Sun is at the center and the planets orbits are shown within the spread of the sheet. This current sheet spreads throughout the heliosphere.[18]

2.6. THE SUN-EARTH CONNECTION

Because the solar wind is magnetically charged, it constantly interacts with the Earth's magnetic field. The "protective magnetic cocoon" in which the Earth sits is called the *magnetosphere*. It is the magnetic environment around the Earth, of terrestrial origin, which protects the Earth from the full brunt of the solar wind. There are five current systems that make up the Earth's magnetosphere.

[18] Image credit: "The Sun", http://www.solarnavigator.net/the_sun.htm

The first is Earth's core, which is the source of the main dipole magnetic field of the Earth, which is shown in Figure 22.

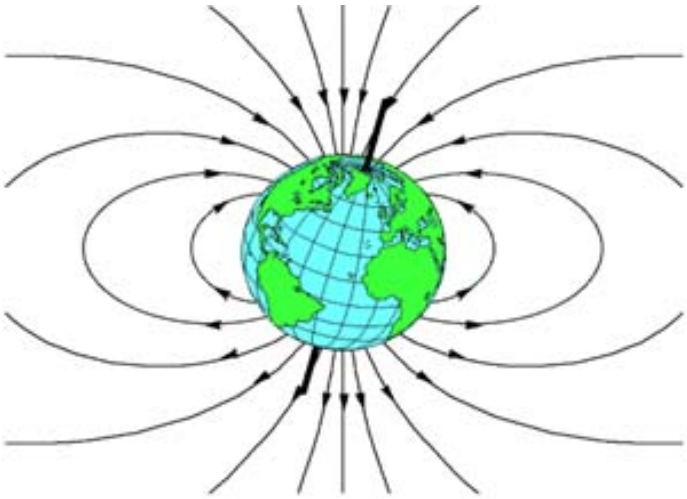

Figure 22. This figure shows a simplified view of the Earth's main dipole field. This magnetic field is due to the liquid core of the Earth.[19]

The other systems that contribute to the magnetosphere are the magnetopause current, the ring current, the cross-tail current, and the field-aligned Birkeland currents. These are shown in Figure 23 in a schematic of the entire magnetospheric structure.

[19] Image credit: Purdue University, Geo-105, "The Planets"

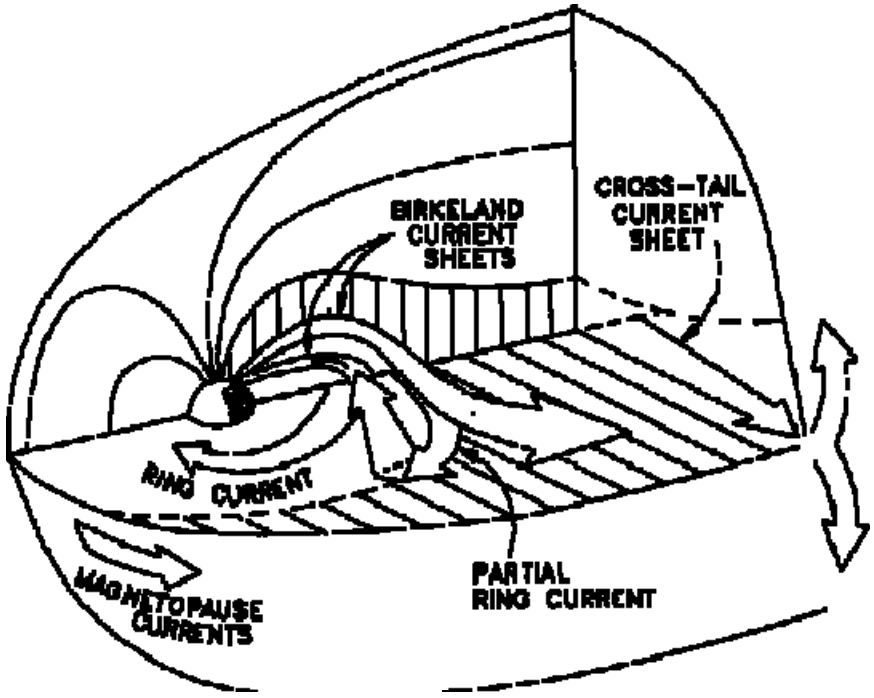

Figure 23. This schematic of the magnetosphere exhibits the five systems that make up the structure of the magnetosphere.[20]

These five systems together make up the Earth's protective magnetosphere, and hence, it is far from static.

The solar wind and Earth's magnetosphere are always tangential to each other, except at one point at which they are normal to each other. This relationship is shown in Figure 24.

[20] Image credit: NASA GSFC, http://www-spof.gsfc.nasa.gov/Education/bh2_3.html

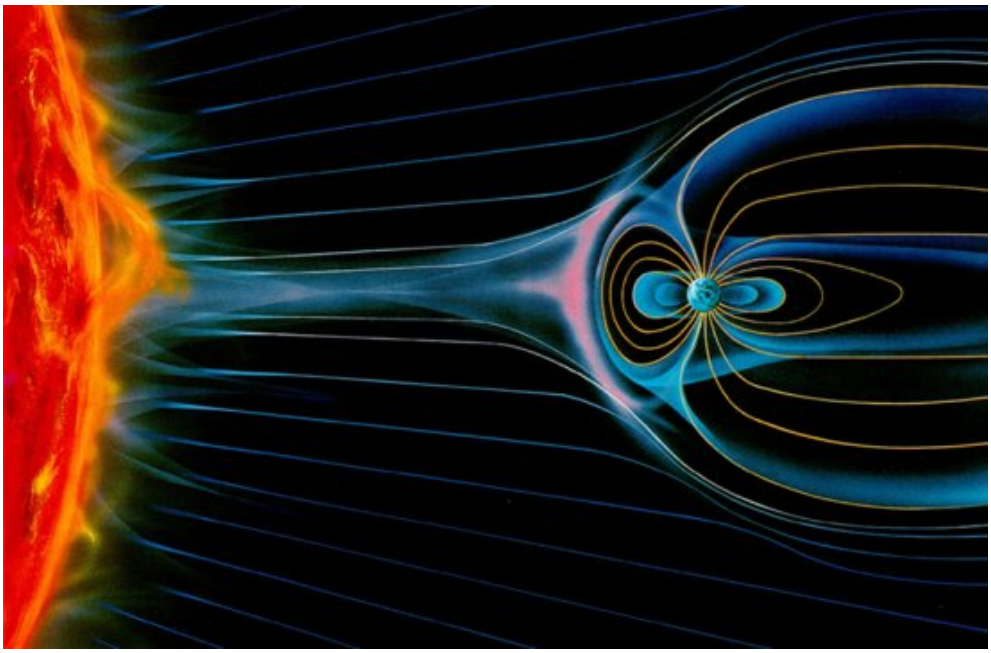

Figure 24. This animation shows the tangential relationship of the solar wind to the magnetic field of the Earth. There is one point at the front of the Earth (at the equator of the dayside) that is normal to the solar wind flow.[21]

The solar wind incident upon the Earth compresses the day side of the Earth's magnetosphere and stretches the night side. This stretched magnetosphere is called the *magnetotail*. It extends up to about 1000 Earth radii from the Earth in the anti-Sunward direction. Occasionally, the magnetotail will be stretched enough by an increased flow of solar wind that a magnetic field line will break. The energy released at the breakage is released into the magnetosphere, and soon the line is reconnected. This is called *magnetic reconnection*. This phenomenon also occurs at other points in the magnetosphere and within the magnetic fields of the Sun. This rapid decrease and recovery of the magnetic field is referred to as a *geomagnetic storm*. Magnetic reconnection is illustrated in Figure 25.

---

[21] Image credit: NASA

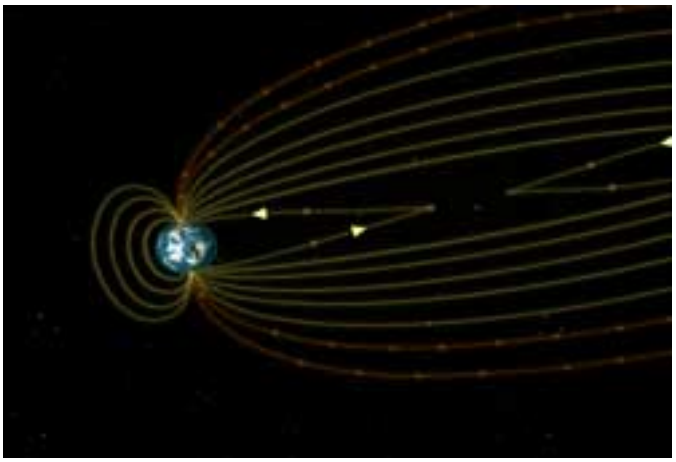

Figure 25. This still-shot of an animation shows the after-effects of a broken field line. The stretched line breaks and is re-connected to its oppositely-charged end after releasing a large amount of energy into the magnetosphere.[22]

The magnetosphere is filled with charged particles. These particles mainly exist in the Van Allen Radiation Belts, which lie in the inner parts of the Earth's magnetic field. They wrap around the Earth and trap solar wind particles in their strong magnetic field. The Van Allen Radiation Belts are shown in Figure 26.

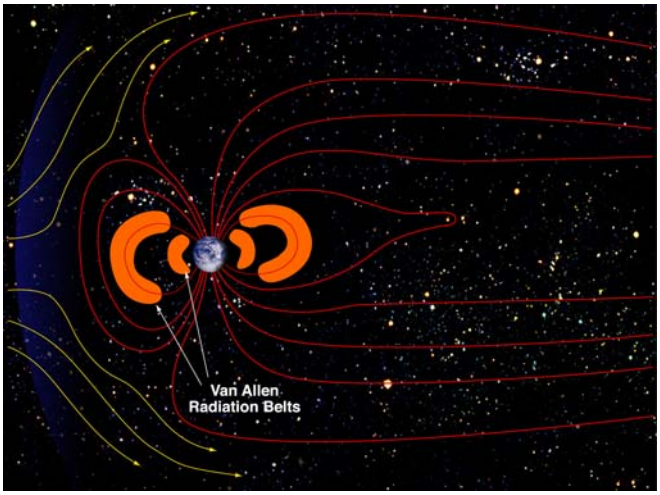

Figure 26. The Van Allen Radiation Belts lie in the inner sections of the magnetic field and trap solar wind particles as they pass the Earth.[23]

[22] Image credit: NASA GSFC

The relationship between the solar wind and the structure of the magnetosphere can be observed in Figure 27.

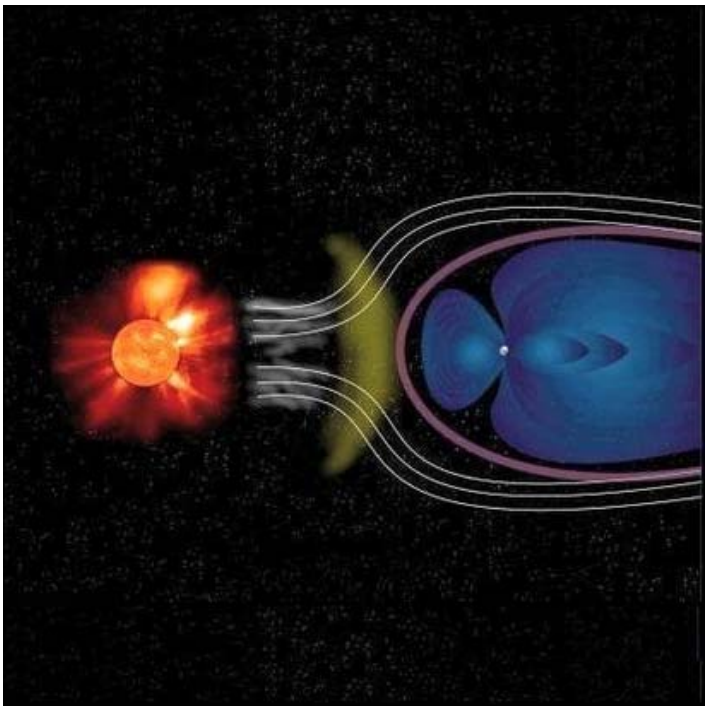

Figure 27. The magnetosphere is warped by the passing solar wind. It is compressed at the day side, and stretched at the night side. The magnetosphere protects the Earth from being bombarded by hazardous solar particles, although some can pass to the Earth through the polar cusp regions.[24]

The Aurora Borealis and Aurora Australis are caused by the energetic particles of the solar wind entering into the Earth's atmosphere.

---

[23] Image credit: ESA Space Weather Web Server, http://esa-spaceweather.net/
[24] Image credit: ESA Science Programme http://sci.esa.int/science-e/

(a)

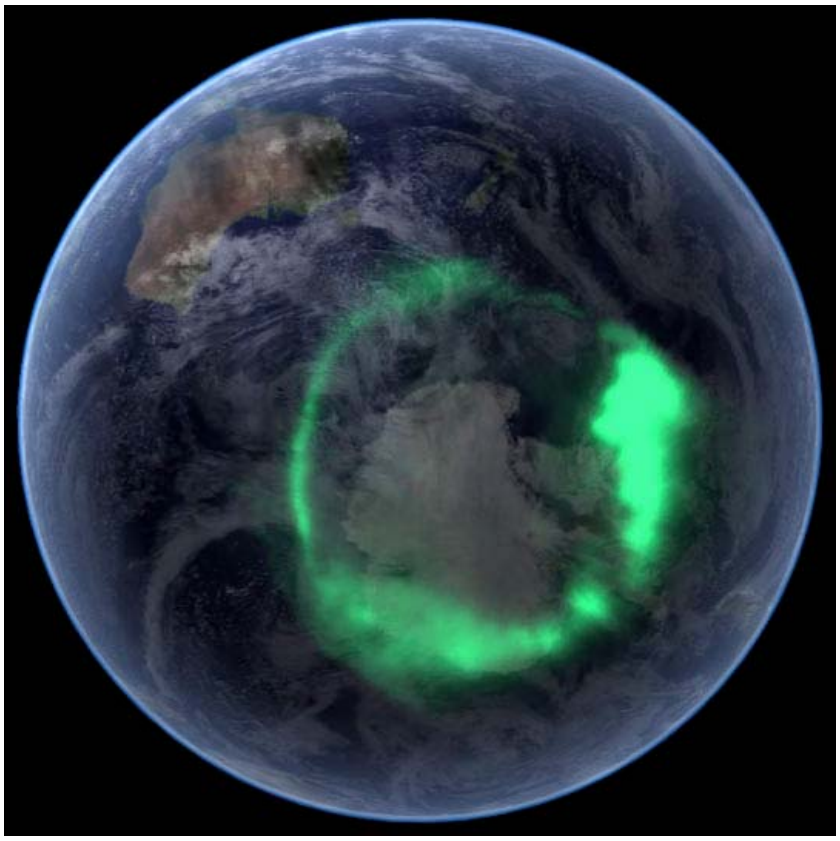

(b)

Figure 28. (a) This image shows a familiar sight of the aurora borealis in the northern hemisphere. (b) This image shows an image captured from space of the aurora australis surrounding the south pole of the Earth. The aurorae are caused by energetic particles, deposited by the solar wind, are transferred onto the field lines of the Earth's magnetic field. These particles spiral up and down the lines and emit radiation as they do so, causing the lights seen on the Earth.[25]

[25] Image credit: a) STEREO Learning Center, NASA GSFC, b) NASA Earth Observatory

The colors seen are due to the spiraling motions of particles around magnetic field lines in the magnetosphere. Although the aurorae are usually present all the time, they are especially noticeable during periods of high solar activity, large CME passages, and after a period of magnetic reconnection in the magnetotail, because these processes send forth an increased number of particles into the Earth's polar regions.

Although the Earth is protected by its magnetosphere, a dilemma quickly presents itself when scientists discuss future space missions. For astronauts traveling outside of the Earth's protective magnet, solar energetic particles carried in the solar wind are extremely hazardous. Astronauts aboard the space station are safe within the magnetosphere; however, any future missions to the Moon are somewhat unsafe until the space weather prediction system is improved. The Moon, due to its distant orbit, only spends about five days of its orbit inside the magnetotail of the Earth. For the rest of its orbit, it takes the full brunt of the solar wind upon its surface, as it has no atmosphere or magnetic field to deflect radiation. Space travelers going past the Moon (to Mars, perhaps?) will be subjected to the assault of cosmic particles as well, although spacecraft can be built to withstand large doses of particles. If an astronaut were on the Moon at the time of a solar flare, proton storm, or CME, he or she would receive approximately 50 rem of radiation, and suffer from radiation sickness. At times of a large solar storm or CME, however astronauts could easily receive 300 rem of radiation, which is fatal.[xxv] Another primary goal of the STEREO mission is to

improve space weather forecasts so that scientists will be able to predict large storms or incoming radiation at dangerous levels.

2.7. THE SOLAR TERRESTRIAL RELATIONS OBSERVATORY (STEREO)

Figure 29. STEREO mission patch.[26]

NASA's Solar Terrestrial Relations Observatory mission, which began in its planning phases in 1996, launched on October 25, 2006 at 8:52pm from Cape Canaveral Air Force Station in Florida on board a Boeing Delta II expendable launch vehicle (Figures 31 and 32). The STEREO mission consists of two nearly identical spacecraft carrying identical scientific payloads. This mission marks the first time two spacecraft were launched on board a single launch vehicle. They are shown stacked for launch in the cleanroom at NASA- Goddard Space Flight Center in October 2006 in Figure 30.

[26] Image credit: STEREO, NASA GSFC

Figure 30. This image (courtesy of NASA-GSFC) shows the two STEREO spacecraft in their final position in the NASA cleanroom before being mounted on the Delta II rocket. STEREO-B is attached to the bottom of STEREO-A in this launch configuration.[27]

[27] Image credit: Courtesy of M. Kaiser, STEREO Chief Scientist

Figure 31. The Boeing Delta II expendable launch vehicle sits atop launch pad 17-B at Cape Canaveral on launch day, October 25, 2006. The white casing at the top of the rocket holds the two STEREO spacecraft.[28]

[28] Image credit: Courtesy of NASA KSC

Figure 32. Following a launch delay at the beginning of the launch window due to temperature issues within the fuel cells, STEREO lifts off at 8:52 pm on October 25, 2006.[29]

The two satellites will orbit the Sun for two years at 1 AU, or at Earth orbit. One spacecraft will lead the Earth, the other will trail behind it. Respectively, these orbiters are called STEREO-A (for Ahead) and STEREO-B (for Behind). The orbit configuration and planned mission is shown in an artist's conception in Figure 33.

[29] Image credit: Courtesy of NASA KSC

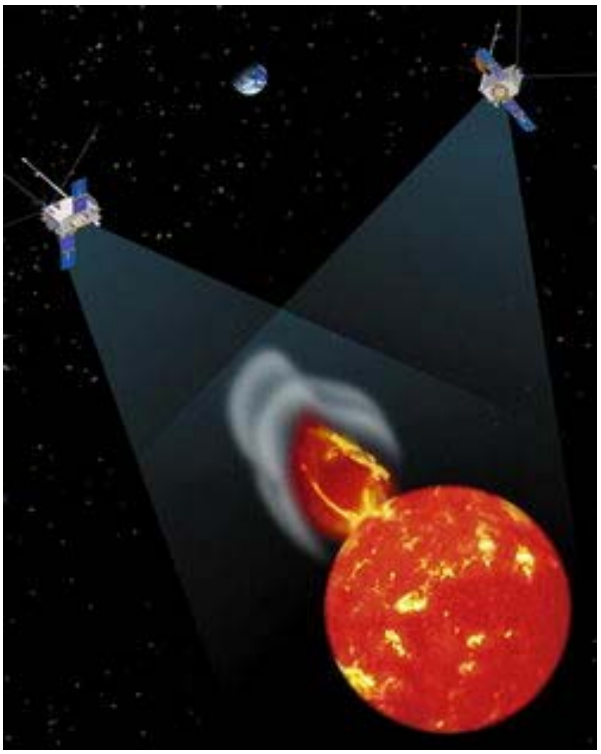

Figure 33. This artist's interpretation of the STEREO mission shows the two satellites pointed toward the Sun. STEREO-A, at left, leads the Earth, and STEREO-B, at right, trails Earth. Earth can be seen at the center of the two spacecraft. The three form a "string of pearls" on the Earth-orbit ellipse.[30]

The four instrument packages on the STEREO spacecraft will take both remote sensing and *in-situ* measurements, and are shown with their locations on the spacecraft in Figure 34. The two remote sensing packages onboard are the Sun-Earth Connection Coronal and Heliospheric Investigation (SECCHI) instruments and the STEREO/WAVES (SWAVES) instruments. The SECCHI instrument package contains all of the imaging telescopes, whereas SWAVES is responsible for radio triangulation of interplanetary radio bursts and disturbances. The Plasma and Suprathermal Ion Composition (PLASTIC) Investigation and the *In-situ* Measurements of Particles and CME Transients (IMPACT) instrument

[30] Image credit: STEREO, NASA Science Mission Directorate

will be taking *in-situ* measurements. IMPACT will provide plasma characteristics of solar energetic particles and the local magnetic field. PLASTIC will provide plasma characteristics of protons, alpha particles, and heavy ions in the solar wind.[xxvi]

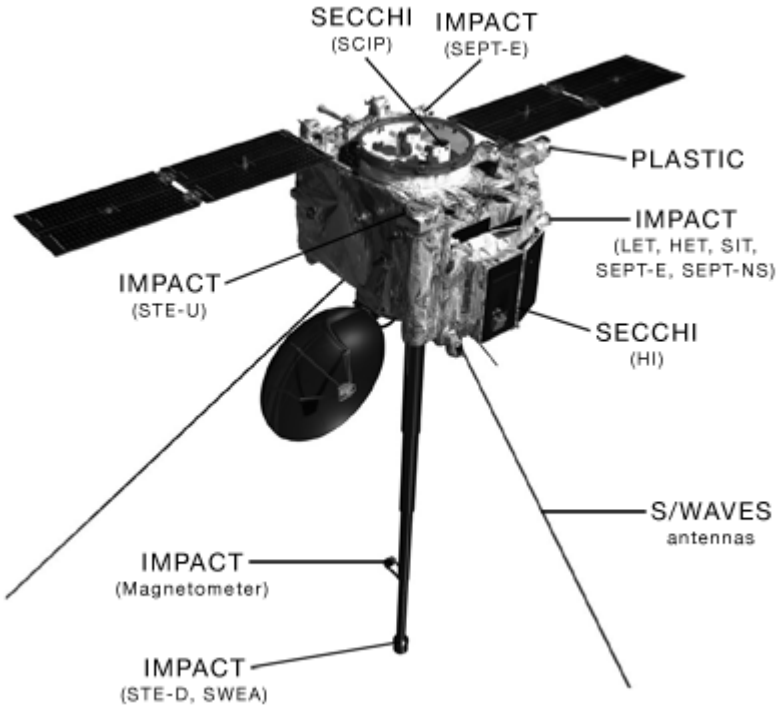

Figure 34. This schematic of the STEREO-A spacecraft (which is identical to STEREO-B) shows all of the instrument packages and their locations on board the spacecraft. [31]

The primary science goals of the STEREO mission are to:

- Understand the causes and mechanisms of CME initiation
- Characterize the propagation of CMEs through the heliosphere
- Discover the mechanisms and sites of energetic particle acceleration in the low corona and the interplanetary medium

[31] Image credit: STEREO, NASA GSFC

- Develop a 3D time-dependent model of the magnetic topology, temperature, density, and velocity structure of the ambient solar wind
- Provide a continuous low-rate data stream for the purposes of space weather specification[xxvii]

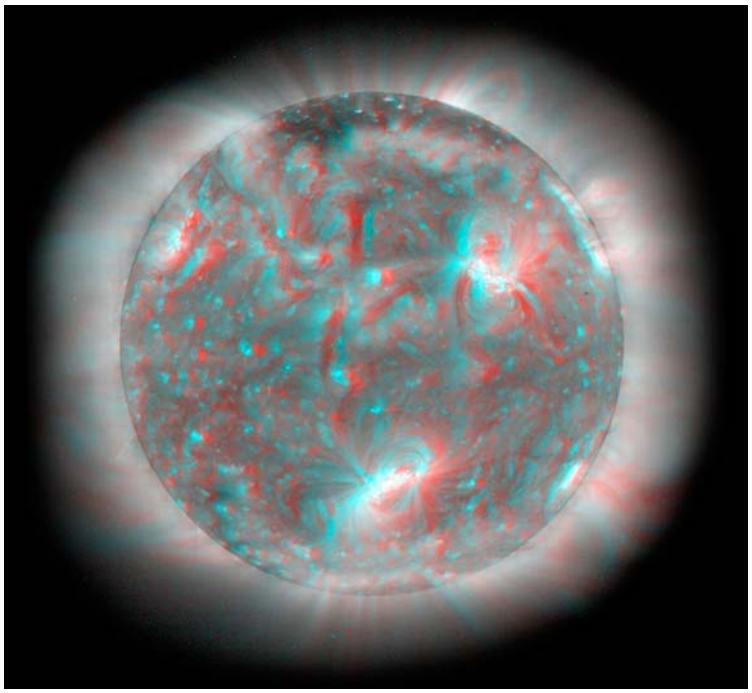

Figure 35. The SECCHI team postulates the expected outcomes of the first-ever 3D images of the Sun here. The first 3D images will be released by NASA around January, 2007.

Through these goals, STEREO will deliver the first-ever three-dimensional images of the Sun. It will also provide the first stereo imaging and tracking of transients from the Sun to Earth, simultaneous imaging of solar phenomena with *in-situ* measurements (by PLASTIC and IMPACT), the first continuous determination of interplanetary shock positions by radio triangulation (by SWAVES), and the first imaging of greater than 180 degrees of the solar surface (by SECCHI). The ultimate goals of the STEREO mission is to

characterize and understand the mechanisms that cause CMEs, and to use that information to predict space weather conditions and improve alert systems in the future.

During the first three months after launch, the spacecraft are placed in "phasing" orbits around the Earth-Moon System, which are shown in the orbit plan in Figure 36.. Three lunar swingbys are used (one for STEREO-A (S1), two for STEREO-B (S1, S2)) as gravity assists to provide the spacecraft with the necessary energy to attain their final heliocentric orbits.

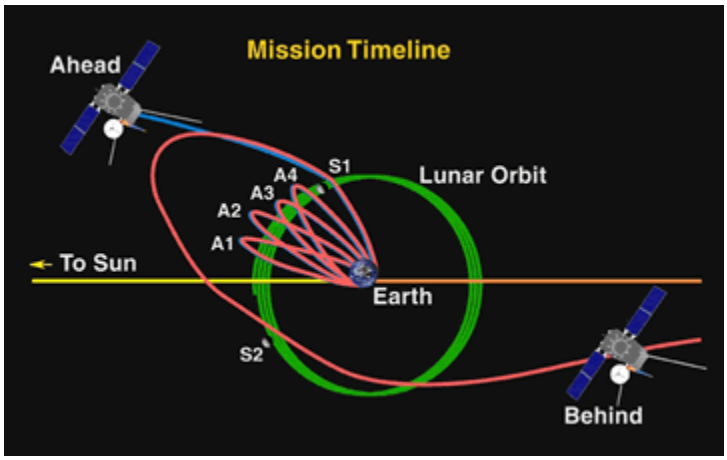

Figure 36. This animation is a representation of the phasing orbits that the STEREO spacecraft will undergo. The Ahead spacecraft will undergo one lunar swingby, and the Behind spacecraft will undergo two lunar gravity assists.

During these three months, as the spacecraft are positioned, they and their instruments are calibrated and commissioned. After reaching their respective heliocentric orbits, STEREO-A and STEREO-B will gradually drift away from each other at a rate of 45˚ per year. STEREO-A will orbit the Sun at a slightly smaller distance than STEREO-B, giving it a spacecraft "year" of 346 Earth days, and STEREO-B, slightly farther out from the Sun, has a spacecraft "year" of 388

Earth days. This orbital separation of the spacecraft allows the remote imager (SECCHI) to obtain three-dimensional images of the Sun, while the *in-situ* instruments sample the solar wind as it flows past the spacecraft at two different locations.

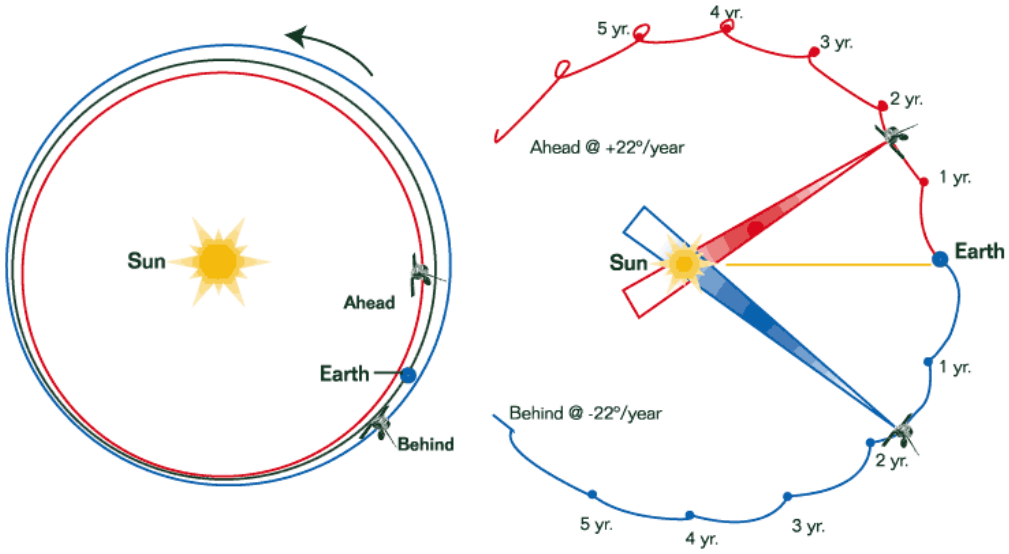

Figure 37. On the left, the Ahead and Behind observatories are shown in their respective positions ahead of and behind the Earth in its orbit. Also shown is the slightly shorter path taken by the Ahead observatory, and the slightly longer one taken by the Behind observatory. At right, the separation of the spacecraft is projected for up to 5 years. The spacecraft each move away from Earth at approximately 22 degrees per year. (STEREO-A is above the Earth in this schematic, STEREO-B is below.)[32]

2.7.1 THE PLASMA AND SUPRATHERMAL ION COMPOSITION (PLASTIC) INVESTIGATION

The Plasma and Suprathermal Ion Composition (PLASTIC) Investigation is based at the University of New Hampshire in Durham, New Hampshire, and was built by UNH, the University of Bern, the Max Planck Institute for

[32] Image credit: STEREO, NASA GSFC

Extraterrestrial Physics, the University of Kiel, and NASA Goddard Spaceflight Center. PLASTIC provides solar wind ion and suprathermal (0.25-100 keV/e) positive ion measurements for STEREO. PLASTIC is the primary sensor on STEREO for studying the relationships between coronal and solar wind ions and solar wind ions and heliospheric processes.

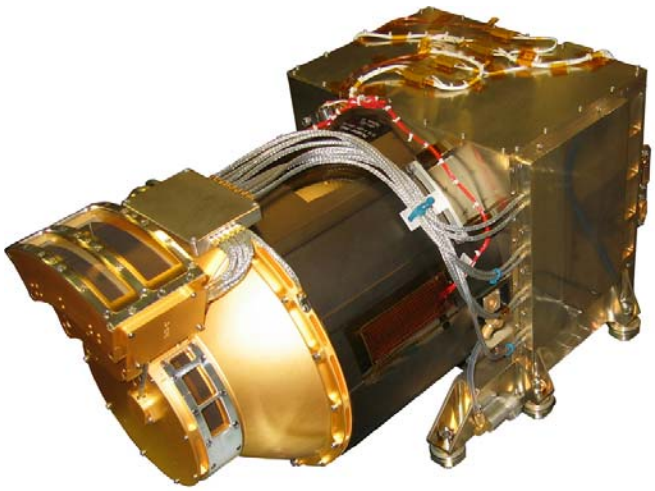

Figure 38. Flight Model 1 (FM1) of PLASTIC is shown in this image, courtesy of UNH Space Science Center.

The main science goals of PLASTIC are as follows:[xxviii]

- ***CMEs: Solar Origins, Interplanetary Manifestation and Topology***
    - ⊙ In-situ signatures of corresponding CME structures on the Sun, including...
        - ICME identification and boundary determinations
        - Global (3D) structure of CMEs at 1 AU, including ...
        - Multipoint measurements of magnetic clouds and multiple ejecta

- ***Gradual Solar Energetic Particles (SEP) and Heliospheric Studies***
  - ⊙ Acceleration of ions at CME-driven shocks
  - ⊙ Global structure of stream interfaces and heliospheric current sheet dynamics
  - ⊙ Global structure of co-rotating interaction regions
  - ⊙ Pickup ions (longitudinal and solar wind parameter dependence)
- ***Solar Processes and Solar Wind Studies***
  - ⊙ Elemental composition: fractionation effects, including in ICMEs
  - ⊙ Charge states: coronal processes and solar wind (including ICME) formation
  - ⊙ Origins (slow solar wind, transition with fast solar wind)

The PLASTIC investigation incorporates three sensor operations. The first is the Solar Wind Sector (SWS) Proton Channel. This measures the distribution functions of solar wind protons (H^{+}) and alphas (He^{+2}), which provides proton density, velocity, kinetic temperature (or thermal speed) and its anisotropy, and alpha to proton (He^{+2} / H^{+}) ratios with a time resolution up to about 60 seconds. The second sensor within PLASTIC is the Solar Wind Sector (SWS) Main Composition Channel. This measures elemental composition, charge state distribution, kinetic temperature (thermal speed), and speed of the more abundant solar wind heavy ions (e.g., C, O, Mg, Si, and Fe) using Electrostatic Analyzer (E/Q), Time-of-Flight (TOF), and Energy (E) measurement

to determine mass and mass per charge (M/Q). Typical time resolution for selected ions will be approximately 300 seconds. The third sensor operation within PLASTIC is the Wide Angle Partition (WAP), which measures the distribution functions of suprathermal ions, including interplanetary shock-accelerated (IPS) particles associated with CME-related SEP events, recurrent particle events associated with Co-rotating Interaction Regions (CIRs), and heliospheric pickup ions. Typical time resolution for selected ions will be about 300 seconds. (Time resolution actually depends on event statistics).[xxix]

The subsystems on PLASTIC are the Entrance System, the Time-of-Flight Chamber, and the Electronics Box.

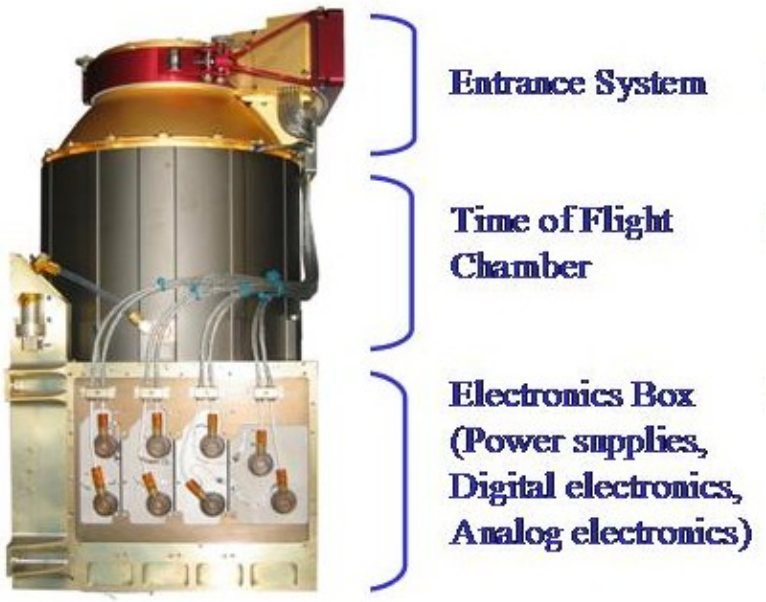

Figure 39. The PLASTIC instrument, denoted with all of its subsystems.[xxx]

The Entrance System selects a polar angle at which to receive solar wind particles, selects the energy per charge ratio (E/Q), and then suppresses ultraviolet radiation and scattered ions and eliminates solar wind electrons, such that only solar wind protons, alphas, and heavy ions pass through the entrance system to the Time-of-Flight (TOF) chamber.

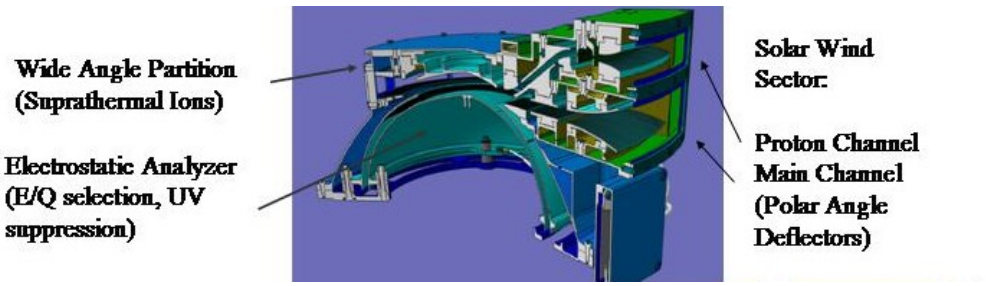

Figure 40. The entrance system of PLASTIC, labeled with its three separate sensor systems.[xxxi]

Upon passing into the TOF chamber, the solar wind particles go through a complex system of detectors (microchannel plate (MCP) detectors, solid state detectors (SSD)), hit the signal board, or anode detectors. The TOF chamber identifies the species, measures the intensity of the beam of particles, and measures the azimuthal angle at which the particles enter the instrument.

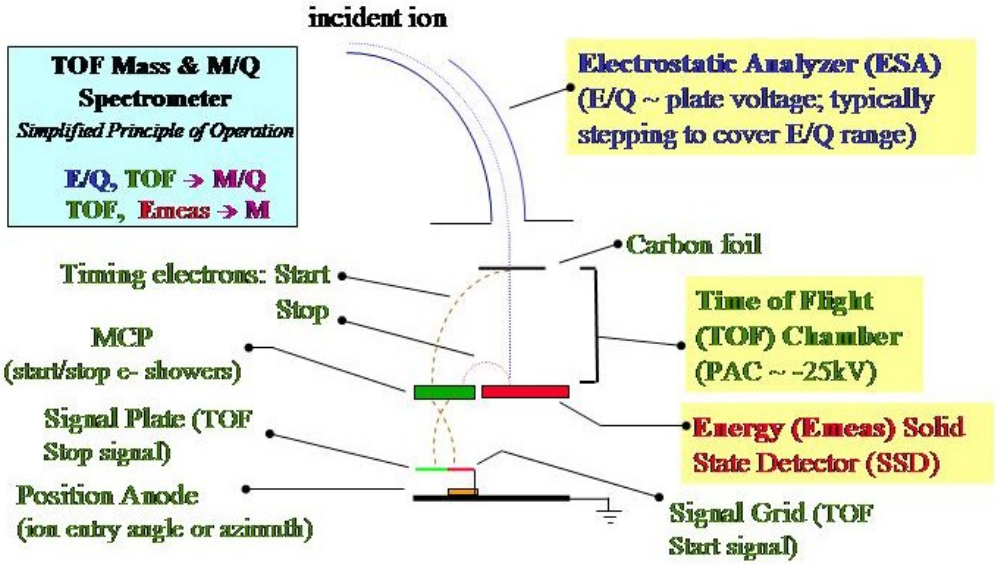

Figure 41. This schematic is a simplified view of the path of an incident solar wind ion once it passes into the entrance system and TOF chamber.[xxxii]

Upon data return, this information can be used to find mass and mass per charge, elemental composition, speed, density, temperature, and direction of the solar wind ions.

2.8. PAST SOLAR-TERRESTRIAL MISSIONS

STEREO is not the first mission sent to study the solar wind – in fact, it is the third of NASA's Solar Terrestrial Probes missions. Data from several past missions are considered in this thesis, and therefore it is appropriate to describe them.

The Advanced Composition Explorer (ACE) was launched in August 1997 with a primary research focus of determining and comparing the isotopic and elemental composition of several distinct samples of matter, including the

solar corona (solar wind), the interplanetary medium, the local interstellar medium, and Galactic matter. It orbits at the L1 Langrangian point, which is close to 1 AU, and is therefore appropriate to analyze ACE data in terms of predictions for STEREO observations.

Another mission that is related to STEREO predictions is the WIND satellite, launched in November of 1994. Specifically, the Solar Wind Experiment (SWE) instrument on the spacecraft measured ions and electrons in the solar wind and the foreshock regions (particles whose energies are in the keV range). From these measurements, the solar wind velocity, density, temperature and heat flux could be deduced. The WIND spacecraft also orbited at the L1 Lagrangian point from 1994 until 1998, when its mission was changed. However, SWE data from these years is valuable to space weather predictions for STEREO, as this period was during the previous solar minimum.

The third spacecraft used to predict STEREO observations is the Solar and Heliospheric Observatory (SOHO). SOHO was launched in 1995 as a joint effort between NASA and the European Space Agency (ESA). Several instruments on SOHO are important for comparison to STEREO observations, for instance the Extreme Ultraviolet Telescope (EIT), the Large Angle and Spectrometric Coronagraph (LASCO), and the Ultraviolet Coronagraph Spectrometer (UVCS) provided ultraviolet images of the surface of the Sun and coronagraphs, whereas the Charge, Element, and Isotope Analysis System/Proton Monitor (CELIAS/PM) provided in-situ measurements of the solar wind at the L1 Lagrangian point.

Using data from WIND, ACE, and SOHO provided data spanning from 1995 to the present, therefore providing solar wind data for various parameters over the entire previous solar cycle, which began in 1996 and lasts until early 2007.

CHAPTER 3

METHODS

Solar cycle 23 began in 1996 (with the solar minimum in that year) and will end in 2007 with the upcoming solar minimum. To study the complete solar cycle, data from each year had to be combined to cover each of the eleven years. For the years 1998 through the present, we were able to use Level 2 proton data from the Advanced Composition Explorer (ACE) spacecraft, specifically the Solar Wind Electron, Proton & Alpha Monitor (SWEPAM) instrument[xxxiii]. Level 2 data have been verified and corrected, whereas Level 1 data are raw data (i.e. not averaged). We used data from the whole data range of the SWEPAM instrument, which started 23/1998, where 23 refers to the day-of-year, or DOY, a common way of demarking days in data sets, as one does not have to specify the month and day. For example, 23/1998 corresponds to January 23, 1998. The data from the SWEPAM instrument were hourly averages of proton velocities, densities, and temperatures, and also the Geocentric Solar Magnetospheric (GSM) coordinates of the solar wind velocity (v_x, v_y, v_z) per hour. These coordinates can be used to calculate the direction of the solar wind at hourly checkpoints. The data received from the SWEPAM instrument team, based at the Los Alamos

National Laboratory in New Mexico, amounted to approximately 75,000 data sets over the years since 1998.

To both expand the amount of data and the amount of time for which we had data, we also acquired data from the Solar and Heliospheric Observatory (SOHO) spacecraft, specifically from the Charge, Element, Isotope Analysis System Experiment (CELIAS) onboard SOHO[xxxiv]. Data were received from two of the five sensors that make up the CELIAS instrument: the Mass Time-of-Flight (MTOF) spectrometer and the Proton Monitor (PM) experiment. This data began on 17/1996, or January 17, 1996. The data sets from SOHO/PM were also hourly averaged data, and amounted to almost 88,000 sets of data. Each data set received from the SOHO/PM instrument team consisted of the hourly-averaged proton velocity, density, thermal speed, and the North-South angle at which the solar wind was flowing. Because we had started with temperature from the ACE spacecraft, we converted the thermal speed measured by the SOHO/PM instrument into temperature using the equation

$$T_K = v_{th} * 60.3434 \qquad (1)$$

where T_K is the temperature in degrees Kelvin and v_{th} is the thermal speed of the particles. Another difference between the ACE/SWEPAM data set and the SOHO/PM data set was that the SOHO/PM instrument measured the North-South angle from which the solar wind was flowing outright, whereas the SWEPAM instrument measured the velocity coordinates in the GSM plane, which allowed us

to calculate the North-South *and* East-West flow angles after receiving the data. Hence, we only have North-South flow angle data from the SOHO spacecraft.

The third set of data collected was by the WIND spacecraft, specifically the Solar Wind Experiment (SWE) instrument[xxxv]. These data began on 319/1994, or November 15, 1994, although we mainly analyzed data after 1995. The data received from the WIND-SWE instrument, based at the Massachusetts Institute of Technology, include proton velocities, East-West flow angles, North-South flow angles, densities, and thermal speeds. These data are also hourly averaged values, and amount to approximately 96,000 data sets. Like the data from the SOHO/CELIAS instrument, we used Equation 1 to convert thermal speeds into temperature values such that they could be compared to data from the ACE/SWEPAM instrument.

These three spacecraft are not the only probes to analyze the solar wind environment, but they are the most relevant to the STEREO mission due to their orbits. Each of these spacecraft orbits at the L1 Lagrangian Point. Lagrangian points are the five points in interplanetary space where a small object affected only by gravity can theoretically be stationary relative to two larger bodies. The Lagrangian Points are locations where the combined gravitational pull of the two larger bodies provides precisely the centripetal force required to rotate with them. They allow an object to orbit in a fixed position in space rather than in an orbit in which its relative position changes continuously.[xxxvi] This is analogous to geosynchronous orbits. These points are shown in Figure 42.

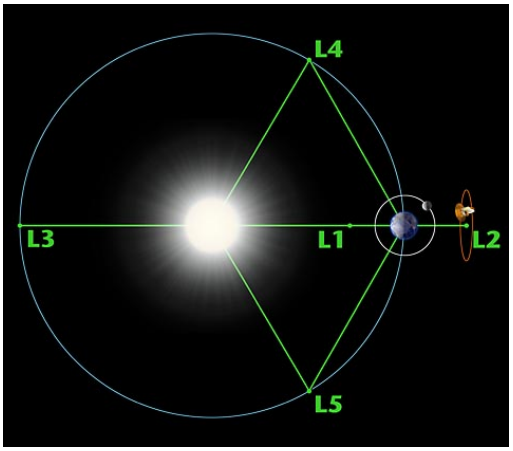

Figure 42. This figure, for NASA's WMAP mission, (located at L2) shows the relative locations of the five Lagrangian Points in the Earth-Sun system. L1 is the stable orbit point between the Sun and the Earth. [33]

L1 represents the stable location for satellite orbits between the Sun and the Earth. Due to the massive size of the Sun compared to the Earth, the equilibrium point of gravity between these bodies is close to the Earth. Hence, these satellites orbiting at this distance from the Sun experience similar conditions to those that STEREO will experience during its orbit at 1 AU, or Earth-orbit distance. In actuality, the WIND spacecraft was originally orbiting at the L1 point, but its mission was changed in 1998 when SOHO was launched to the same orbit. Hence, we only used WIND data through November 1998, when its orbit was changed and it no longer orbited at a comparable distance to that of STEREO.

To classify the data and to find initial averages and extreme cases, we created histograms of solar wind speed, density, and temperature from each data set for each Carrington Rotation period since January 1996. This corresponds to approximately 13 to 14 histograms per year for each parameter. To analyze solar

[33] Image credit: Cornish, N.J., "The Lagrangian Points", Wilkinson Microwave Anisotropy Probe (WMAP) Homepage, February 2006, http://map.gsfc.nasa.gov/m_mm/ob_techorbit1.html

wind direction, or flow angle, we plotted the value of the angle versus time on x-y scatter plots for each Carrington Rotation period. Using these histograms, we were able to calculate rotational averages (i.e. approximate monthly averages). Also, we found 10% and 90% values per Carrington Rotation for each of the solar wind parameters. That is, we found the range of values for each rotation, and then analyzed the whole data set to find how many hours the solar wind was within 10% of the normal, and how many hours per rotation the solar wind was within 90% of the normal. Using this method, we could pick out extreme cases in which the solar wind parameter (being speed, temperature, or density) was far above normal for that particular rotation period. To study these cases more in-depth, we often created plots of individual days. Many of the instances could be correlated with a known CME event or shock event, according to the SOHO/LASCO CME catalogue.

Of specific interest were the periods of solar minimum and solar maximum. For in-depth study of these periods, we chose to examine the months of June and July 1996 during the previous solar minimum and the months of June and July 2001 during the previous solar maximum. To find the relationships between the parameters at these times, we employed a technique of plotting the parameters against one another, rather than plotting the parameters singularly over time. We created plots of temperature vs. speed, temperature vs. density, and speed vs. density for both solar maximum and solar minimum. From these plots,

we were able to deduce the relationships between the parameters themselves, and also the relationships between the parameters and the phases of the solar cycle.

In order to visualize the solar cycle and to correlate solar activity with solar wind conditions, we used data from the National Oceanic and Atmosphere Association (NOAA). The National Geophysical Data Center (NGDC) within NOAA offers sunspot number counts dating back to 1750. Using sunspot number data for solar cycle 23, we were able to plot solar wind parameters against the sun spot number for a particular Carrington Rotation and find the relationship between the active region count and the space weather conditions measured by the solar probes.

Another data source is the SOHO/LASCO CME Catalog.[xxxvii] The catalog contains all CMEs manually identified since 1996 from the Large Angle and Spectrometric Coronagraph (LASCO) on board the SOHO mission. LASCO has three telescopes C1, C2, and C3. However, only C2 and C3 data are used for uniformity because C1 was disabled in June 1998. In the absence of a perfect automatic CME detector program, manual identification is still the best way to identify CMEs. We used the catalog to find the average number of CME events per day for each month of the solar cycle. We used these averages to plot the occurrences of CMEs over a solar cycle to attempt to find a correlation between the solar cycle and the number of CME events. We attempted to find the correlation by plotting the averages over time, and also by plotting the CME numbers against the active region count by NOAA.

To find the effects of CMEs on the ambient solar wind conditions, we looked specifically at several important and well-known CMEs during the past solar cycle. For each event, we plotted our solar wind parameters over time to find the changes in the nature of the wind as the CME passed by the spacecraft. In addition to other, smaller events, we looked specifically at the first strong geo-effective period of solar cycle 23, which occurred May 1-4, 1998; the Bastille Day storm on July 14, 2000, which caused intense geomagnetic storms and affected power grids; and the Halloween storm on October 28, 2003, during which the Aurora Borealis could be seen as far south as Washington, D.C.

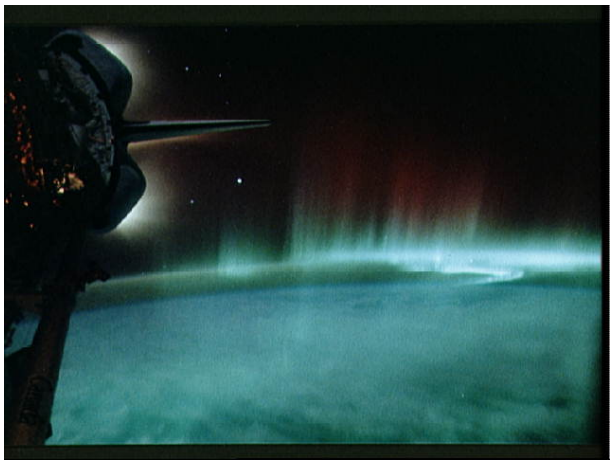

Figure 43. This image shows the Aurora Borealis as seen from the space shuttle astronauts onboard the STS-39 mission. Image courtesy of NASA.

After plotting *in-situ* data from the various solar probes, we used remote image data from the SOHO spacecraft to correlate ambient solar wind conditions with the physical state of the surface of the Sun. We used images of the solar surface in various states. First, we analyzed images taken by the Extreme Ultraviolet Imaging Telescope (EIT), which imaged the Sun at 195Å. These

images show active regions and coronal holes in bright green. We also looked at images from the Michelson Doppler Imager (MDI) experiment on board SOHO, which images the Sun in the continuous spectrum, showing the solar disc and sunspots. The MDI experiment also has a magnetogram imager, which images the Sun and showcases the magnetic polarities of different regions of the Sun, which most often correspond to sunspot groups. In addition to the solar surface, we were able to view the Sun's corona by the SOHO/LASCO telescopes C2 and C3. Using a built-in occulting disc, which simulates a solar eclipse, the telescopes are able to block out the bright sun and image only the solar corona, otherwise only visible during an actual solar eclipse. We used these images especially to see the progression of flares and CMEs from the surface of the Sun, and also to view the coronal streamers. We used the combination of these images to build a visual library of the solar cycle and correlate the solar conditions with space weather conditions.

In order to make space weather forecasts for the STEREO mission, we used data from corresponding months during the previous solar cycle. Because STEREO has launched into solar minimum conditions, we used the first five months of cycle 23 to preview the conditions that STEREO will meet during its first months of data return. Analyzing our original histograms for January through May of 1996, we were able to find a maximum and minimum range for solar wind conditions for each of the parameters studied. We were also able to determine the number of CMEs per day that STEREO should be able to capture.

Using daily, monthly, and year-long averages, 10% and 90% values, maximum ranges, and modal values, we were able to devise estimates for solar wind conditions upon initial data return from the STEREO spacecraft.

CHAPTER 4

RESULTS

4.1 SUNSPOTS AND THE SOLAR CYCLE

The concept of the solar cycle developed when astronomers noticed the changing numbers of sunspots visible on the Sun's surface. After years of watching and mapping the morphing appearance of the surface, amateur astronomers were able to identify the approximately 11 year solar cycle. With the onset of technology, scientists have been able to observe this phenomenon more closely. Using data from the National Oceanic and Atmospheric Administration's (NOAA) National Geophysical Data Center (NGDC), which has kept track of sunspot numbers since the year 1749, it can be inferred from plots that there is in fact a roughly constant cycle in sunspots dating back at least 250 years. Figure 44 shows a plot of sunspot numbers over the years 1749 through 2006.

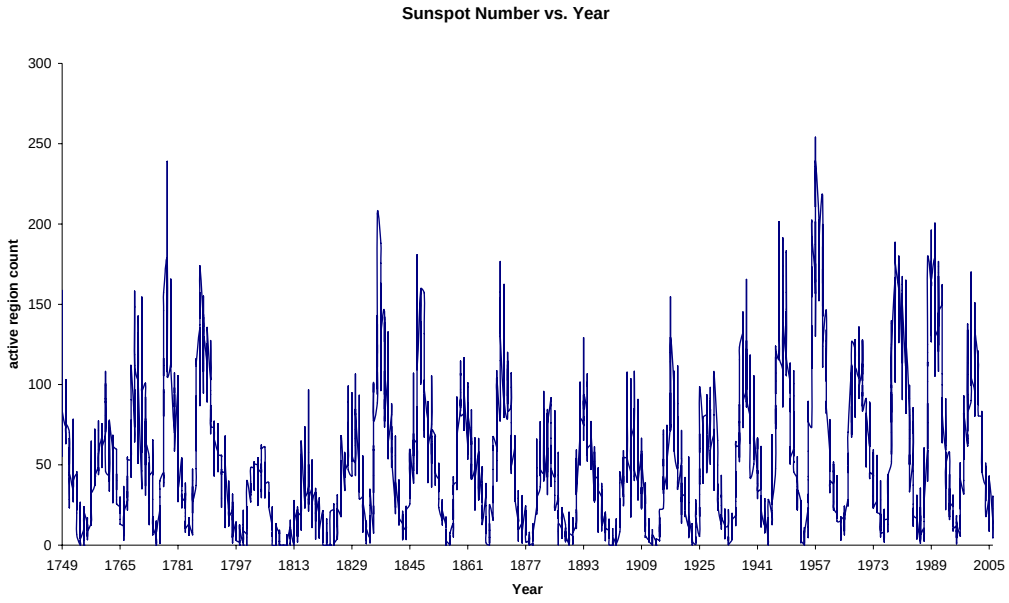

Figure 44. This plot shows the regular pattern of the approximately 11-year sunspot cycle, using data collected by NOAA since 1749.[xxxviii]

Prior to the acquisition of these data, amateur astronomers kept track of the sunspot numbers. E.W. Maunder[xxxix] studied records kept by early astronomers and discovered a period of extremely low sunspot numbers. During one thirty-year period during this lull in solar activity between the years 1645 and 1715, only 50 sunspots were observed. For comparison, in a normal thirty-year period of the Sun's life, the surface exhibits approximately 40,000 to 50,000 sunspots. This lull of 70 years is called the Maunder Minimum, and occurred simultaneously to the so-called Little Ice Age. The coincidence of the record sunspot minimum and the extremely cold winters around the world during these years has inspired debate as to whether or not sunspot number affects terrestrial climate. Figure 45 shows a plot of the record low number of sunspots noted by astronomers of the day.

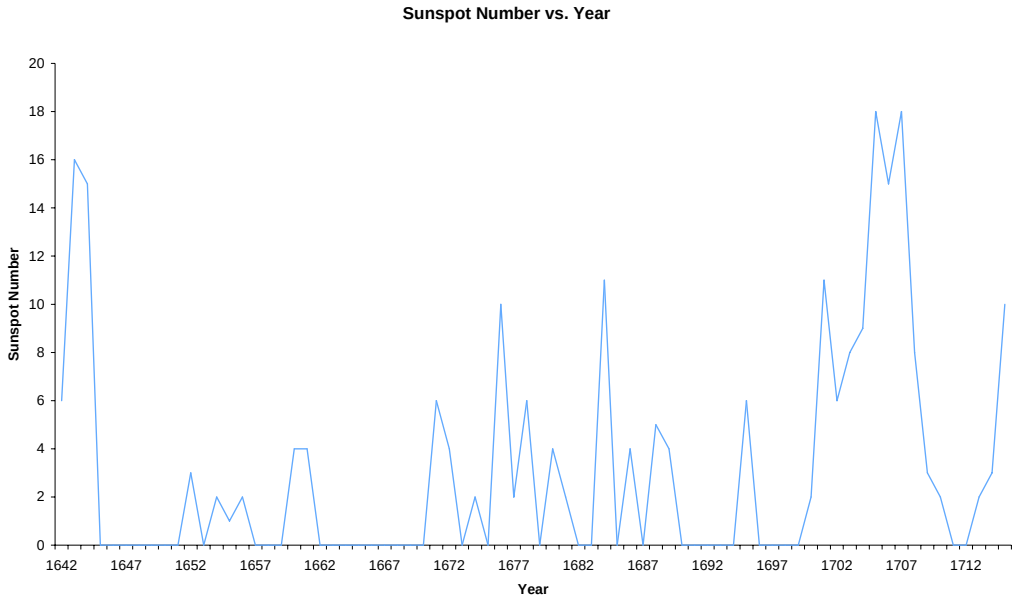

Figure 45. This plot, using data collected by NOAA from the records of amateur astronomers of the day, shows the record low numbers of sunspots observed between the years 1640 and 1715. The maximum number spotted was approximately 18 spots in one year, whereas a normal observation is at least 50 spots each year.[xl]

The most recent solar cycle, solar cycle 23, was typical of the normal 11-year sunspot cycle. In Figure 46 (and Figure 47), data provided by NOAA-NGDC are plotted to exhibit the observable curve from minimum (1996), to maximum (2001) and back to minimum (approximately 2006).

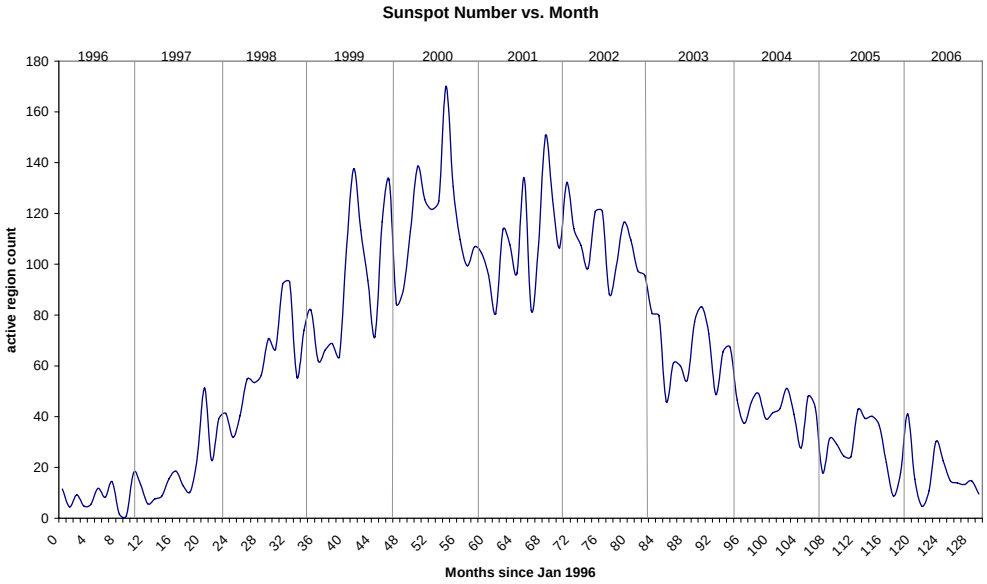

Figure 46. This plot shows the cyclical pattern of the solar cycle over the most recent solar cycle, SC23. The x-axis is measured in months since January 1996, the beginning of SC23. By the end of 2006, we approach the next cycle, SC24.

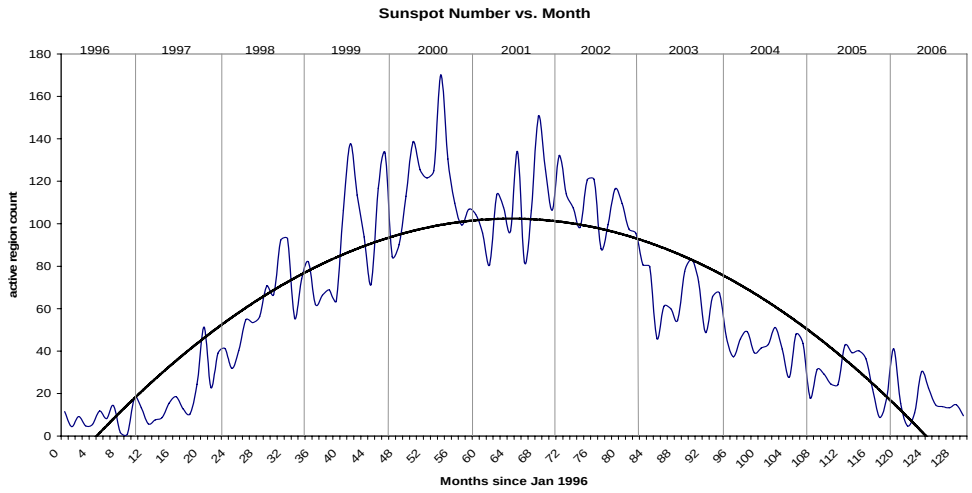

Figure 47. The plot of sunspot numbers from 1996 through 2006, fitted with a trendline, shows the rise and decline of cycle 23.

4.2 CHANGES IN THE SOLAR WIND OVER A SINGLE YEAR

In order to show long term changes in the solar wind, it is relevant to introduce the study of solar wind parameters in a short-termed manner. For this analysis, I examine several plots over the course of the year 1998, in the middle of the rising phase of the previous solar cycle (solar cycle 23). It is easy to analyze data from this particular year, due to the fact that the SOHO, Wind, and ACE spacecrafts were all orbiting at the L1 point (the location which is relevant to this thesis due to the positioning of the STEREO spacecraft) for all or part of 1998, and hence data can be correlated.

4.2.1. SOLAR WIND SPEED

Solar wind speeds during the rising phase of the solar cycle vary due to the increasingly corrupted magnetic field of the Sun. Figures 48 and 49 are a histogram of the solar wind speed values of the first Carrington Rotation of the year 1998, day-of-year 23 through 49 (which correspond to January 23 through February 18) and a plot of the solar wind speed values over this same period, respectively.

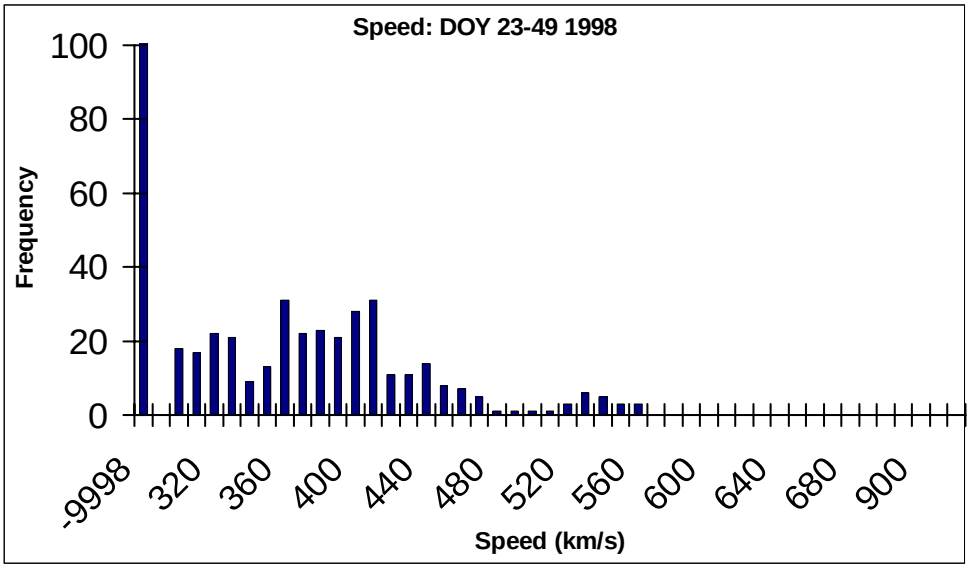

Figure 48. This histogram shows differing speed values over the first Carrington Rotation of 1998 (January 23 through February 18).

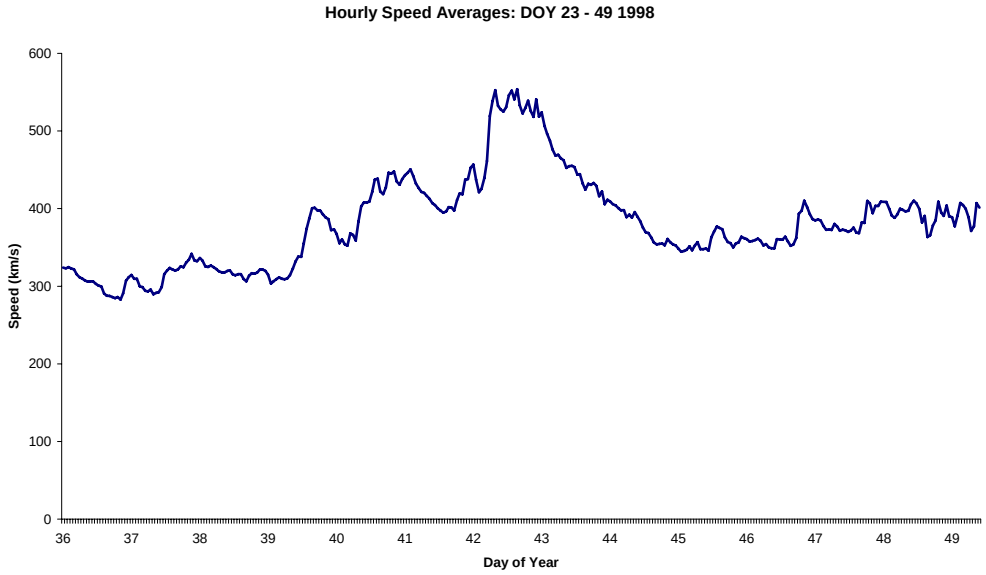

Figure 49. This plot shows solar wind speeds for the first Carrington Rotation of 1998, although the days-of-year 23 through 35 are not shown because of an instrument shut-down occurred on these days.

Figure 49 shows that most of the winds passed the ACE spacecraft between 350 and 450 km/s; this is reflected in the abundances of those speeds in

the histogram in Figure 48. Also notable is the high speed stream passing the spacecraft around DOY 43. This stream, at around and above 500 km/s, can be correlated to the small grouping of speeds that landed in the 500 and above bins of the histogram.

As a comparison, Figures 50 and 51 show a histogram of the last Carrington Rotation of the year 1998, day-of-year 347 through 08 (1999), and the corresponding plot of speed values, respectively.

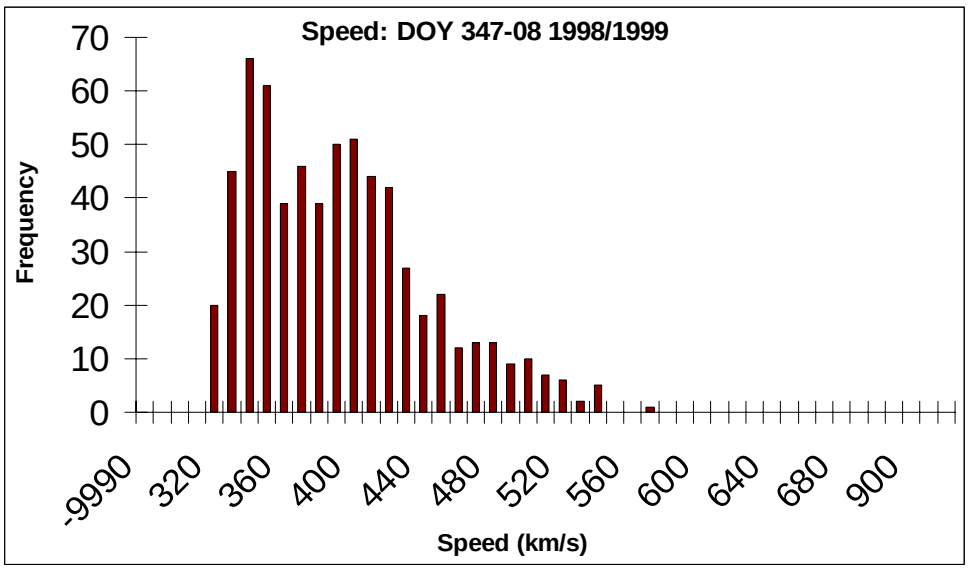

Figure 50. Abundances of the differing values of the solar wind speed during the last Carrington Rotation of the year 1998, going into 1999.

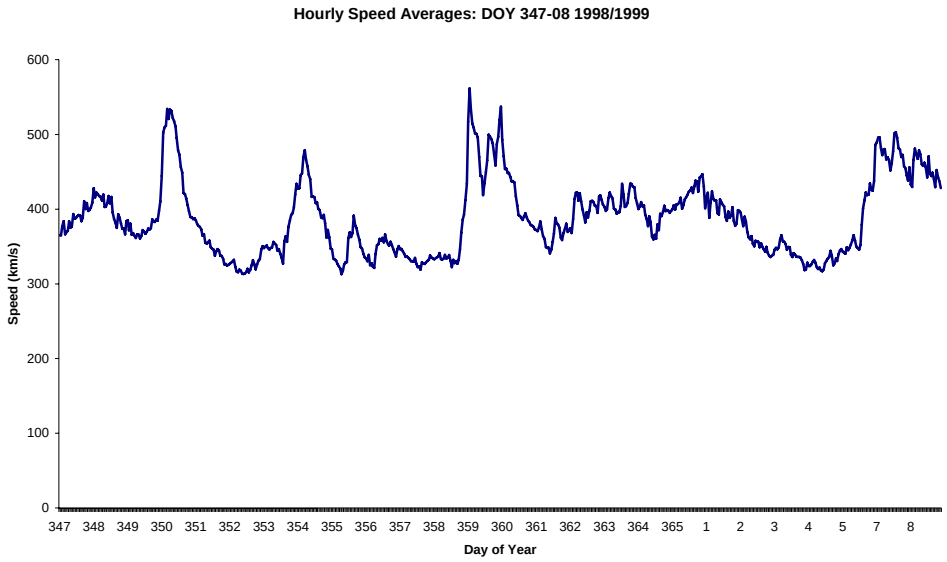

Figure 51. Speeds of the ambient solar wind over the last Carrington Rotation of the rising year of 1998.

Here at the end of the year, there are more occurrences of higher speed streams than occurred during the beginning of the year (referring back to the single large jump in speed in late January). This causes the histogram of this last rotation to be much smoother, with no beta-peaks. The increase in high-speed streams could be related to the increase in coronal holes close to the equator of the Sun, from which high speed streams originate. These coronal holes migrate toward the equator during the rising phase of the cycle, and therefore could explain the increased numbers of high speed streams flowing off of the Sun.

Figure 52 shows a histogram of total solar wind speeds for the year 1998. There are many possible wind speeds. Figure 53 shows the corresponding plot of varying values of the solar wind speed over the year 1998.

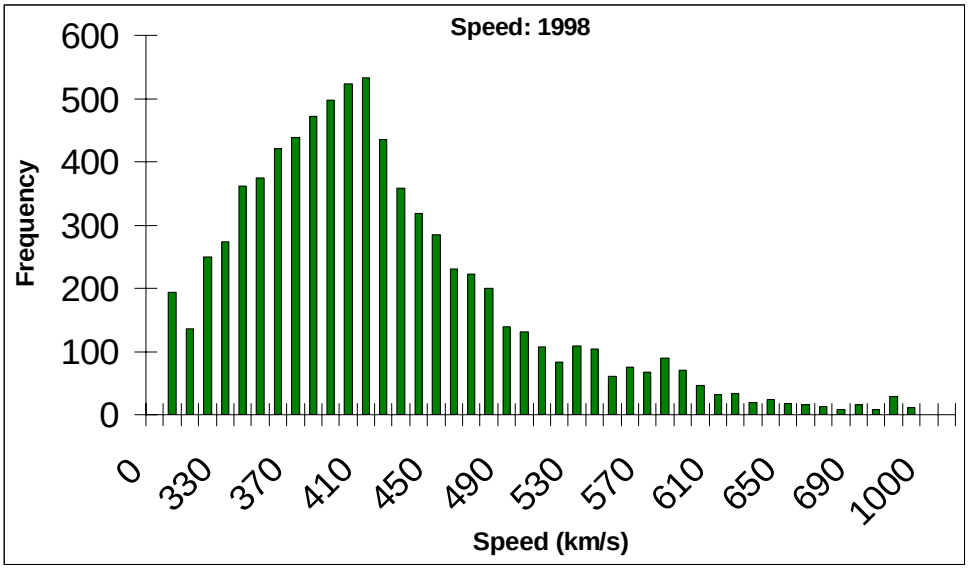

Figure 52. Distribution of all solar wind speeds over the course of the rising year of 1998.

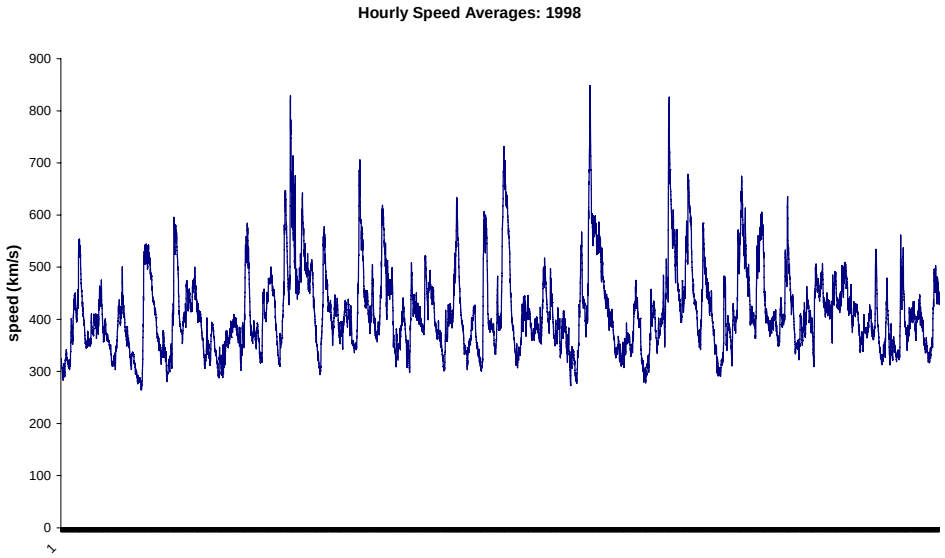

Figure 53. Plotted here are all hourly values for the solar wind speed over the entire year of 1998.

Although the individual monthly histograms of speed show irregular shapes due to individual events, the yearly histogram in Figure 52 appears smoother than the monthly graphs. The total 1998 histogram appears somewhat

like a bell-curve, with the most speeds between 350 and 500 km/s. In Figure 53, all hourly values are plotted together over the course of the year 1998. The is a slight increase in the number of high speed streams occurring at the right hand side of the plot, which corresponds to a slight rise in high speed streams between the beginning and end of 1998.

4.2.2. SOLAR WIND TEMPERATURE

Because the temperature of the solar wind is connected to the speed of the particles, temperature should change as the solar wind speed changes. As a particularly fast stream passes by, it is normally observed to have relatively high temperatures; conversely, slower streams are normally cooler. Temperature data from the SOHO spacecraft, which measures thermal speed rather than direct temperature, have been converted to degrees Kelvin using the method described in the previous section.

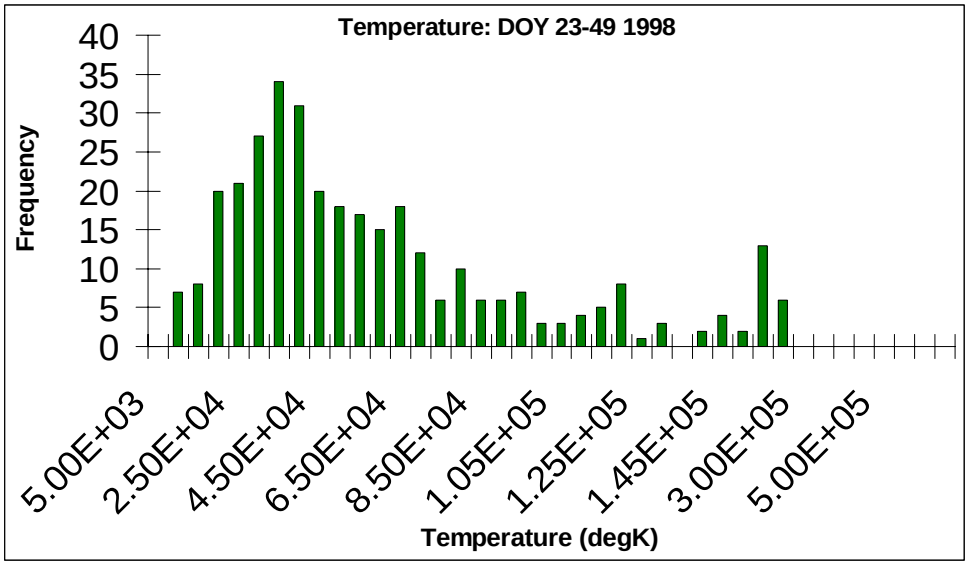

Figure 54. Distribution of temperature values over the first Carrington Rotation of 1998.

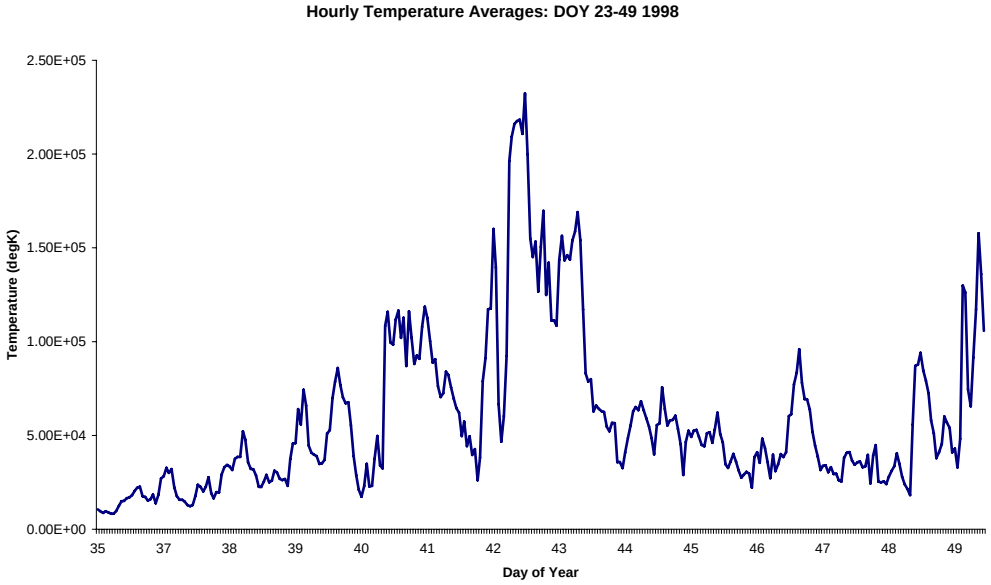

Figure 55. Solar wind speeds in real-time. Note the spike in the center of the plot, around day-of-year 43. This event is the same one that caused the spike observed in speed in Figure 6.

As observed in the histogram and plot of speed values for days 23 through 49 of 1998 (Figures 48 and 49), there is a high speed stream event that erupts at approximately day 43. This stream has an effect on the temperature of the solar

wind as well; in Figure 55, a spike in temperature at the same point also occurs at day 43. It is also possible to relate the histogram of speeds (Figure 48) to the histogram of temperatures (Figure 54). Both exhibit a β-peak in the higher values due to this streamer event on day of year 43.

As before, Figures 56 and 57 below show a histogram and plot of the temperature values over the last rotation of 1998.

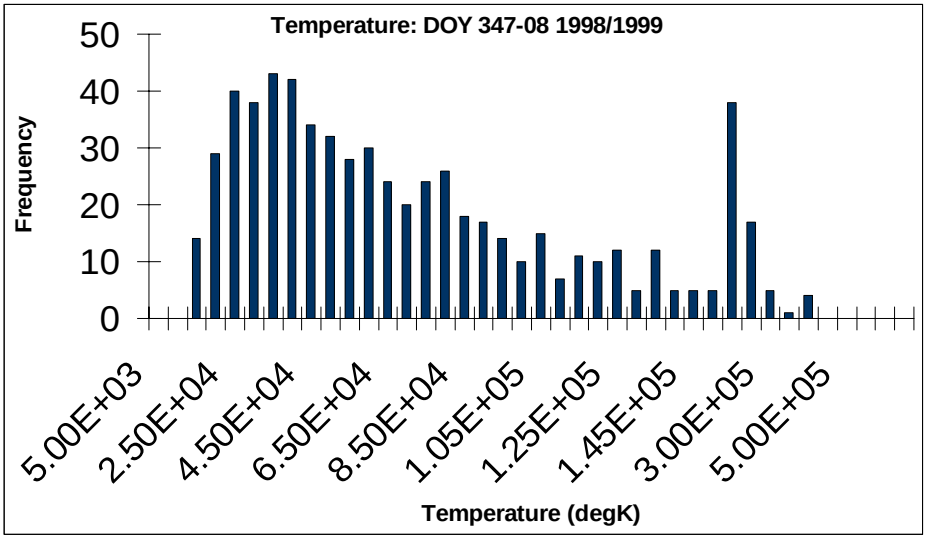

Figure 56. Range of temperature values over the final Carrington Rotation of 1998.

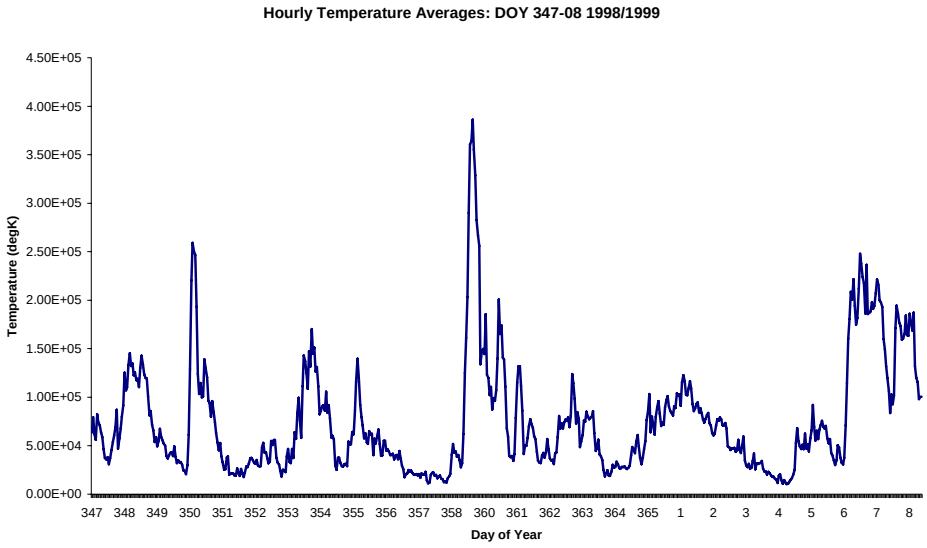

Figure 57. Temperature variation over days 347 (1998) through 08 (1999).

Although there was a high speed stream exhibited during the last Carrington Rotation of 1998 at approximate day 360 (see Figure 51), its effects were not reflected in the speed histogram for that rotation (i.e. there was no β-peak due to extreme values in Figure 50). Conversely, for the same event at day 360, the temperature of the solar wind undergoes a large change and is thus reflected in the histogram as a β-peak around temperatures of 3.0×10^5 degrees Kelvin. This example proves that temperatures and speeds can change at different rates of magnitude.

Figures 58 and 59 show the yearly values for temperature in histogram form and in plot form, respectively.

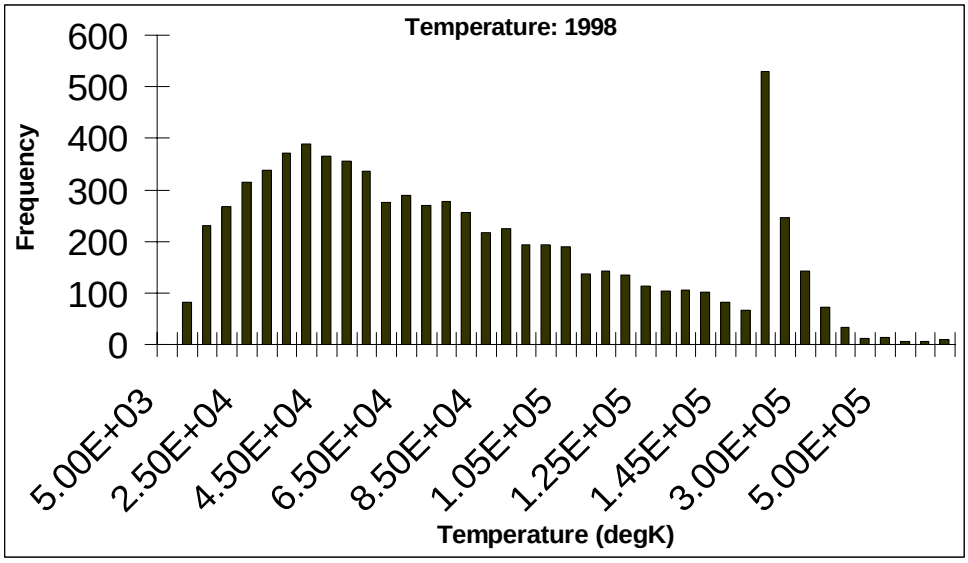

Figure 58. Range of values over which temperature values were measured during the year 1998.

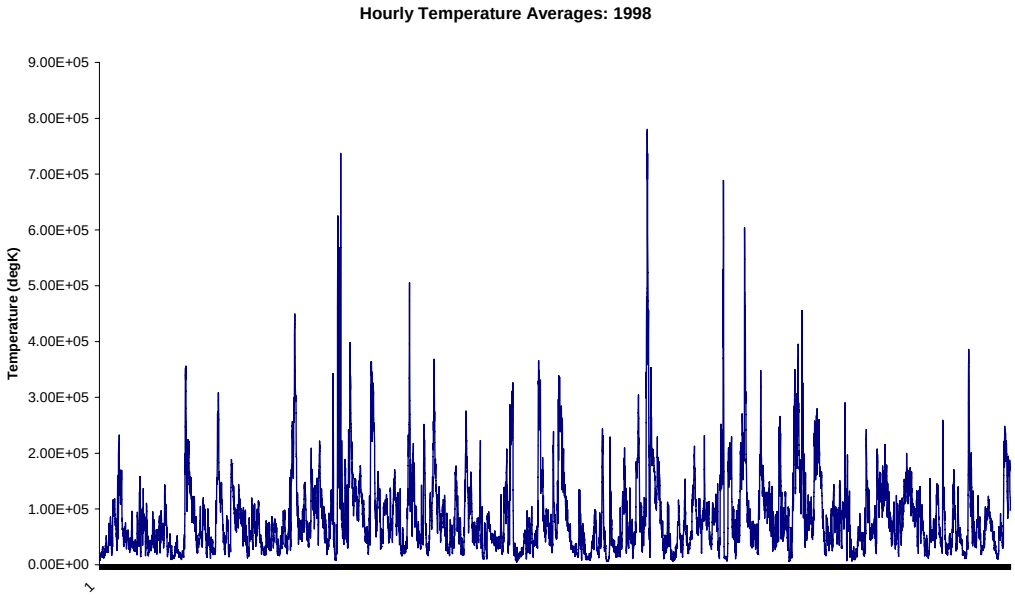

Figure 59. This plot shows the variation of the solar wind temperatures throughout 1998.

As observed in Figure 59, there are several extreme temperature spikes due to solar events, mostly towards the middle and later end of the year. These

extreme jumps cause a large β-peak in the histogram for the year (Figure 58), and temperatures as high as 8.0×10^5 degrees Kelvin.

4.2.3. SOLAR WIND DENSITY

The temperature and speed of the solar wind dictate the particle density within it. A slow, cold stream is relatively dense and contracted; a hot, fast stream is tenuous and has only a few particles per cubic centimeter.

Figures 60 and 61 show a histogram of the varying particle densities for the first rotation period of 1998 and its corresponding plot.

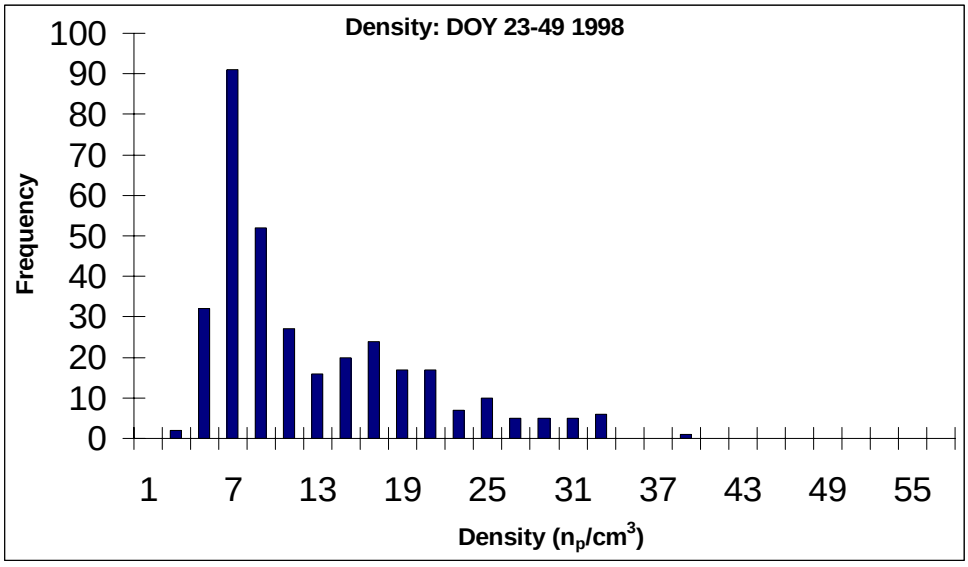

Figure 60. Range of values for the particle density of the solar wind over the first Carrington Rotation of 1998.

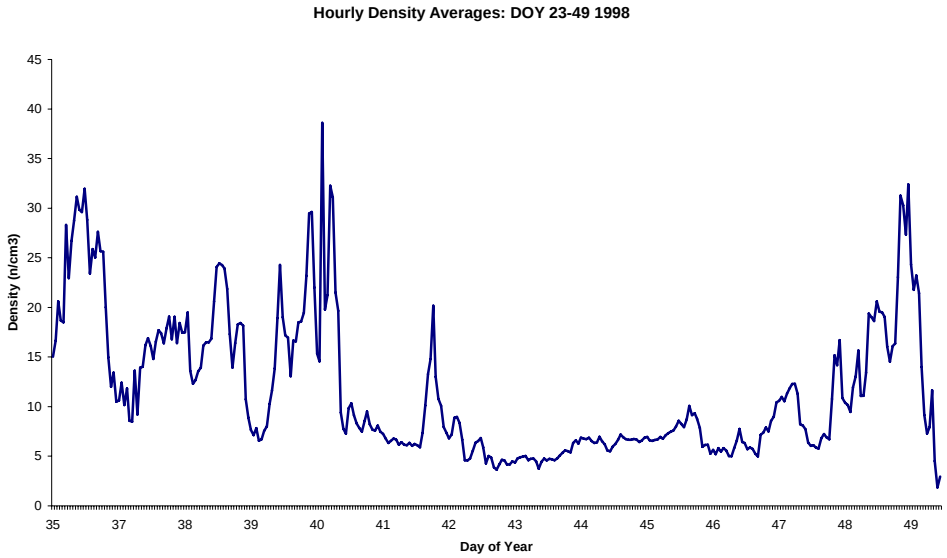

Figure 61. Solar wind particle density over the first solar rotation of 1998.

Comparing the data in Figure 61 to that in the plots in Figures 49 and 55, there is a noticeable change. In Figures 49 and 55, large spikes in amplitude of both the speed and temperature of the solar wind occurred due to the particle event on the surface of the Sun. Because this was a fast and hot stream of particles, it is to be expected that is also very tenuous. This is demonstrated in Figure 61, where it can be observed that the particle density of the wind decreases at approximate day 43, when the event began. This decrease in density is a characteristic sign of a passing CME (although it is not always the case). In this case, there were two CMEs noted for the 12th of February, although they were very poor events, so this streamer may not have been a CME.

Figures 62 and 63 show a histogram and the corresponding plot of the solar wind densities measured during the last Carrington Rotation period of 1998.

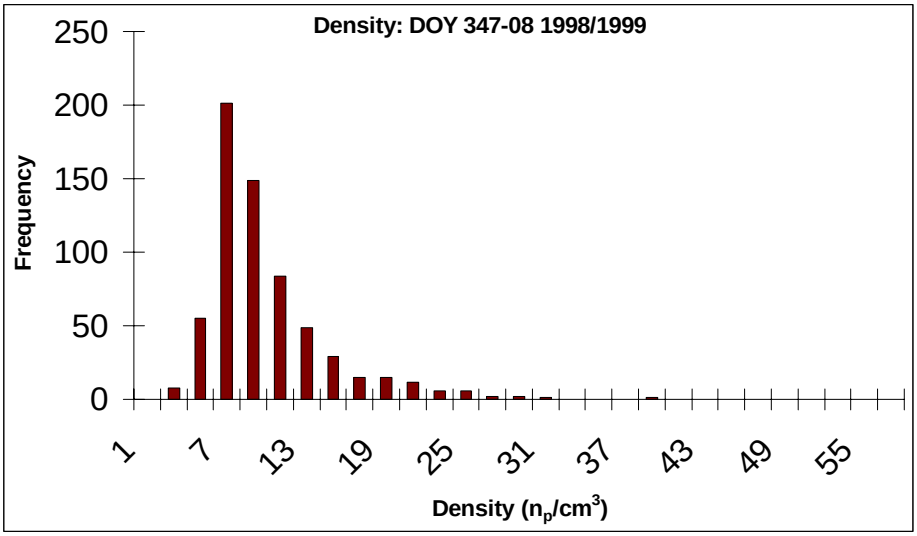

Figure 62. A histogram of density values for the last rotation of 1998.

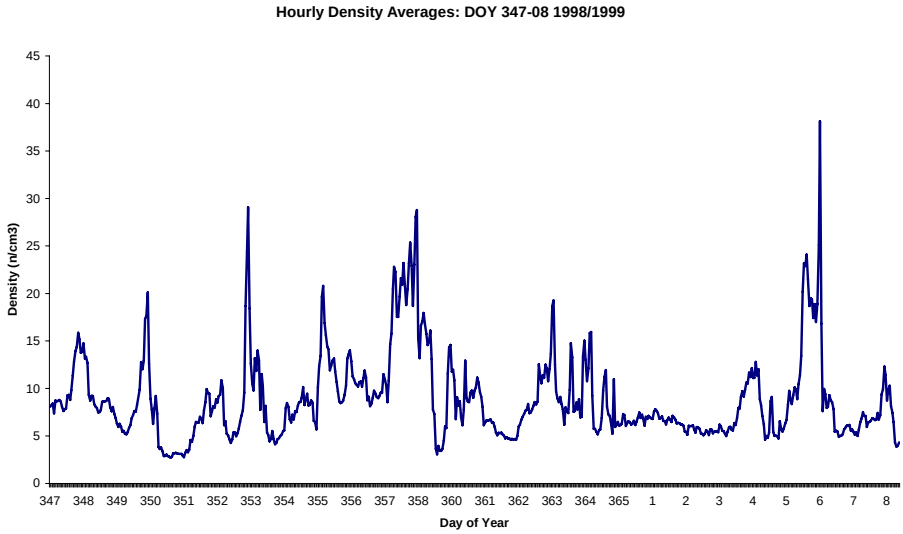

Figure 63. A plot of density shows the range of values over the course of days-of-year 347 (1998) through 08 (1999).

As in the example from the first Carrington Rotation of 1998, the density shows an opposite effect of the solar particle event around day 360 than do the plots of temperature and speed for the same day. In the plots showing speed (Figure 51) and temperature (Figure 57) for this rotation, there are significant

jumps in the values for day 360. As expected with this hot, fast stream, particle density decreases and the passing stream is relatively tenuous, exemplified by the dip in magnitude at day 360 in Figure 20.

Figures 64 and 65 show the yearly values for density in histogram form and in plot form, respectively.

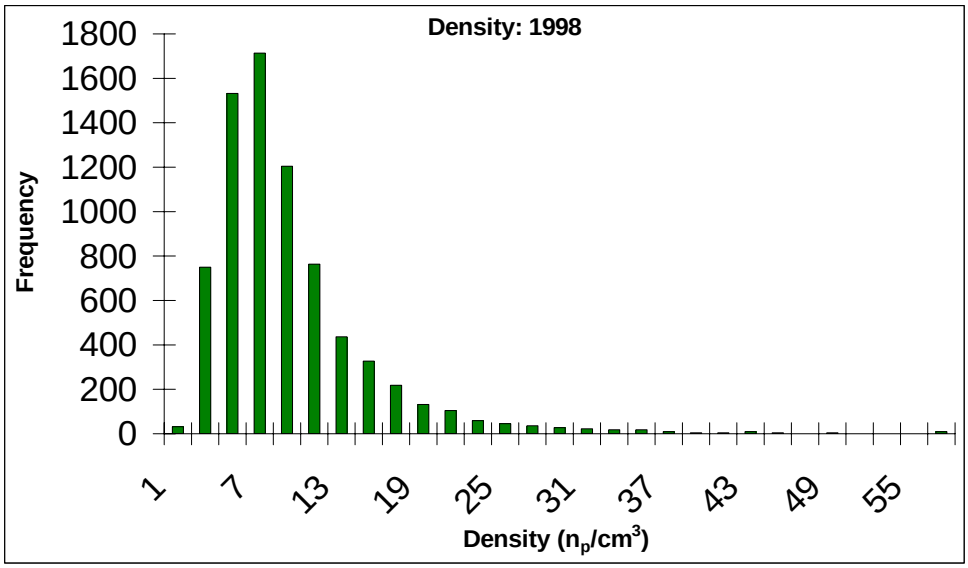

Figure 64. The range of densities of the entire year of 1998.

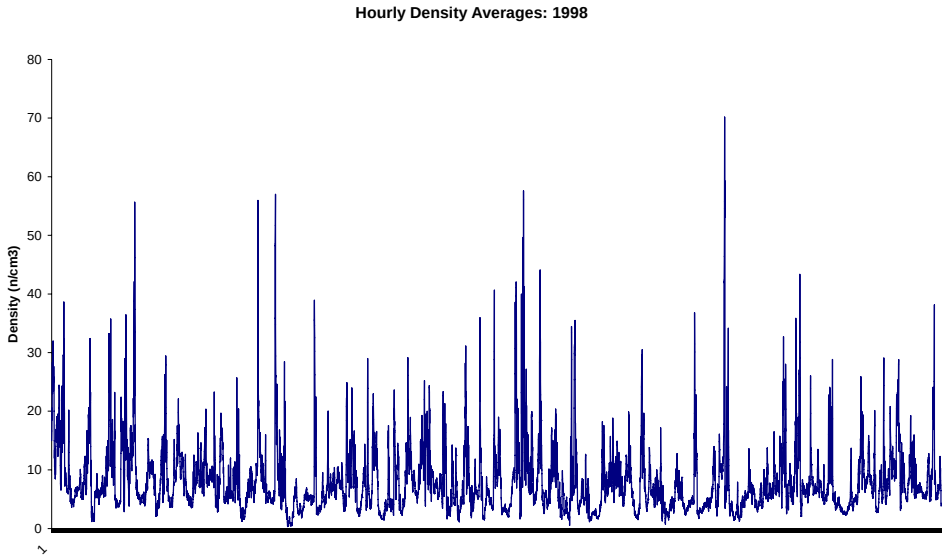

Figure 65. This plot graphs the changing particle density values over the 13 rotations of the rising year of 1998.

Unlike the full-year histograms for speed and temperature, the density histogram is somewhat bell-curve shaped. It also reflects the monthly histograms more than the other yearly histograms do. Although there are sharp changes in density, no event is long-lived enough to produce many continuous hours with extreme high or low values for density.

4.2.4 SOLAR WIND DIRECTION

The direction of the solar wind can be measured in various coordinate systems. Each of these coordinate systems gives the direction of the passing solar wind in terms an East-West (E/W) angle and a North-South (N/S) angle. Figure 66 shows the directions on the Sun's surface.

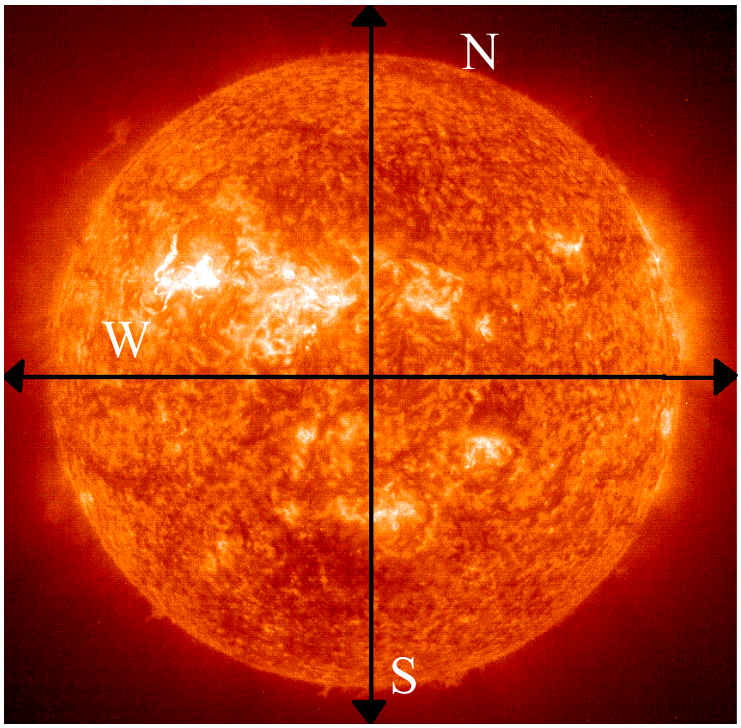

Figure 66. In this image, conventional directions are shown on the Sun for reference.

The various coordinate systems used to calculate the angle from which the solar wind flows include the Geocentric Inertial Reference Frame (GCI), the Radial Tangential Normal (RTN) spacecraft-centered coordinate system, the Geocentric Solar Magnetospheric (GSM) system, and the Geocentric Solar Ecliptic (GSE) coordinate system. The GSE is used to calculate angles in this thesis. The GSE is a 3–axis coordinate system, with Earth at its center. The *x*–axis points to the Sun, the *z*–axis is perpendicular to the ecliptic plane, and the *y*–axis is perpendicular to both the *x* and *z* axes with a positive direction opposite to the Earth's motion around the Sun. Figure 67 shows this coordinate system.

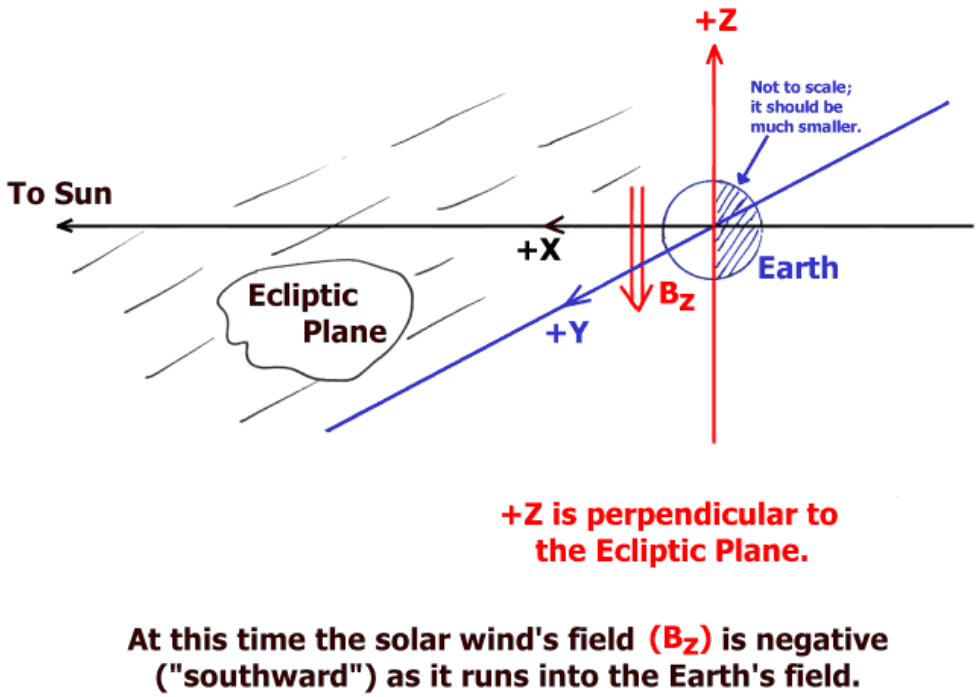

Figure 67. This illustration, courtesy of the ACE Science Center, shows the GSE coordinate system.

In the case of the SOHO spacecraft data, an onboard instrument measures the N/S angle of the wind, but no measurement is taken to find the E/W angle. The Wind spacecraft also only measures the N/S angle. The ACE spacecraft took measurements of the proton velocity vectors in the *x*, *y*, and *z* directions. With these data, it is possible to calculate the E/W and N/S angles, using the GSE coordinate system shown in Figure 68.

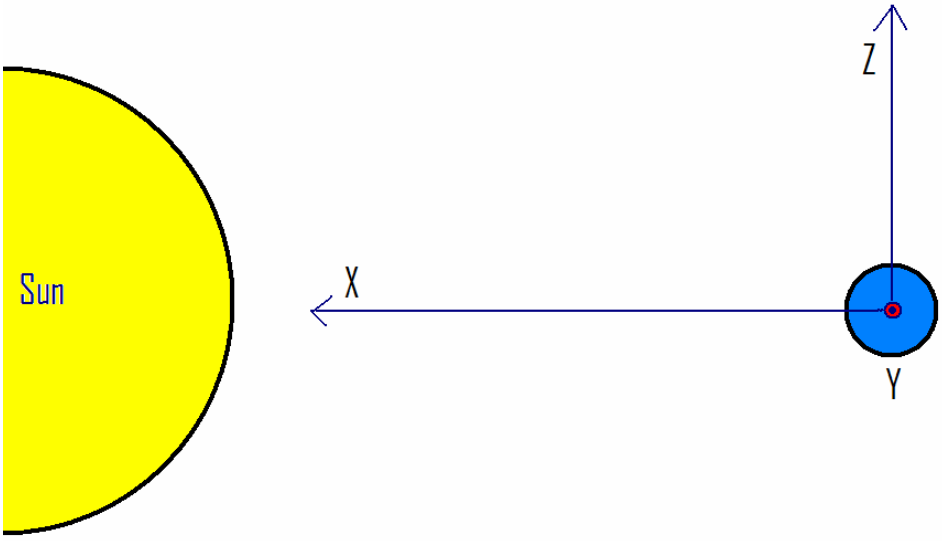

Figure 68. This schematic shows the accepted directions of the Geocentric Solar Ecliptic (GSE) coordinate system. The *x*-direction is towards the Sun; the *y*-direction points out of the page, along the tangent of the Earth's orbit; the *z*-direction is perpendicular to both the *x*- and *y*-directions, along the magnetic North pole.

The measurements taken by the ACE spacecraft (the SWEPAM instrument specifically) included wind velocity in each of the vector directions, V_x, V_y, and V_z. Using the direction schematic above in Figure 68, the corresponding E/W and N/S angles of the wind were determined by:

$$\theta_{EW} = \tan^{-1}\left(\frac{V_Y}{V_X}\right) \times 180 \text{ (in degrees)} \quad (2)$$

$$\theta_{NS} = \tan^{-1}\left(\frac{V_Z}{V_X}\right) \times 180 \text{ (in degrees)} \quad (3)$$

Thus, a positive E/W angle translates to a solar wind flowing from the west of the Sun, while a negative angle translates to a solar wind stream coming from the east of the Sun. Likewise, a positive N/S angle translates to a solar wind

stream from the north of the Sun, and a negative angle corresponds to a stream having originated in the south.

Examples of changing stream directions are illustrated in Figures 69 and 70, which show the E/W and N/S angles of January 1998, and in Figures 71 and 72, which show the same parameters during the last Carrington Rotation of 1998.

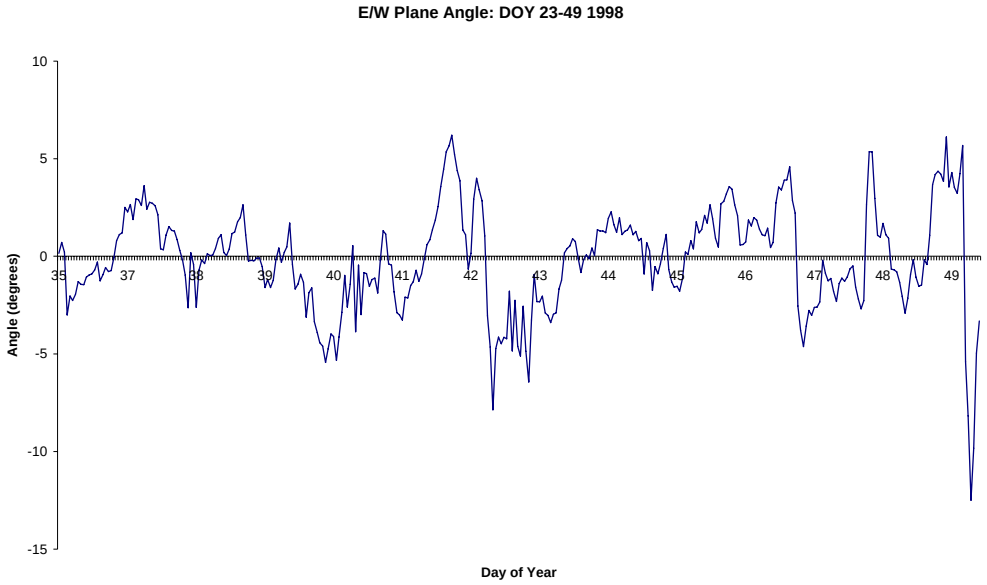

Figure 69. Spread of solar wind direction in terms of the East-West angle of the flow of the wind. Negative angles represent wind flowing from the East of the Sun, while positive angles represent wind flowing from the West.

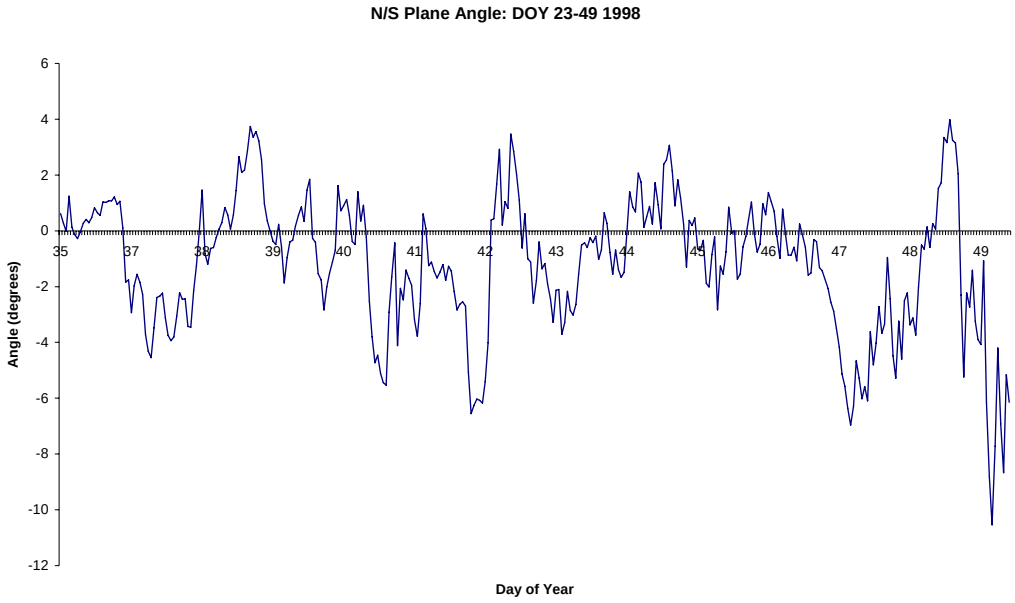

Figure 70. Directions of the solar wind in terms of the North-South direction. Negative values correspond to winds flowing from the south of the Sun; positive values correspond to wind flowing from the northern hemisphere of the Sun.

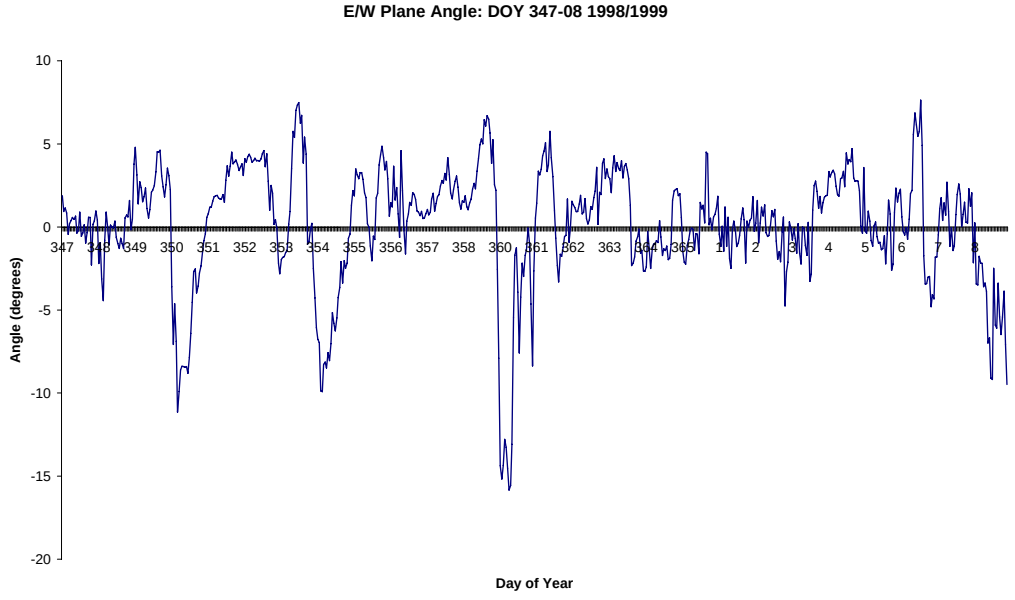

Figure 71. East-west directions of the solar wind for the last rotation of the year 1998.

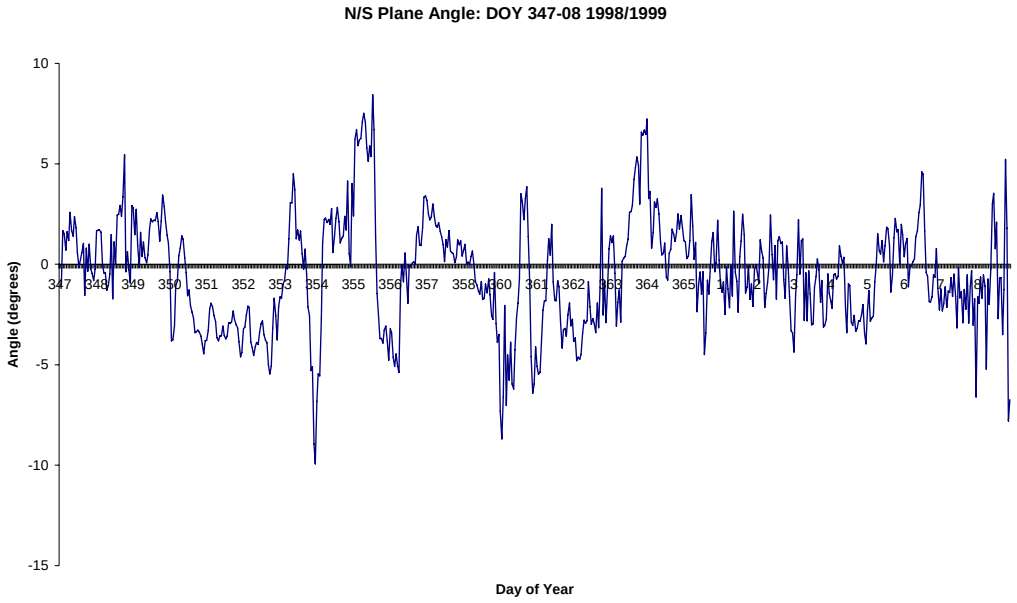

Figure 72. North-south direction of the solar wind during the final Carrington Rotation of 1998.

Due to the increasingly perturbed current sheet around the Sun during the rising phase in 1998, it can be observed that the directions of the solar wind fluctuated greatly in 1998 with changing E/W angles and N/S angles, shown in Figures 73 and 74 respectively.

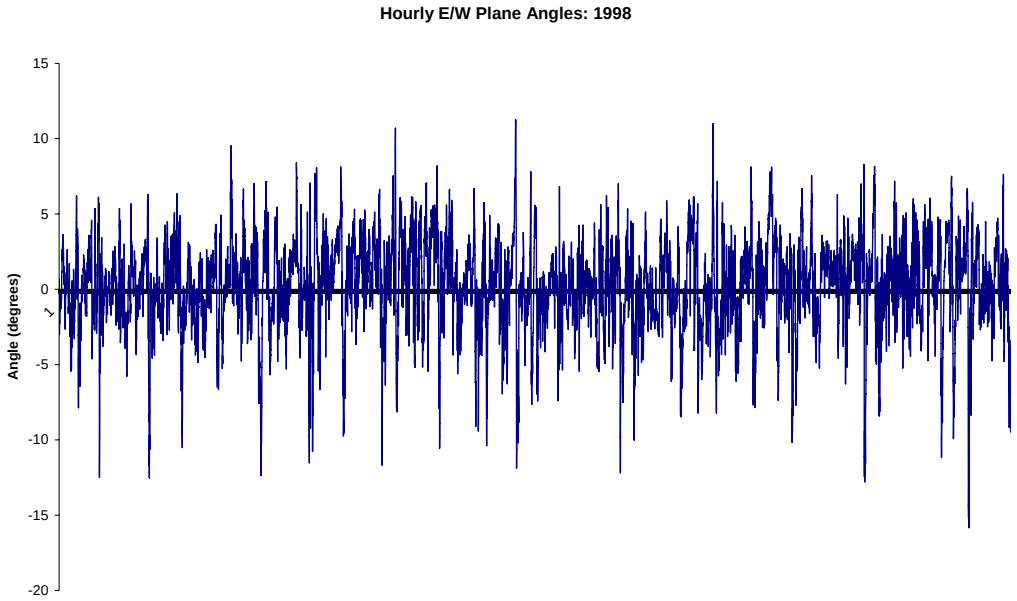

Figure 73. Varying direction of the solar wind in the East-West plane over the year 1998.

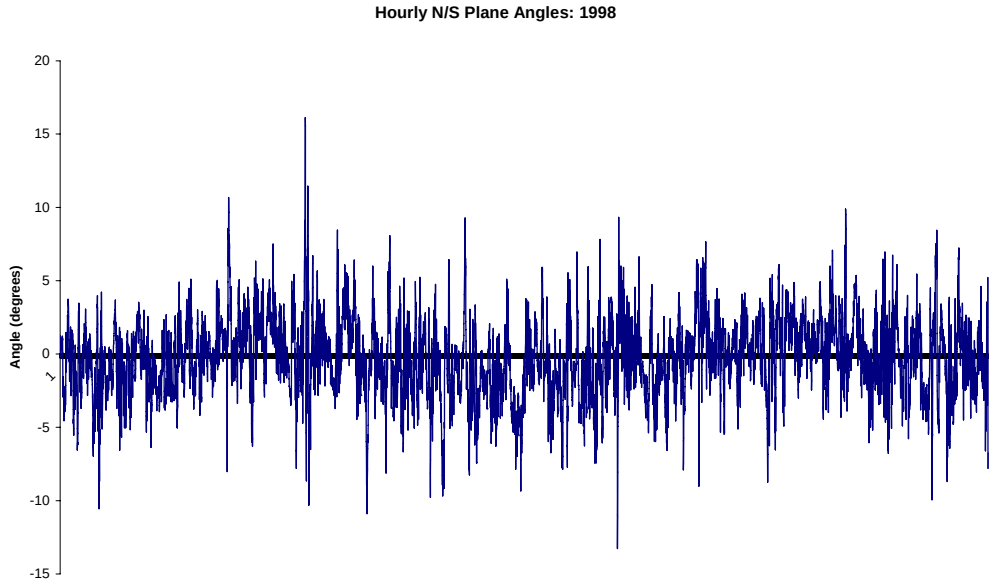

Figure 74. Changes in the North-South plane angle of the flow of the solar wind during 1998.

Figures 73 and 74, show a slight increase in the extremity of angles from which the wind flows that increases toward the latter half of the rising year 1998.

The flow of particles from increasingly high latitudes (northern and southern) on the Sun is caused by the growing perturbation of the current sheet around the Sun. The current sheet begins at minimum as a relatively flat sheet extending from the solar equator on the Earth-Sun line, but progresses and becomes more turbulent as the cycle rises. In the latter half of the year 1998, both east-west and north-south angles experienced greater flow angles than during the first half of the year.

4.3. COMPARING THE YEARS: 1996 THROUGH 2006

To quantify the changes over the solar cycle, histograms of each parameter measured by the various spacecrafts and instruments are compared. To illustrate the changes, it is appropriate to examine a single month per year to examine the changes that have occurred in one year during the cycle. The following histograms use data taken by the spacecrafts each May from 1996 through 2006.

4.3.1. SOLAR WIND SPEED

Figures 75a through k show histograms of varying speed values in the month of May for each year in solar cycle 23 (1996-2006). The data from years 1996 and 1997 are taken from the SWE instrument on the Wind spacecraft, and the following years (through present) are given by the SWEPAM instrument on the ACE spacecraft.

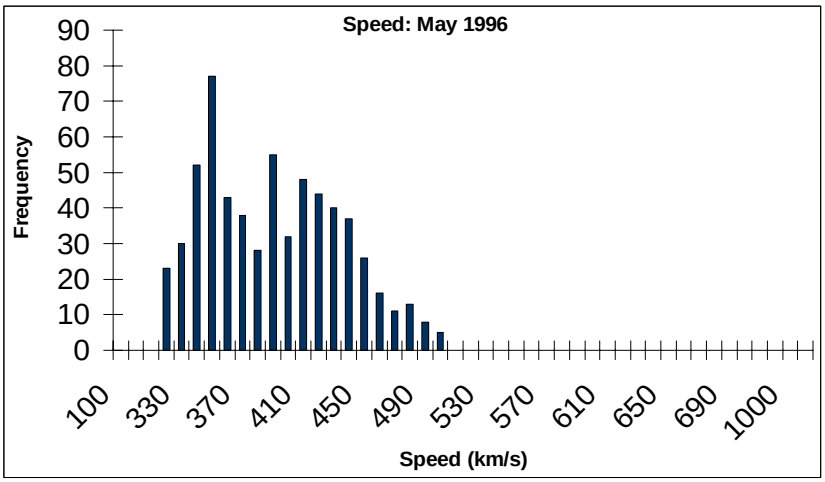
Speed: May 1996
Frequency
90
80
70
60
50
40
30
20
10
0
100
330
370
410
450
490
530
570
610
650
690
1000
Speed (km/s)

(a)

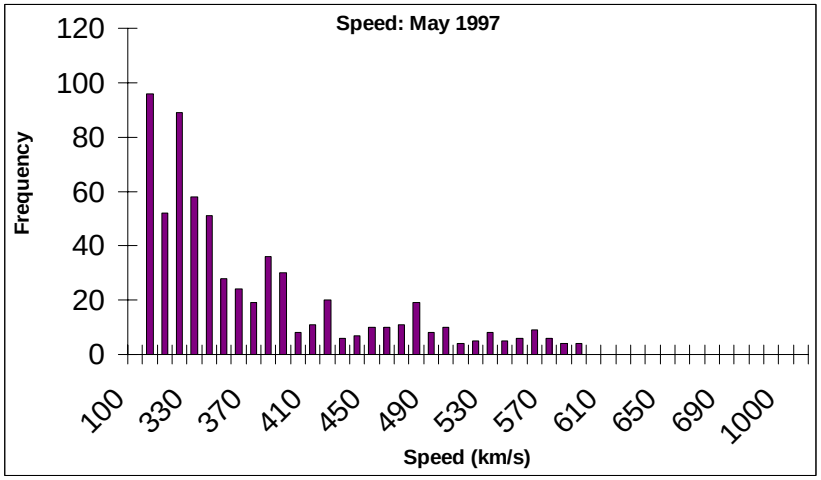
Speed: May 1997
Frequency
120
100
80
60
40
20
0
100
330
370
410
450
490
530
570
610
650
690
1000
Speed (km/s)

(b)

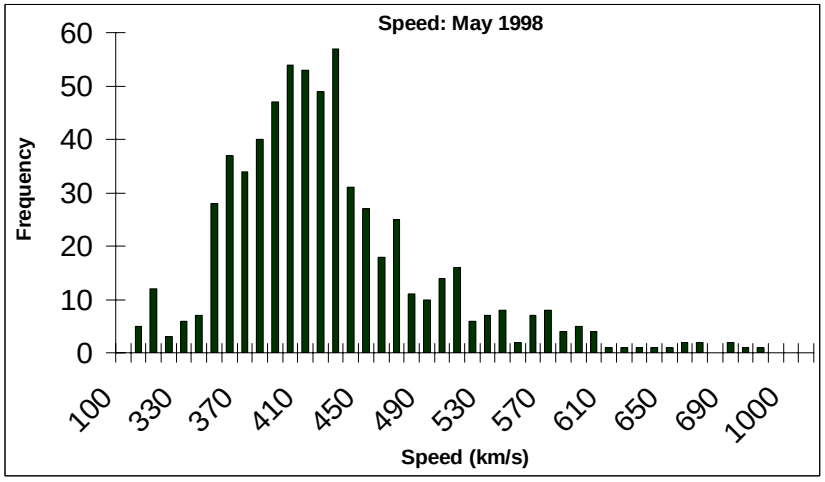
Speed: May 1998
Frequency
60
50
40
30
20
10
0
100
330
370
410
450
490
530
570
610
650
690
1000
Speed (km/s)

(c)

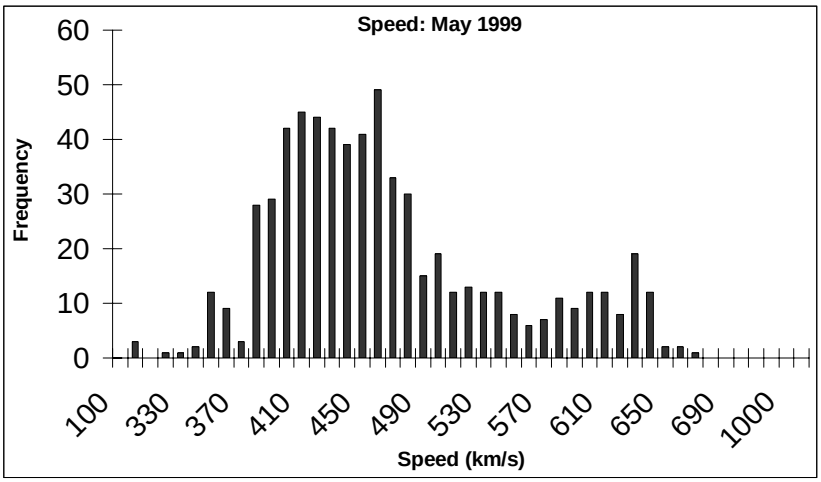
Speed: May 1999
Frequency
60
50
40
30
20
10
0
100
330
370
410
450
490
530
570
610
650
690
1000
Speed (km/s)

(d)

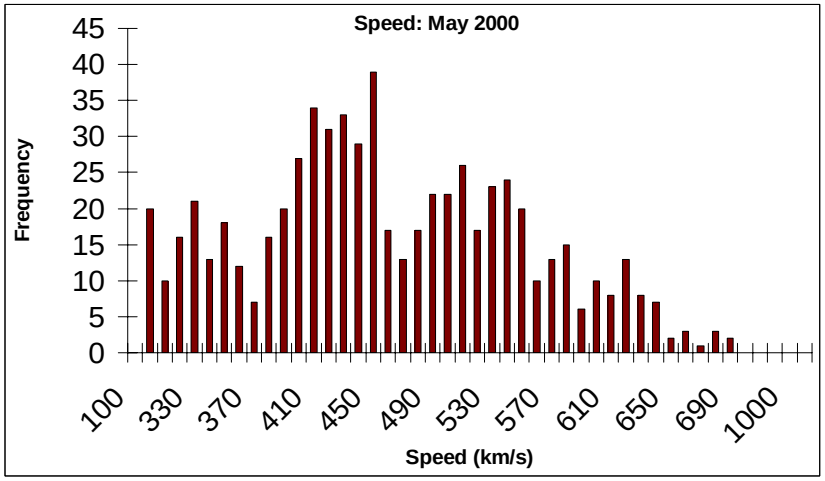
Speed: May 2000
Frequency
45
40
35
30
25
20
15
10
5
0
100
330
370
410
450
490
530
570
610
650
690
1000
Speed (km/s)

(e)

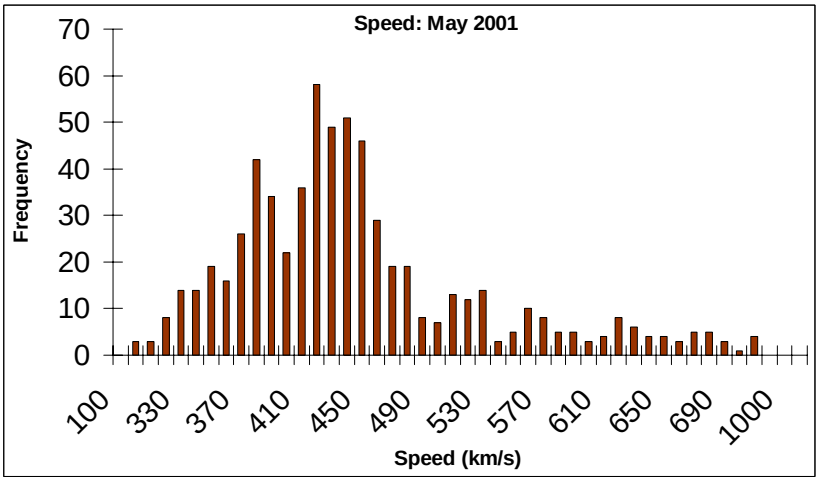
Speed: May 2001
Frequency
70
60
50
40
30
20
10
0
100
330
370
410
450
490
530
570
610
650
690
1000
Speed (km/s)

(f)

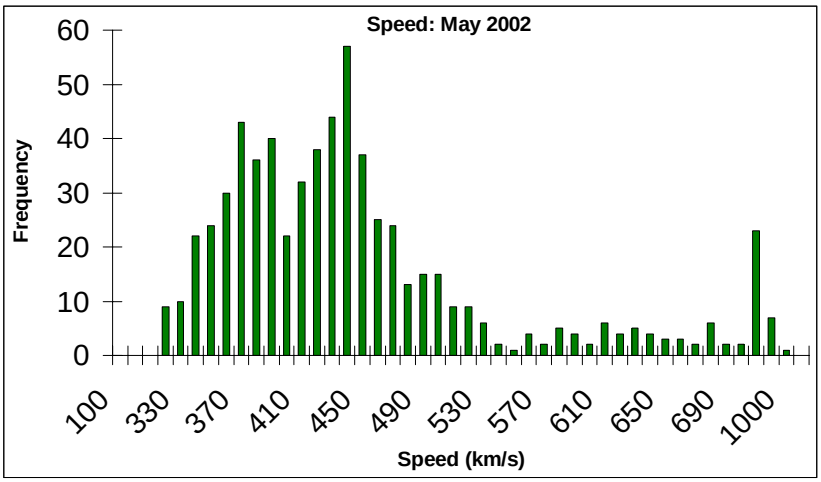
Speed: May 2002
Frequency
60
50
40
30
20
10
0
100
330
370
410
450
490
530
570
610
650
690
1000
Speed (km/s)

(g)

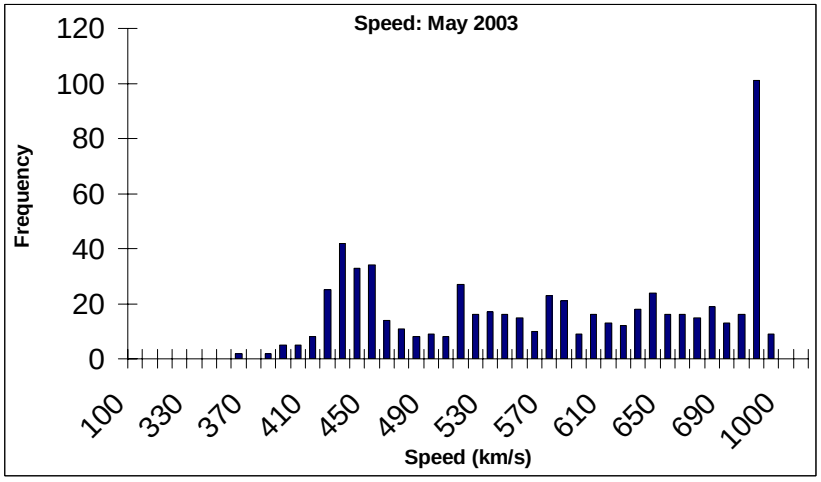
Speed: May 2003
Frequency
120
100
80
60
40
20
0
100
330
370
410
450
490
530
570
610
650
690
1000
Speed (km/s)

(h)

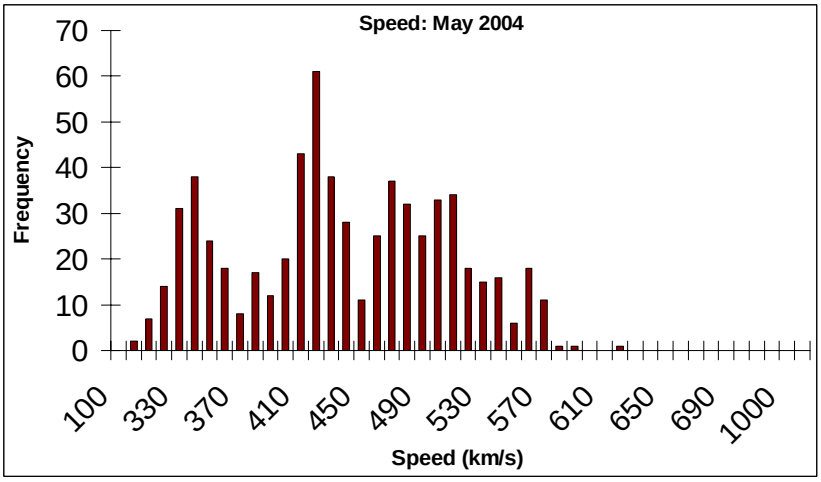
Speed: May 2004
Frequency
70
60
50
40
30
20
10
0
100
330
370
410
450
490
530
570
610
650
690
1000
Speed (km/s)

(i)

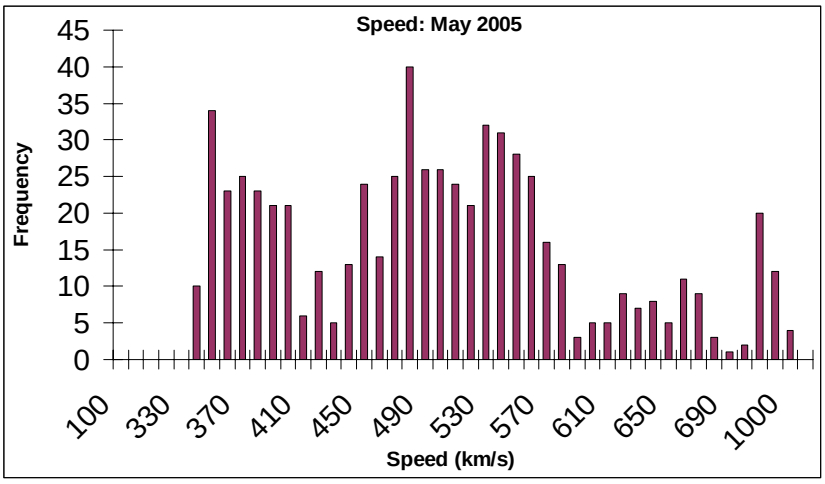

(j)

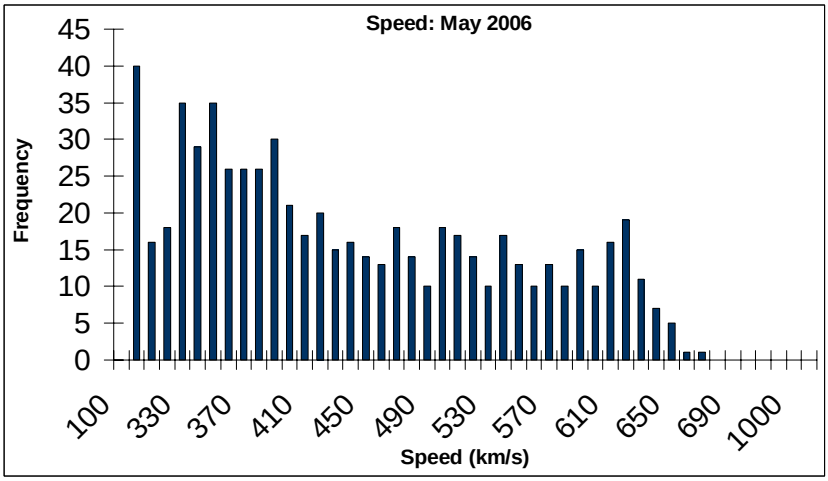

(k)

Figure 75. Figures 32a through 32k show histograms of varying speed values in the month of May for each year in solar cycle 23 (1996 through 2006). This illustrates the change experienced by the solar wind in the speed parameter over a solar cycle.

Speed ranges widely at all times during the solar cycle. Although all phases of the cycle exhibit a mix of fast and slow streams, it is possible to make several observations using these histograms. The declining phase of the cycle from approximately 2002 to 2006 spent the most overall hours in fast speed streams. Although the solar maximum years, 2000 and 2001, show great

extremes of speed and a great spread of values, the years following the maximum exhibit the greatest net speed. The histograms from 1996 and 1997, during the last solar minimum and rising phase, are noticeably thinner than the other years. Although the latter may be caused by the fact that these data are from the Wind spacecraft, it is more likely caused by the minimal activity going on at the time. Due to decreased solar activity, there are not many high speed streams observed in these years. Another notable observation is that 2002, 2003, and 2005 exhibit several hours of extremely high speed streams, each spending about 25 to 100 hours at approximately 1000 km/s. In the middle of these years, in 2004, the speed does not rise above 650 km/s. Low speeds vary greatly as well; ranges for the low end of speed vary from approximately 200 km/s in 1997 through 2001 to about 380 km/s in 2003. In terms of the speed of the solar wind over the solar cycle, changes must occur gradually, and therefore on a large, yearly scale, the effects of the solar cycle on speed may not be observed as well.

4.3.2. SOLAR WIND TEMPERATURE

Figures 76a through k show histograms of data taken each May over the course of solar cycle 23. As in the solar wind speed readings, 1996 and 1997 data are given by the Wind spacecraft; 1998 through 2006 data are taken from the ACE spacecraft.

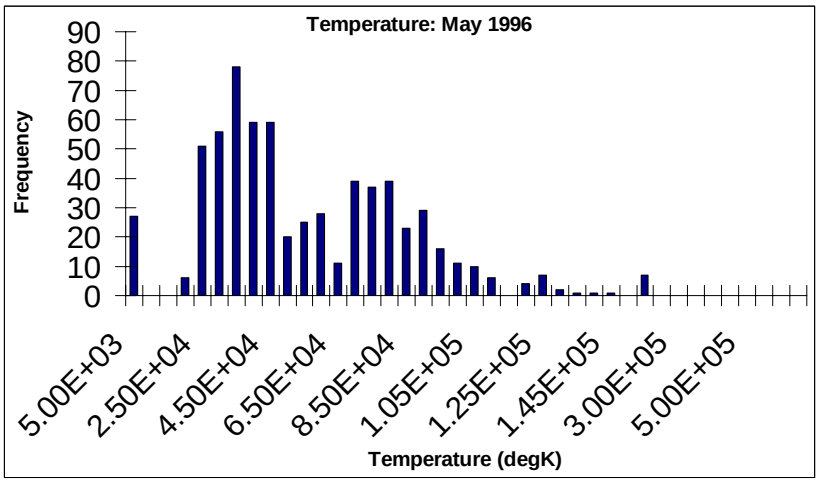
Temperature: May 1996
Frequency
90
80
70
60
50
40
30
20
10
0
5.00E+03
2.50E+04
4.50E+04
6.50E+04
8.50E+04
1.05E+05
1.25E+05
1.45E+05
3.00E+05
5.00E+05
Temperature (degK)

(a)

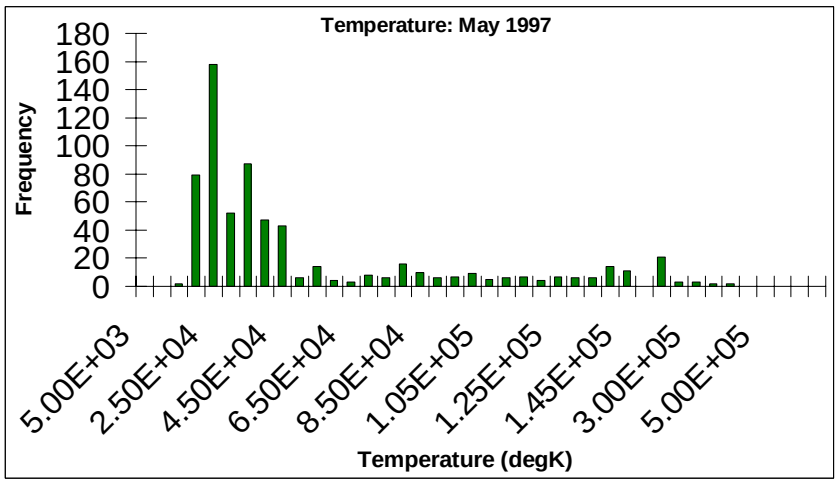
Temperature: May 1997
Frequency
180
160
140
120
100
80
60
40
20
0
5.00E+03
2.50E+04
4.50E+04
6.50E+04
8.50E+04
1.05E+05
1.25E+05
1.45E+05
3.00E+05
5.00E+05
Temperature (degK)

(b)

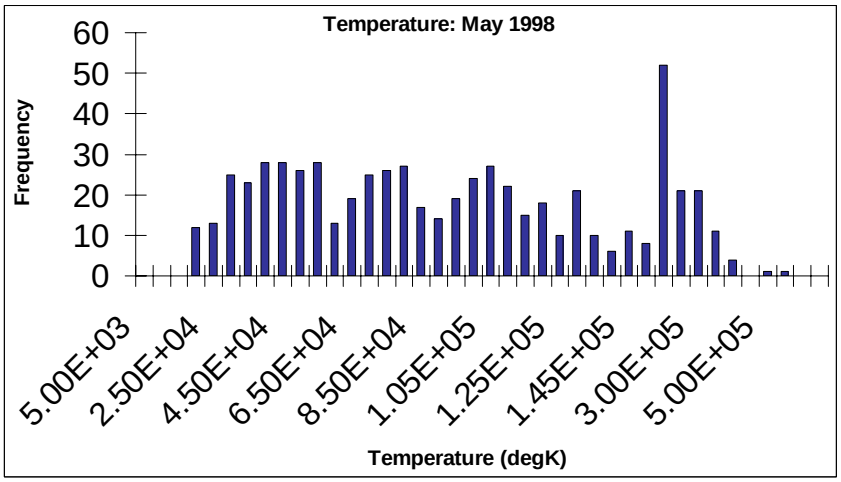
Temperature: May 1998
Frequency
60
50
40
30
20
10
0
5.00E+03
2.50E+04
4.50E+04
6.50E+04
8.50E+04
1.05E+05
1.25E+05
1.45E+05
3.00E+05
5.00E+05
Temperature (degK)

(c)

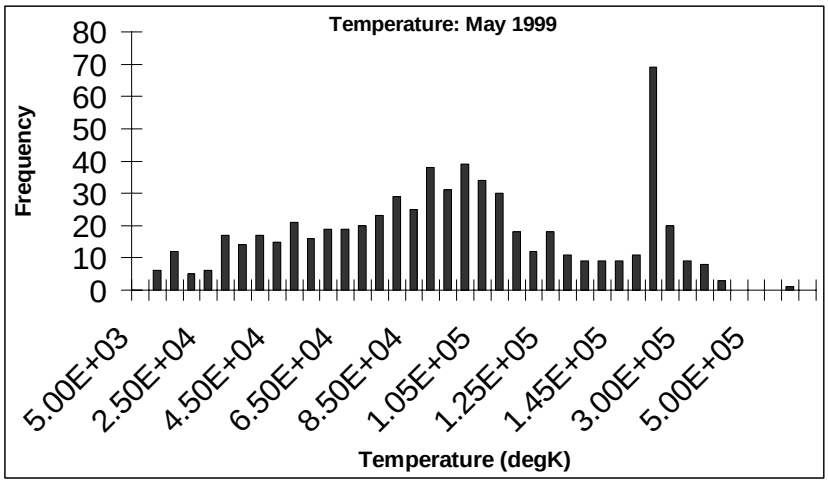
Temperature: May 1999
Frequency
80
70
60
50
40
30
20
10
0
5.00E+03
2.50E+04
4.50E+04
6.50E+04
8.50E+04
1.05E+05
1.25E+05
1.45E+05
3.00E+05
5.00E+05
Temperature (degK)

(d)

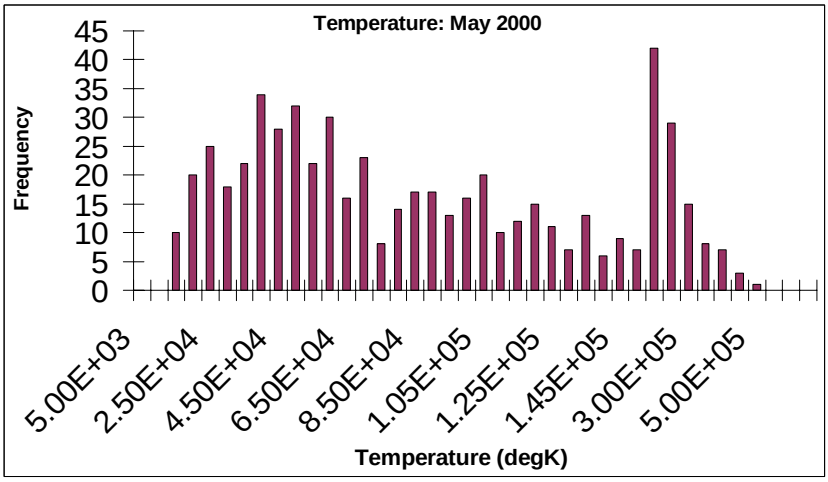
Temperature: May 2000
Frequency
45
40
35
30
25
20
15
10
5
0
5.00E+03
2.50E+04
4.50E+04
6.50E+04
8.50E+04
1.05E+05
1.25E+05
1.45E+05
3.00E+05
5.00E+05
Temperature (degK)

(e)

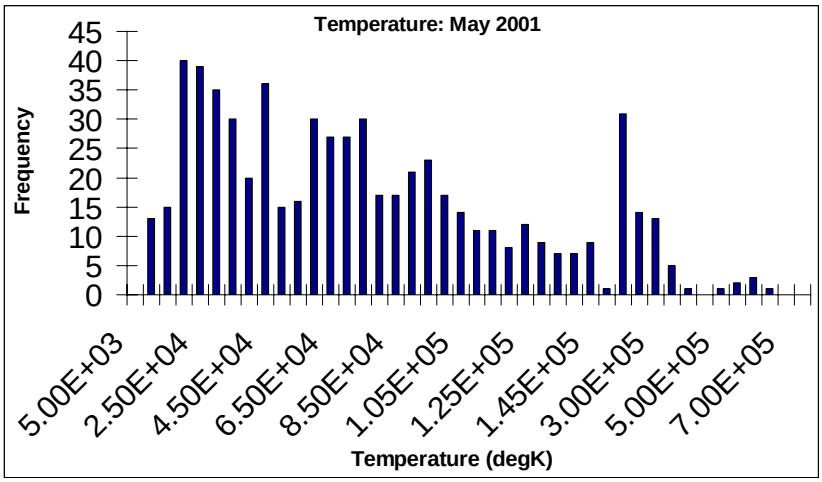
Temperature: May 2001
Frequency
45
40
35
30
25
20
15
10
5
0
5.00E+03
2.50E+04
4.50E+04
6.50E+04
8.50E+04
1.05E+05
1.25E+05
1.45E+05
3.00E+05
5.00E+05
7.00E+05
Temperature (degK)

(f)

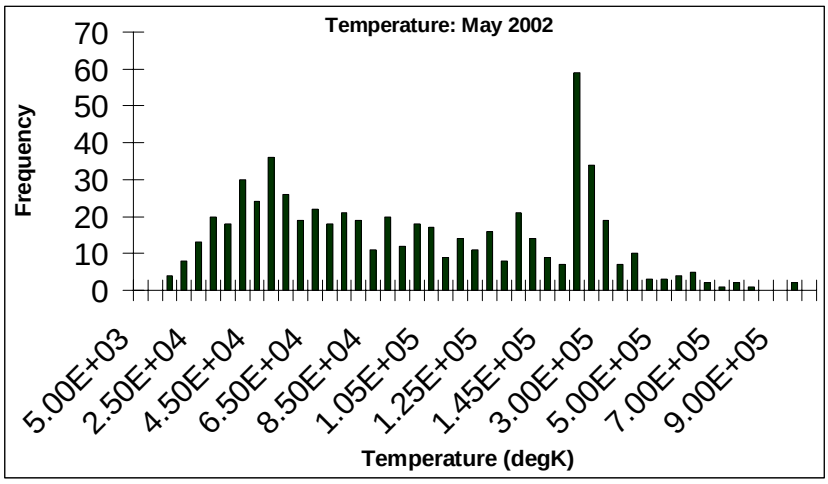
Temperature: May 2002
Frequency
70
60
50
40
30
20
10
0
5.00E+03
2.50E+04
4.50E+04
6.50E+04
8.50E+04
1.05E+05
1.25E+05
1.45E+05
3.00E+05
5.00E+05
7.00E+05
9.00E+05
Temperature (degK)

(g)

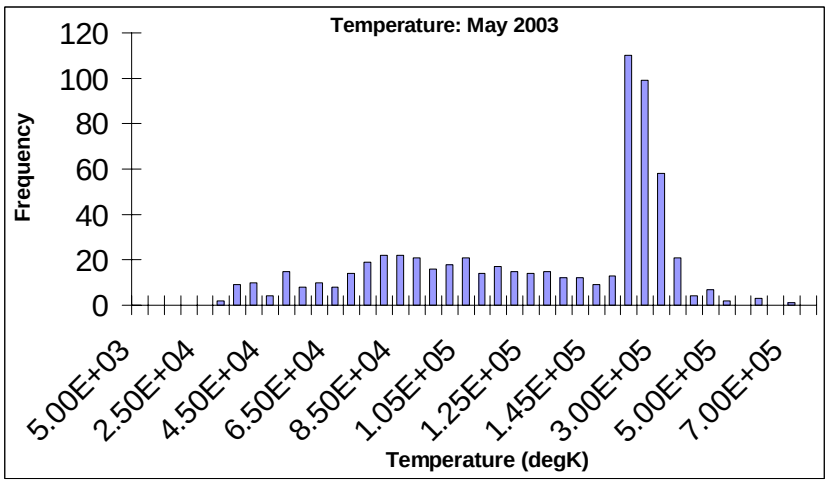
Temperature: May 2003
Frequency
120
100
80
60
40
20
0
5.00E+03
2.50E+04
4.50E+04
6.50E+04
8.50E+04
1.05E+05
1.25E+05
1.45E+05
3.00E+05
5.00E+05
7.00E+05
Temperature (degK)

(h)

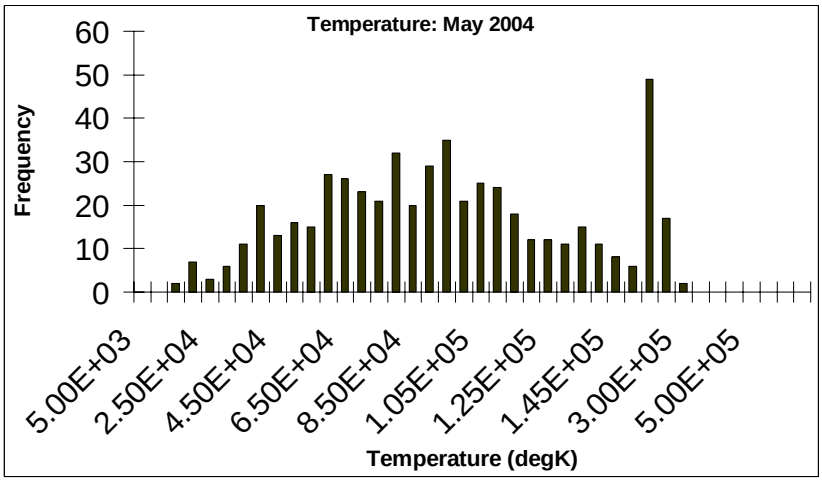
Temperature: May 2004
Frequency
60
50
40
30
20
10
0
5.00E+03
2.50E+04
4.50E+04
6.50E+04
8.50E+04
1.05E+05
1.25E+05
1.45E+05
3.00E+05
5.00E+05
Temperature (degK)

(i)

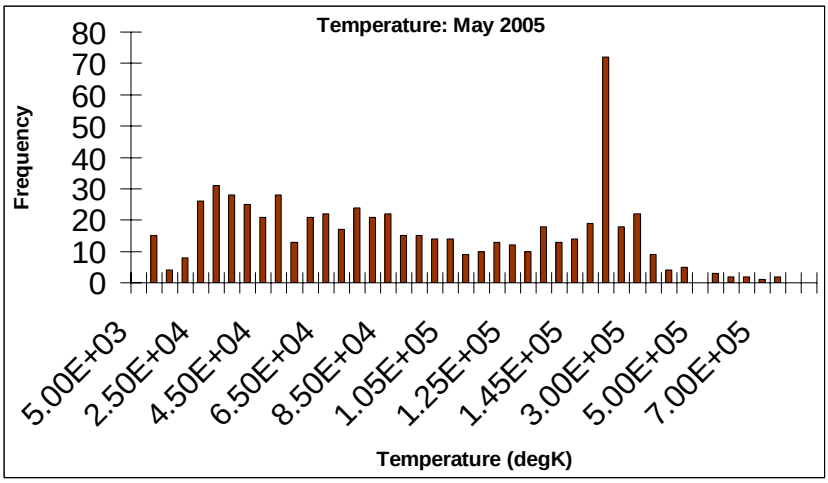

(j)

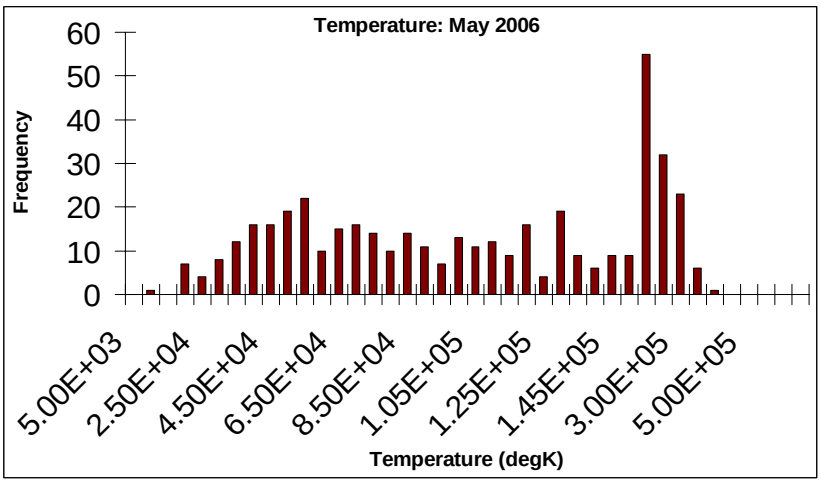

(k)

Figure 76. Figures 33a through 33k exhibit histograms of the ranging temperature values experienced by the solar wind each May over the years 1996 through 2006 (solar cycle 23).

As in the histograms of yearly speeds of the solar wind, the overall change of temperature activity in the solar wind is not evident on such a large scale. However, there are some observations that can be noted from these plots. The most obvious recurring phenomenon is the resurgence of hours experiencing solar wind temperatures of 300000 K and above. Each year exhibits this same β-peak property. This is most likely due to the constant presence of coronal holes, which

allow hot, fast streams to escape the Sun's corona throughout the cycle. It is also relevant that the declining phase (after 2001) has a greater number of hours spent at a higher average temperature. Although most of these histograms share roughly the same shape, the years following the maximum show a larger percentage of hours at the average temperature range, rather than at the low end of the range.

4.3.3. SOLAR WIND DENSITY

Figures 77a through k shows the changes in the solar wind density over the solar cycle from 1996 through 2006. 1996 and 1997 data are from the Wind spacecraft, 1998 through 2006 data are taken from the ACE spacecraft.

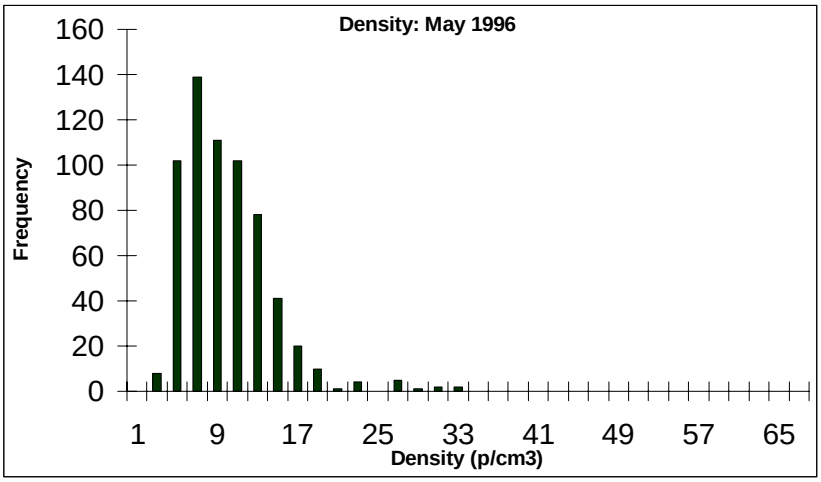

(a)

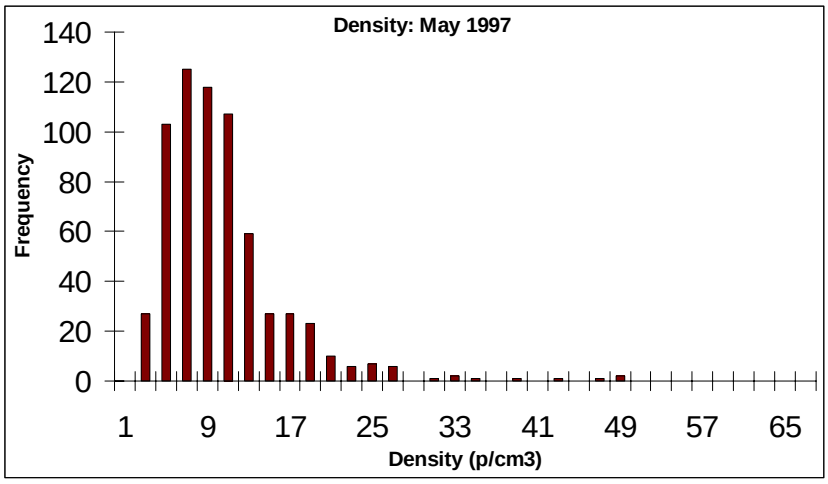
Density: May 1997
Frequency
140
120
100
80
60
40
20
0
1
9
17
25
33
41
49
57
65
Density (p/cm3)

(b)

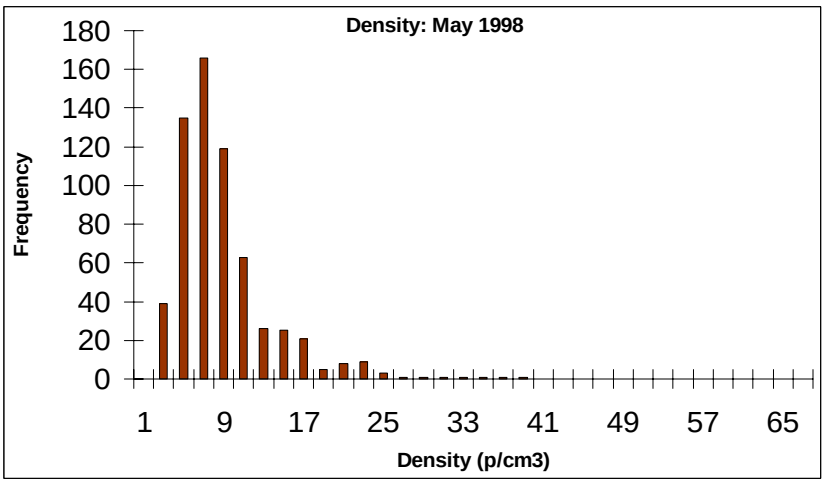
Density: May 1998
Frequency
180
160
140
120
100
80
60
40
20
0
1
9
17
25
33
41
49
57
65
Density (p/cm3)

(c)

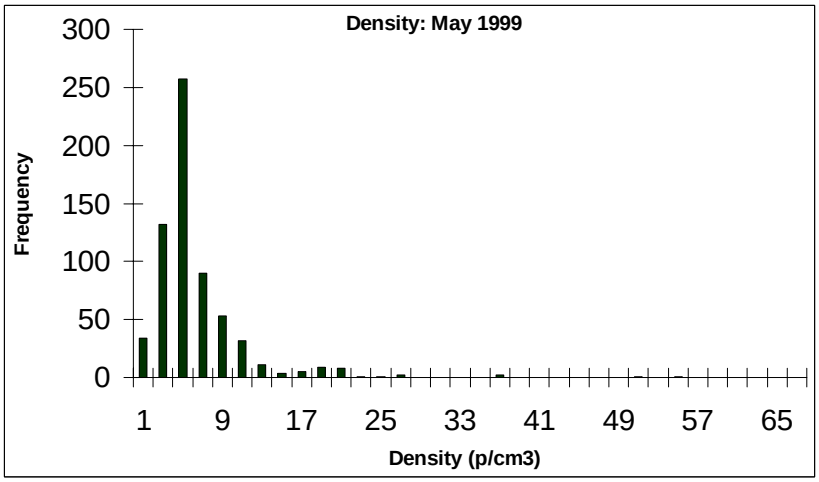
Density: May 1999
Frequency
300
250
200
150
100
50
0
1
9
17
25
33
41
49
57
65
Density (p/cm3)

(d)

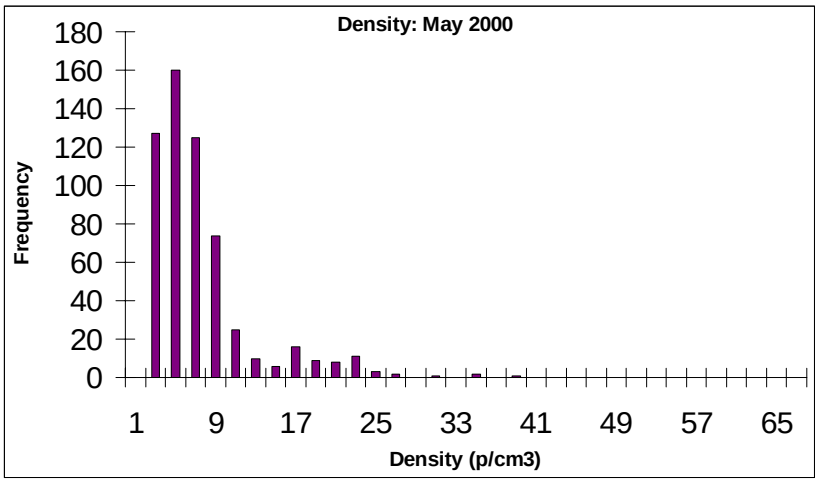
Density: May 2000
Frequency
180
160
140
120
100
80
60
40
20
0
1
9
17
25
33
41
49
57
65
Density (p/cm3)

(e)

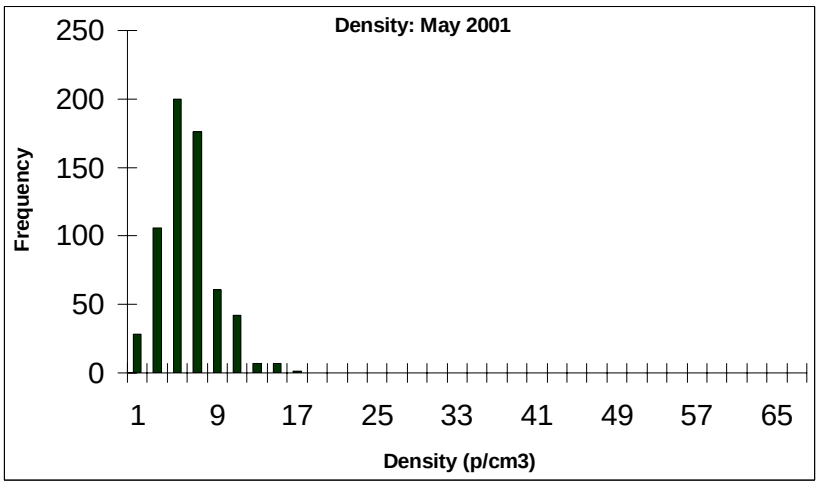
Density: May 2001
Frequency
250
200
150
100
50
0
1
9
17
25
33
41
49
57
65
Density (p/cm3)

(f)

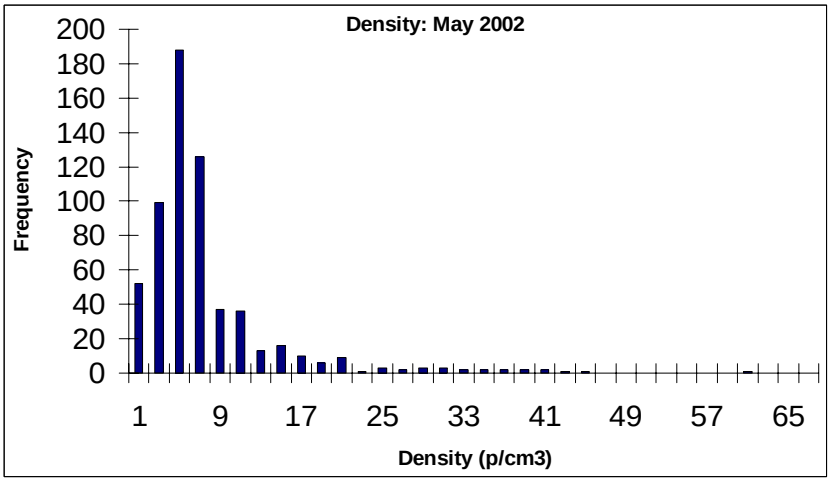
Density: May 2002
Frequency
200
180
160
140
120
100
80
60
40
20
0
1
9
17
25
33
41
49
57
65
Density (p/cm3)

(g)

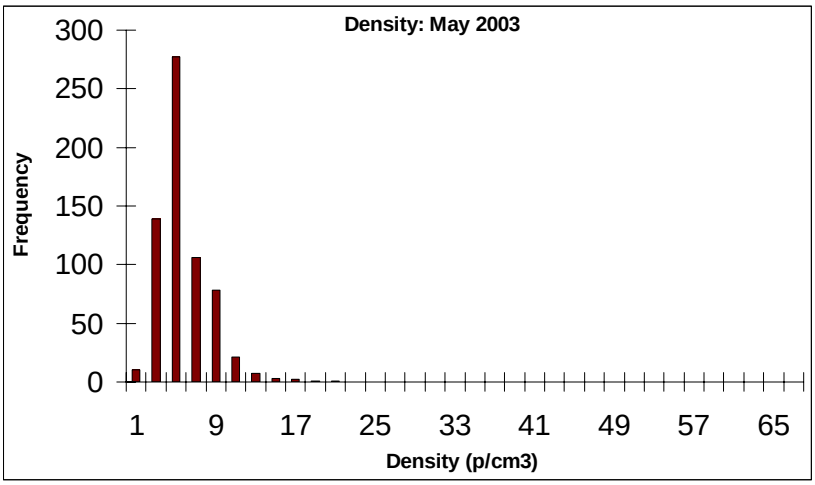
Density: May 2003
Frequency
300
250
200
150
100
50
0
1
9
17
25
33
41
49
57
65
Density (p/cm3)

(h)

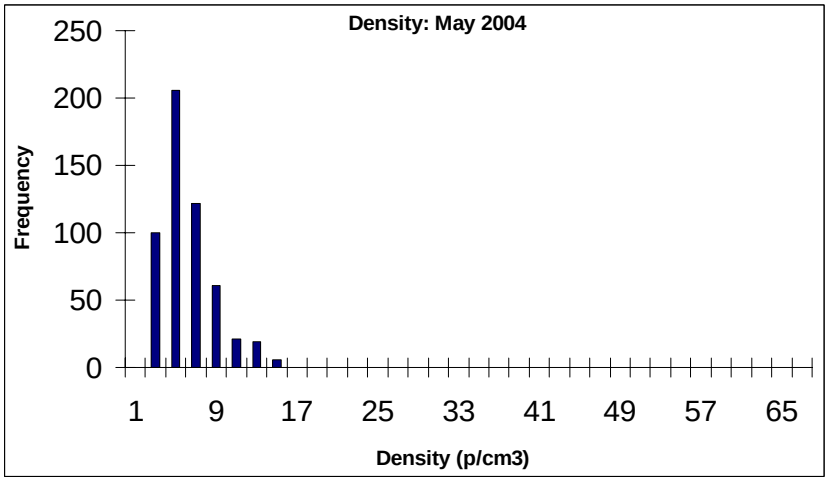
Density: May 2004
Frequency
250
200
150
100
50
0
1
9
17
25
33
41
49
57
65
Density (p/cm3)

(i)

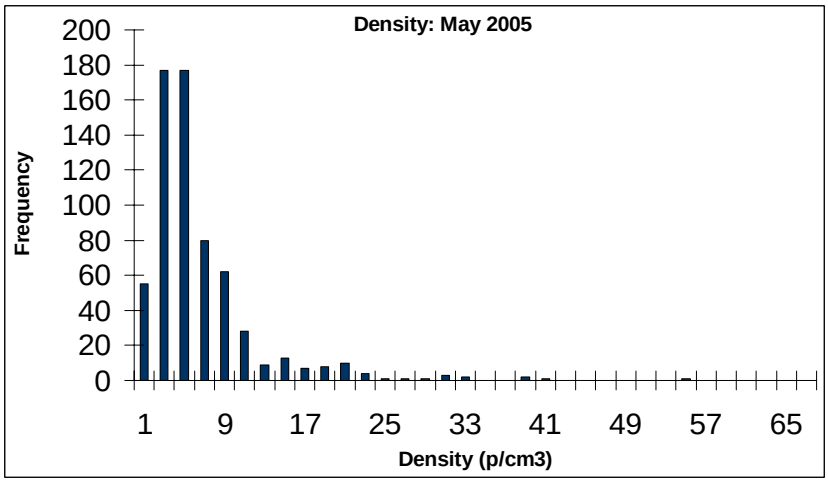
Density: May 2005
Frequency
200
180
160
140
120
100
80
60
40
20
0
1
9
17
25
33
41
49
57
65
Density (p/cm3)

(j)

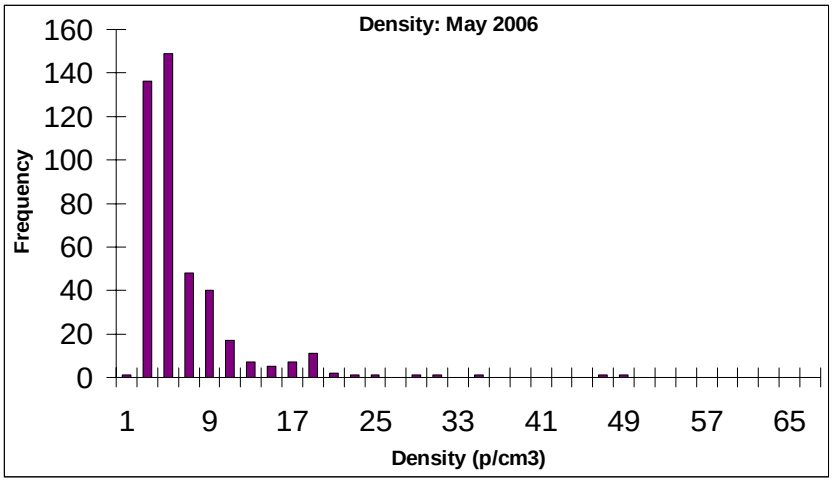

(k)

Figure 77. Histograms 77a through 77k show the varying particle densities exhibited by the solar wind each May throughout solar cycle 23.

The solar wind density histograms exhibit very similar appearances for each year of the solar cycle. Although most densities stay within the 1 - 20 particles per cubic centimeter range, most notably 1996 through 2000, show higher values of the solar wind density. This could be attributed to the lower overall speeds and temperatures during the rising phase of the cycle. These slow, colder streams cause the solar wind to become more dense (whereas hot, fast streams are more tenuous). The faster, hotter streams emitted during the declining phase cause the overall densities during the declining phase (after 2001) to be lower, i.e., the particle density per cubic centimeter is more tenuous.

4.4. SOLAR MAXIMUM VS. SOLAR MINIMUM

Although the changes from year to year may be gradual, there is a large difference in the space environment between the solar minimum years and the

solar maximum years. At solar minimum, the low activity of the Sun causes a smoother version of the solar wind to flow out from the corona, whereas in the solar maximum period, there are often larger solar storms and a greater degree of turbulence in the solar wind. To illustrate the difference in space weather conditions between solar minimum and solar maximum, presented below are data from the sixth Carrington Rotation from the solar minimum year 1996 and the solar maximum year 2001. The sixth Carrington Rotation corresponds roughly to mid-June through mid-July, and therefore represents the middle of each of the years in question. This middle rotation was chosen as it is most likely to be a good representation of the years on the whole.

4.4.1. SPEED

The differences in speeds of the solar wind vary. Depending on the number of active regions and coronal holes during each period, the differences between the solar maximum and minimum speeds can be great or small. In general, however, the solar maximum period shows a greater number of extreme values for solar wind speeds due to the fact that it is prone to more violent storms and particle events.

Figure 78 shows a histogram of the solar wind speeds for the months of June and July (Carrington Rotation number 6) of 1996, approximately half-way through the most recent solar minimum year. Figure 79 shows the same time of

year for the most recent solar maximum in 2001 (further discussion of the solar maximum year is discussed below).

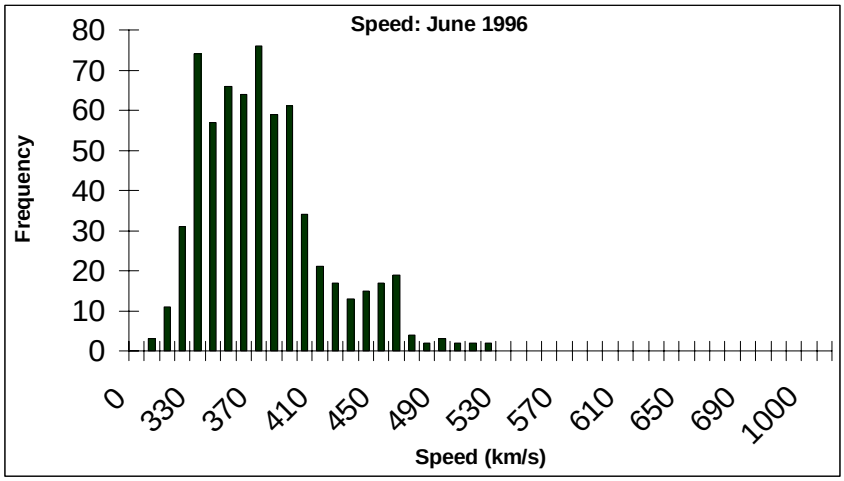

Figure 78. Solar wind speeds for the sixth Carrington Rotation of 1996 (roughly corresponds to June 1996, the middle of the most recent solar minimum)

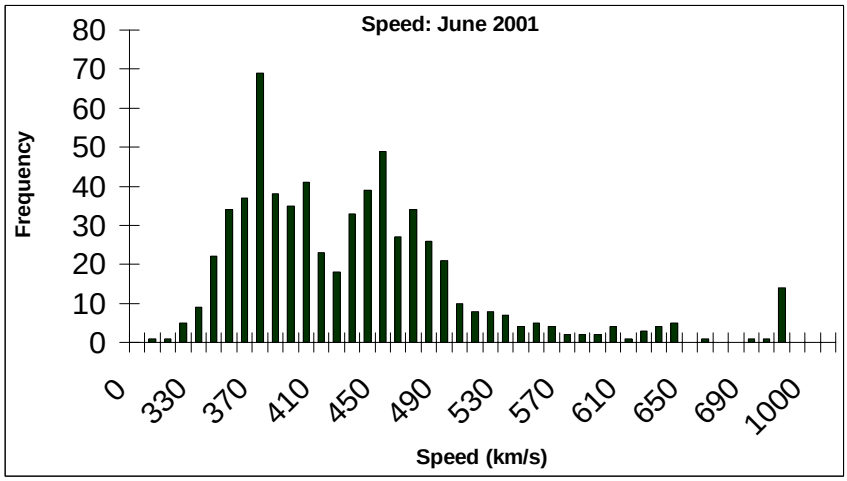

Figure 79. Solar wind speed over the sixth Carrington Rotation of 2001 (corresponding to June of 2001, the middle of the most recent solar maximum)

June of the solar minimum year of 1996, represented in Figure 78, exhibits a single peak, with the most common speeds occurring between 340 and 410 km/s. The entire range of the month falls between 300 and 530 km/s. In the same month during the solar maximum year, there are two peaks, the first of which

occurs between 350 and 420 km/s, and the second of which occurs between 440 and 510 km/s. The values of the solar wind during this period range between 300 and 1000 km/s, and another noticeable peak occurs at this extreme value. An obvious change between the solar minimum and solar maximum is the larger array of values occurring in 2001. Although there is not a high frequency of increased values, there are certainly a higher number of extreme values in 2001 than in 1996, where no solar wind speeds occurred above 530 km/s. This increase in extreme speeds is due to the increased activity of the Sun during solar maximum.

Figure 80 shows a combined histogram of solar wind speeds over the entire solar minimum year of 1996 and solar maximum year of 2001.

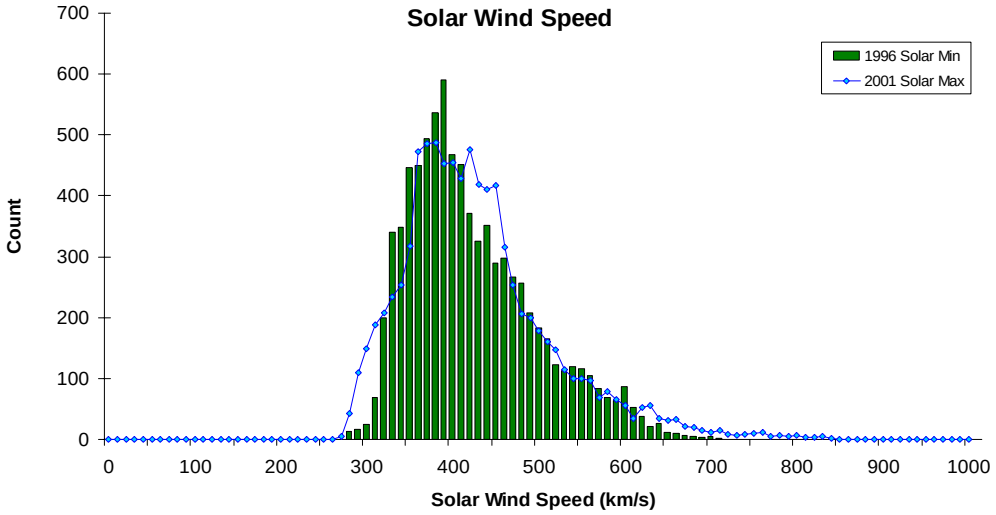

Figure 80. This combined histogram shows the varying values of the solar wind speed of 1996 (minimum) overlaid with the speed values of 2001 (maximum).

As a whole, the speed histograms for the solar minimum of 1996 and solar maximum of 2001 have roughly similar shapes. Certainly, they have similar

peaks around 350 to 450 km/s. However, it is also noticeable here that the extreme values that occurred during the solar maximum did not occur during the solar minimum. However, it is also important to point out that, taking yearly averages, the years do not differ by much. The yearly average speed for 1996 was 419 km/s. The yearly average for 2001 was 423 km/s. This difference is relatively negligible in terms of the range of speeds possible for the solar wind. The difference between speed variances in the solar minimum and maximum lies in the higher occurrence of extreme values in the solar maximum period.

Plots of the solar wind data from the Wind and ACE spacecrafts also show that there are differences between the solar minimum and solar maximum speeds. Figure 81 shows a plot of monthly averages over the year 1996; Figure 82 shows monthly averaged data over the course of 2001. These plots reiterate the fact that the average monthly speeds are also very close during the solar minimum and maximum.

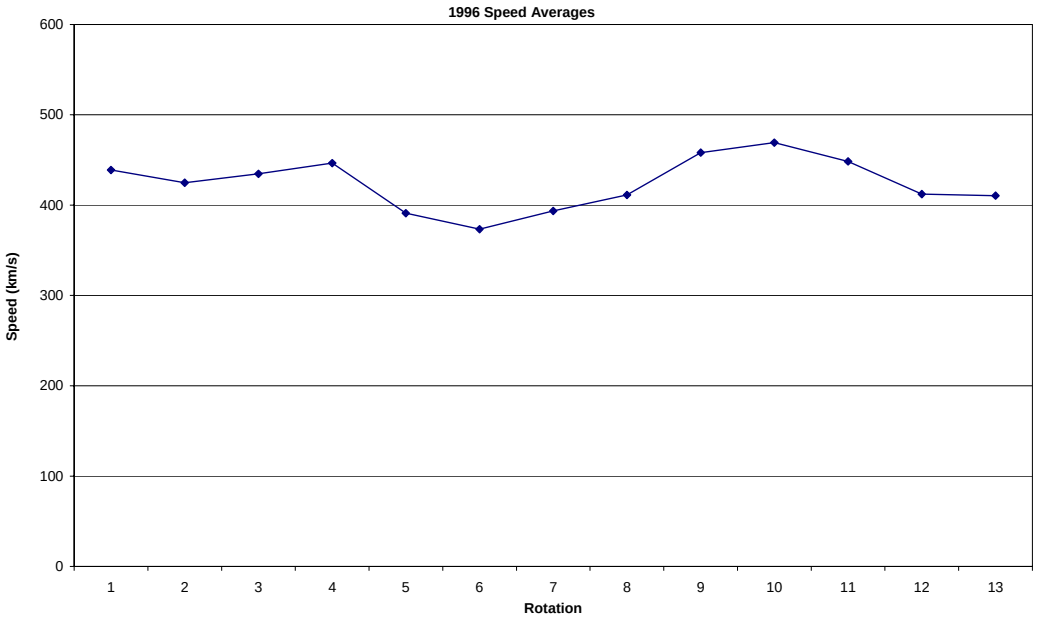

Figure 81. Speed averages of *in-situ* data from the Wind spacecraft for each Carrington Rotation of 1996 (which roughly correspond to the months of the year)

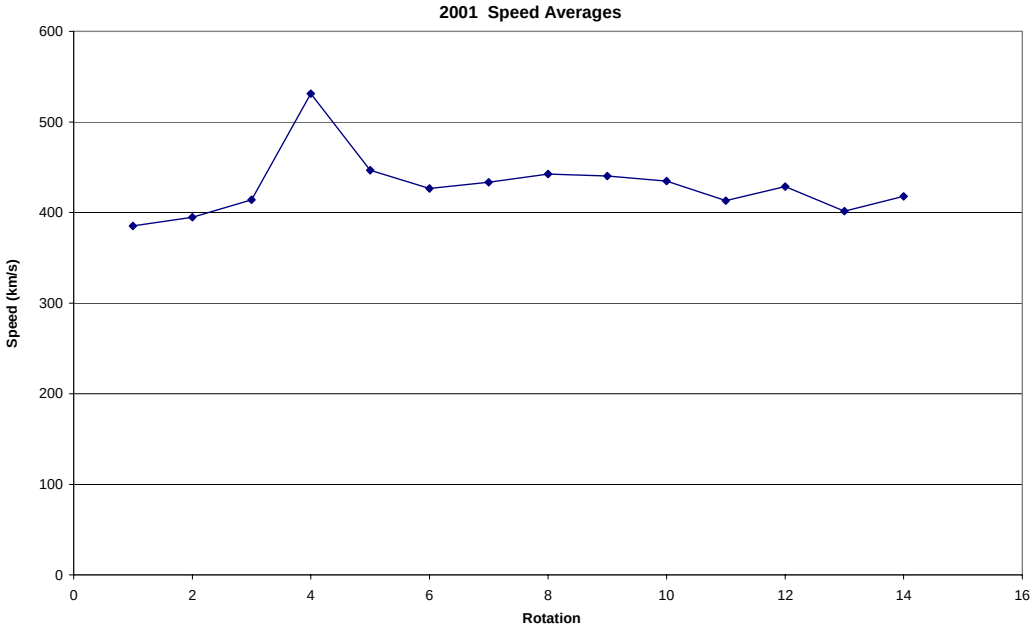

Figure 82. Speed averages for each Carrington Rotation of the year 2001, calculated using *in-situ* data taken from the ACE spacecraft.

Taking the average of solar wind speed per year using hourly data (i.e. data from each hour of each day) and monthly histograms, I find that the average speed during the solar minimum year is approximately 419 km/s. Likewise, during the solar maximum year, the average solar wind speed is approximately 423 km/s. According to this result, there is a negligible difference between the speed of the solar wind in a solar minimum year and a solar maximum year. However, although these values are approximately the same, the solar minimum wind reaches its average by remaining relatively even throughout the year, whereas the wind speed during the solar maximum wanders away from the average greatly with extreme values.

4.4.2. TEMPERATURE

The temperature of the solar wind is contingent on how fast the stream is moving and how dense it is. Due to the interconnectedness of these three parameters, analysis of them is somewhat similar. Cooler streams tend to be slow, whereas hotter streams tend to be fast. Some spacecraft, as in the SOHO mission, measure thermal velocity rather than speed. This measurement makes the most sense in terms of what is actually being measured, but must be translated into speed so that it is an understandable quantity to observers. The thermal speed of the wind is the rate at which the particles are moving. If they are moving faster, then there are more collisions and more friction, and so the stream gets hotter. If the particles are slow-moving, there are less collisions and less friction,

giving the stream a cooler temperature. This gives way to the term "thermal speed". However, since "thermal speeds" of 20 to 50 km/s do not mean much to the average observer, we used the equation

$$temperature = (v_{thermal})^2 \cdot 60.3434 \qquad (4)$$

to convert these thermal speeds into average temperatures in degrees Kelvin.

Figure 83 shows a histogram of solar wind temperatures for the sixth Carrington Rotation of 1996, as shown above for speed. Figure 84 shows the corresponding rotation for solar maximum in 2001.

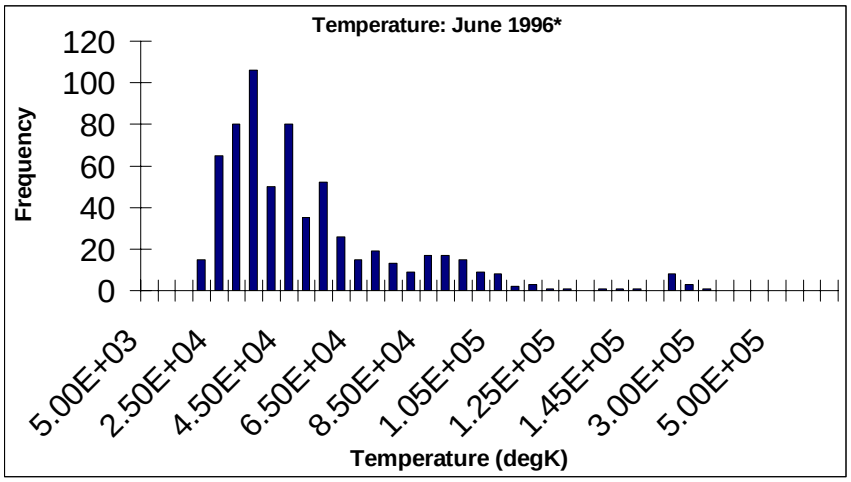

Figure 83. Varying values of solar wind temperatures in June of 1996.

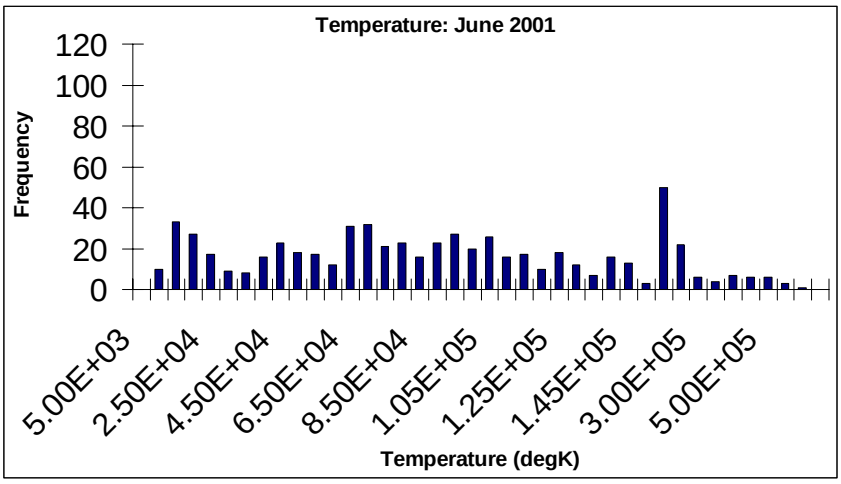

Figure 84. Array of temperatures given off by the solar wind in June of 2001.

In June of 1996, there appears to be a peak where most of the solar wind temperatures fell between $2.5\times10^4\,K$ and $6.5\times10^4\,K$. There are a small amount of days that varied above this peak, but the majority of the time in June of 1996 was spent within this limit. Alternately, in June of 2001, temperature values are actually fairly evenly spread, decreasing slightly at the high end of the values after a large peak near $3.0\times10^5\,K$. Where the solar minimum values above $1.25\times10^5\,K$ are near to none, the solar maximum displays measurements for all possible temperatures. This illustrates again that, although the solar maximum is not always hotter than the solar minimum, it certainly exhibits a higher number of hours spent at extreme values than does the solar minimum.

Figure 85 shows a combined histogram of the solar minimum in 1996 and the solar maximum in 2001 in terms of temperature values for the year.

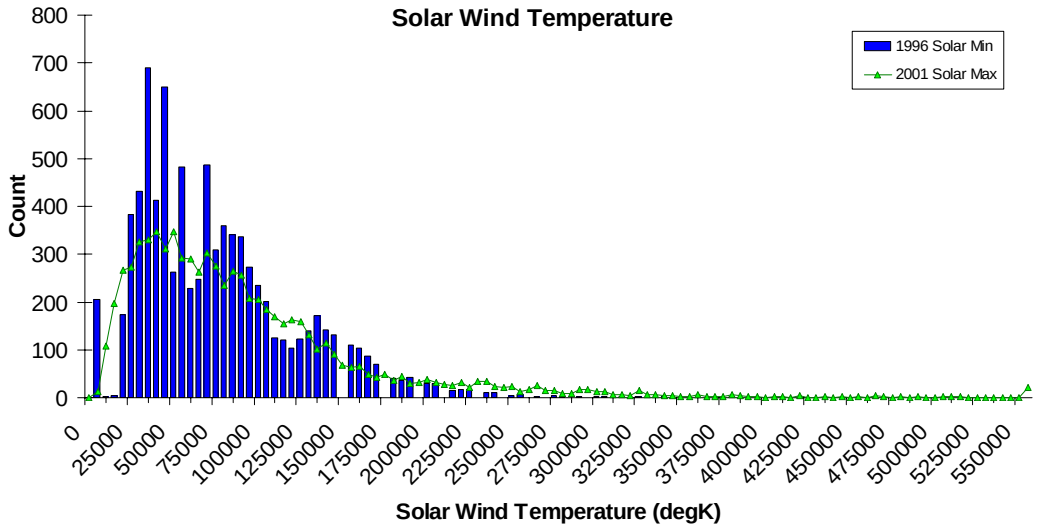

Figure 85. Yearly temperature ranges of the solar wind for 1996 (minimum) and 2001 (maximum).

As shown in Figure 85, the solar minimum spends much more time on the whole at low temperatures than does the solar maximum. Also exhibited in this combined histogram is the fact that, while the temperatures at the solar minimum trail off at about 250,000 degrees Kelvin, the temperatures at solar maximum reached up to over 550,000 degrees Kelvin, an approximately 300,000 degree difference.

This difference between the solar maximum and minimum is also demonstrated in Figures 86 and 87. These figures show the averages from each Carrington Rotation (which roughly correspond to monthly averages) for 1996 and 2001.

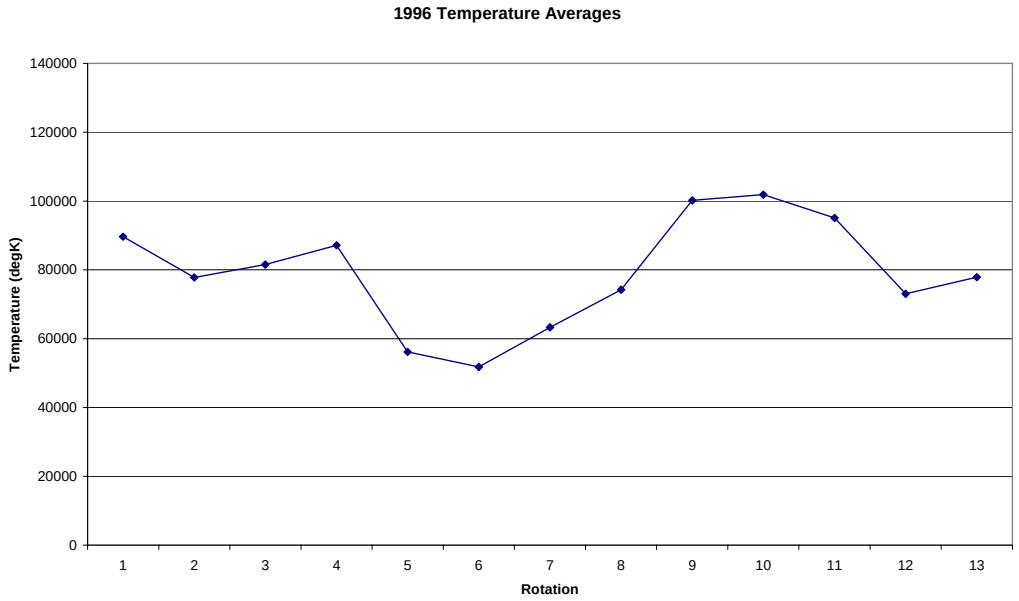

Figure 86. Solar wind temperature averages for each Carrington Rotation of 1996

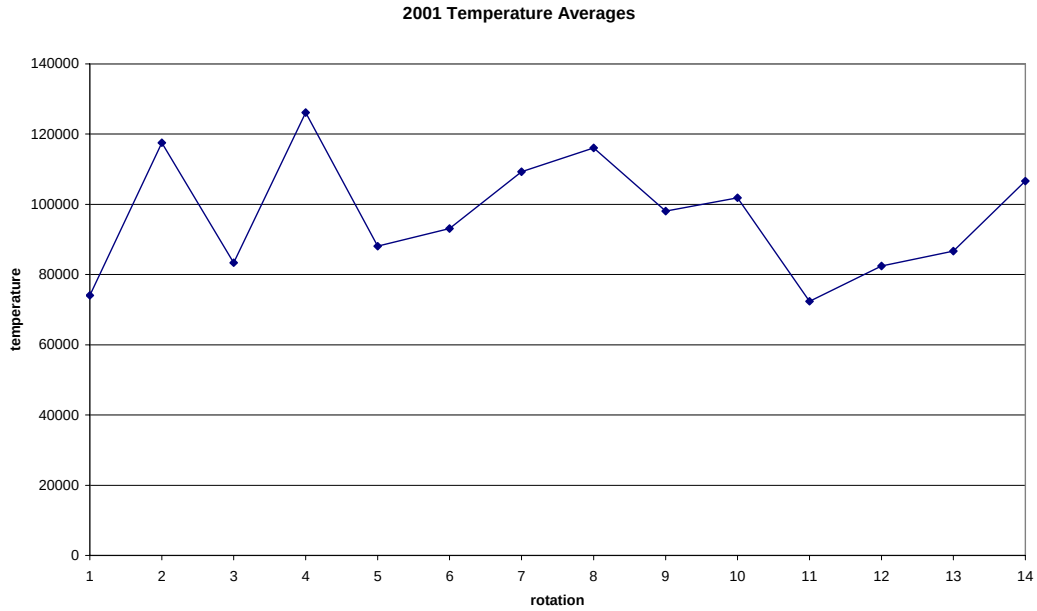

Figure 87. Rotational averages of solar wind temperatures of 2001

In 1996, the rotational averages rarely rose above 100,000 K (only twice). In fact, the maximum rotational average for temperature was 101893.1 K. In

2001, there were many rotations holding averages above 100,000 K (six). The maximum rotational average for 2001 was 126129.5 K, almost 25,000 K more than the highest average temperature reached in 1996. Also observed in this pair of plots is the difference on the low end of temperatures for each year. In 1996, at least seven of the rotational averages dip below 80,000 K; two rotations even had averages below 60,000 K. However, in 2001, only two rotations varied below the 80,000 K mark. These changes in the values of the solar wind temperature during corresponding periods during the maximum and minimum years show the differences that may not be seen on a gradual scale.

4.4.3. DENSITY

Due to the interconnectedness of the solar wind speed, temperature, and density, it comes as no surprise that density data from the ACE and Wind spacecrafts have similar traits to the analyses of speed and temperature. Figure 88 shows a histogram of the sixth Carrington Rotation of 1996, as before with speed and temperature.

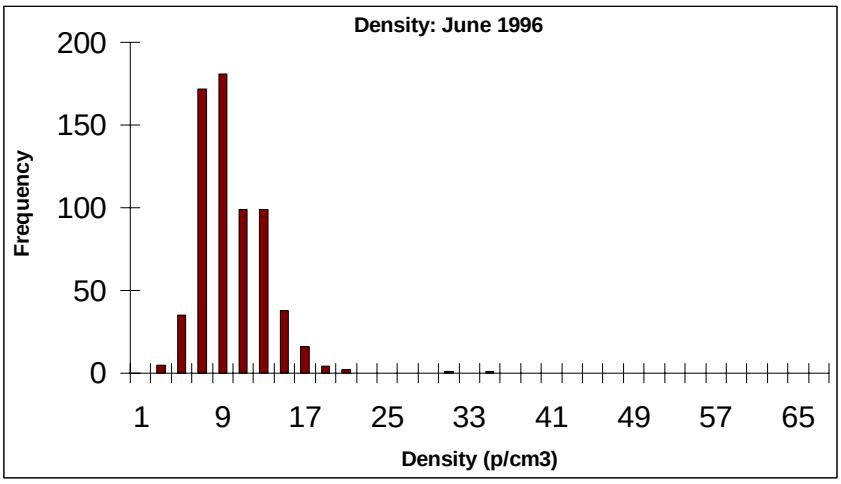

Figure 88. Solar wind densities during the middle of the solar minimum year 1996.

The majority of density values for this middle period of 1996 fall between 5 and 15 particles per cubic centimeter (p/cm^3). For the entire month, the density does not stray above 21 p/cm^3, save for only a few hours on the scale of a month that appear between 31 and 35 p/cm^3. Figure 89 shows a histogram of the corresponding period in 2001.

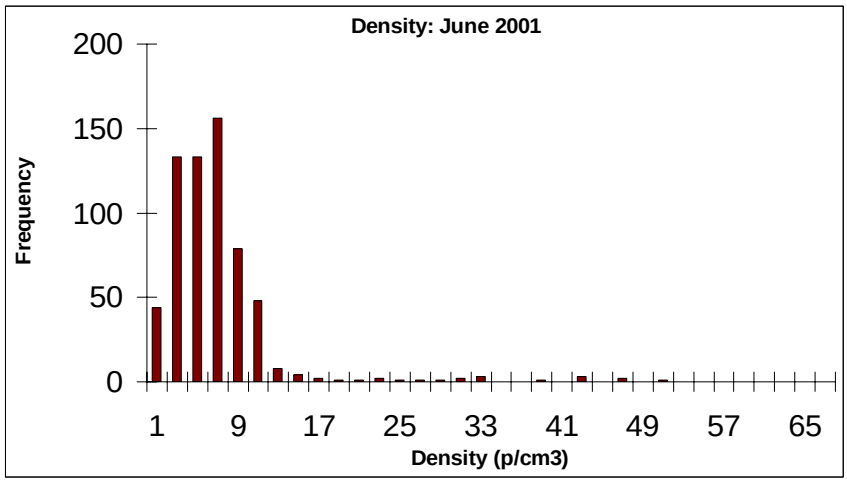

Figure 89. Values of the solar wind density over the middle period of the 2001 solar maximum.

Figure 89 illustrates the extreme values of the solar wind density during the solar maximum. The first thing to note is that the "extreme" values are not only in the high densities, but rather they appear in the lower densities as well. The densities during the solar maximum range all the way down to one p/cm^3 (whereas the least dense streams during 1996 began at 3 p/cm^3), and all the way up to 51 p/cm^3 (whereas the maximum in 1996 occurred at 35 p/cm^3). The extremely low values for the density is due to the increased number of high velocity streams exiting the solar surface at the solar maximum. These high speeds cause the particles to spread and the stream because very tenuous. On the contrary, due to the number of active regions on the Sun during the solar maximum, there are also a lot of slow streams exiting the solar corona. These slow streams are cold and relatively dense, exhibiting densities up to 51 p/cm^3. Figure 90 shows a combined histogram of yearly solar wind densities for 1996 and 2001.

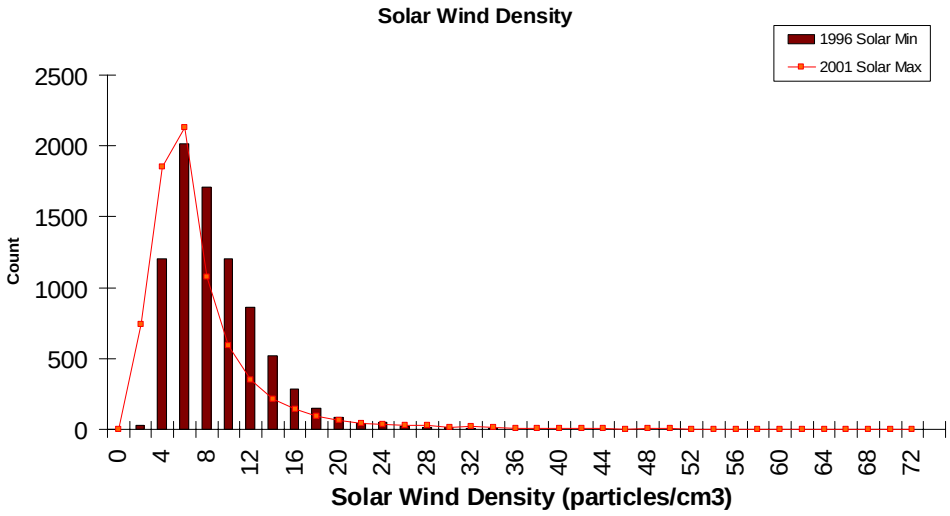

Figure 90. Arrays of values of solar wind density for 1996 (minimum) and 2001 (maximum).

Comparing yearly totals for density, it is again apparent that less-dense streams occur more often during the solar maximum than during the solar minimum. This is exhibited here as the minimum value for density in 2001 reaches into the fraction-of-a-particle per cubic centimeter measurements, where the minimum in 1996 reaches 2. In addition, the maximum values for 1996 trail off at about 36 p/cm^3, the solar wind density values for 2001 range up to 72 p/cm^3, approximately double the maximum value reached in 1996. These differences are related to the positions of active regions and coronal holes on the surface of the Sun. During the solar minimum, coronal holes are at the poles, and there are not many active regions. On the contrary, during the solar maximum, there are many active regions at low latitudes, and the coronal holes have drifted towards the equator, meaning both features are in perfect positions to unleash alternately slow and fast streams (respectively) towards the awaiting spacecraft in the ecliptic. Another way to view the changes in density over the solar maximum and minimum years is by looking at plots of rotational averages (roughly equivalent to monthly averages) for each year. These are exhibited in Figures 91 and 92.

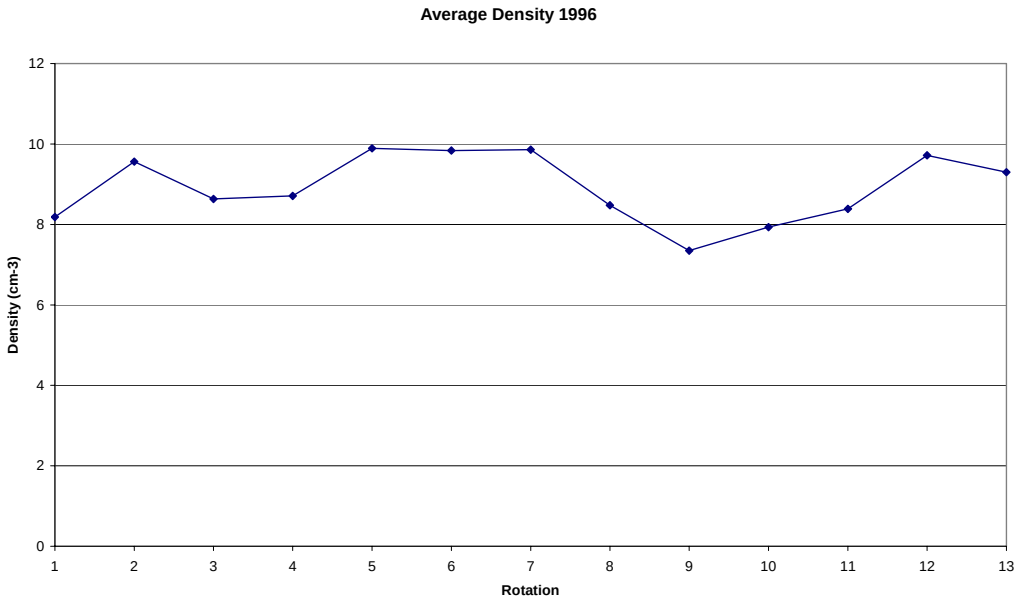

Figure 91. Density averages for each Carrington Rotation in 1996 (minimum).

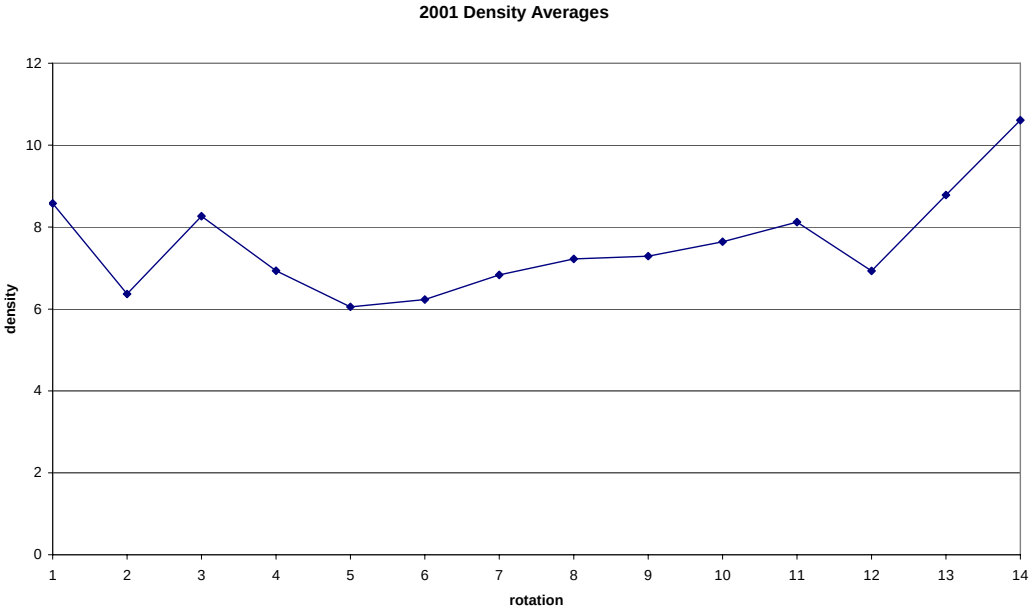

Figure 92. Density averages for each Carrington Rotation of 2001 (maximum).

Figures 91 and 92 illustrate the significant difference between the density of the solar wind between 1996 and 2001. During the solar minimum in 1996, the

rotational average density rarely falls below 8 p/cm^3. Alternately, in the solar maximum, the density spends the majority of its time below 8 p/cm^3. This is again due to the increase amounts of extreme phenomena occurring on the solar surface at solar maximum.

4.4.4. COMPARING PARAMETERS: HOW DO THEY AFFECT ONE ANOTHER?

Another way to investigate the changes of the solar wind parameters during the solar cycle is to directly compare the parameters. The first two figures will show the plots separated so that they can be examined on their own (as they soon become crowded and difficult to read properly), and the third figure shows the combined figure used to see the differences between the minimum and maximum. First, Figure 93 shows a graph of speed plotted against temperature (with a trend line) for the solar minimum in 1996. Temperature here, for ease of reading, is shown in degrees/1000.

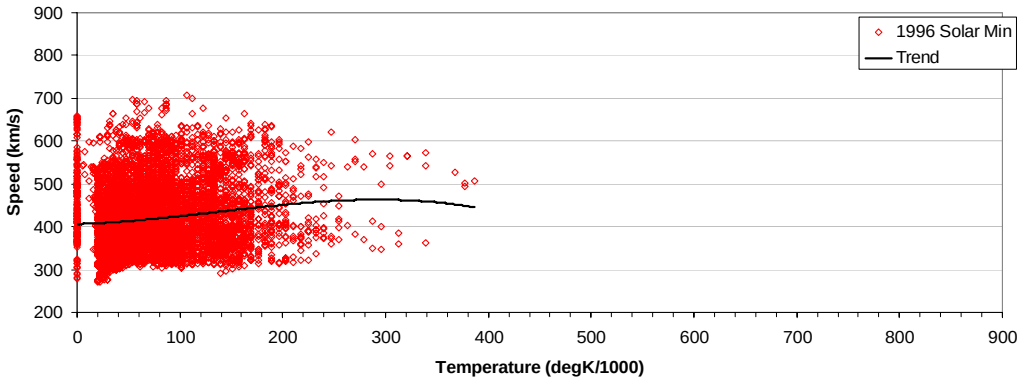

Figure 93. Solar wind speed vs. temperature 1996 (minimum)

Likewise, Figure 94 shows a plot of speed against temperature for the solar maximum in 2001.

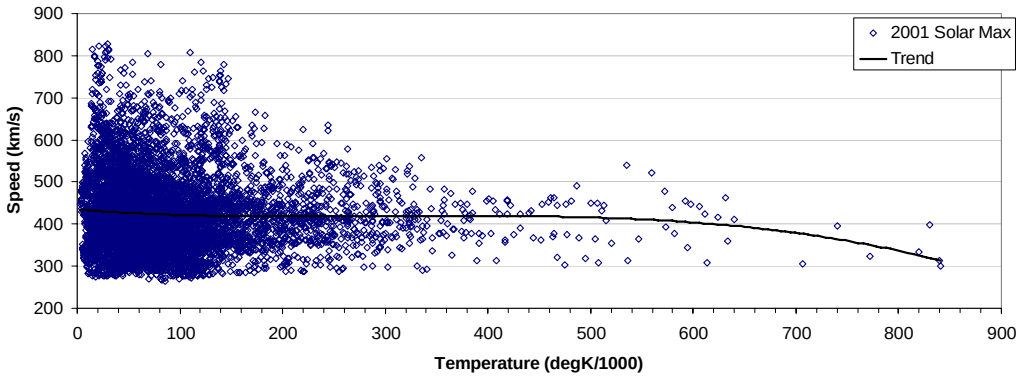

Figure 94. A plot of solar wind speed vs. temperature for 2001 (maximum)

Figure 95 shows a combination of the previous two plots to illustrate the differences between the two.

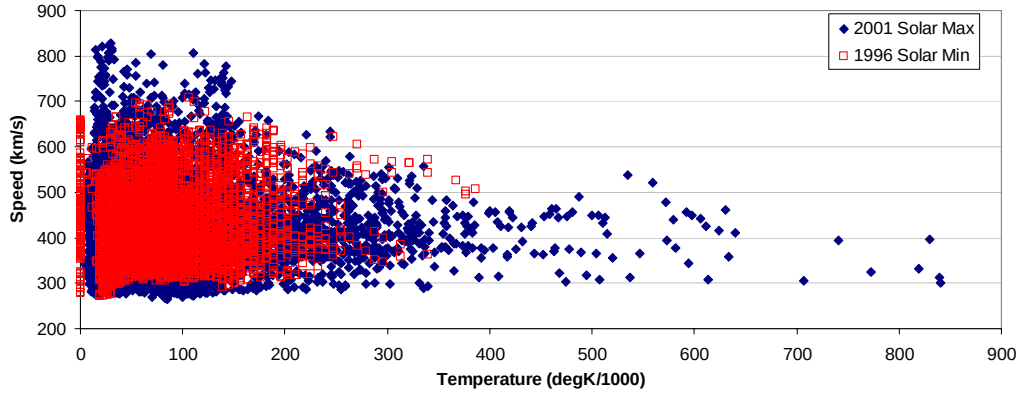

Figure 95. A combination of Figures 93 and 94, showing speed vs. temperature for 1996 and 2001

The first thing to notice about these plots is the extremes to which the 2001 data extends and that the 1996 data does not. Especially using Figure 95, the 2001 data shows a tendency to be either very fast, exhibited by the "column"

of diamond-shaped points at the left of the plot reaching up towards the 900 km/s line, or very hot, exhibited by the extension of the 2001 temperature data out towards the 900 K/1000 mark. The values of the solar wind speeds and temperatures during the solar minimum in 1996 are much more condensed towards a clear average. The values during the solar maximum are much more spread out. These plots also show, using trend lines, that the earlier conviction that speed averages do not vary too much between maximum and minimum is true, due to the fact that both trend lines (in Figures 93 and 94) stay between 400 and 500 km/s for most of the data series. This again shows that although the maximum period exhibits more extreme values, these extremes still average out to be about the same as the relatively smooth minimum period.

Another comparison between parameters is the one between density and speed. Figures 96 and 97 show the plots of density against speed for 1996 and 2001, respectively. Following these two plots, Figure 98 shows the combination of the two in order to compare the results.

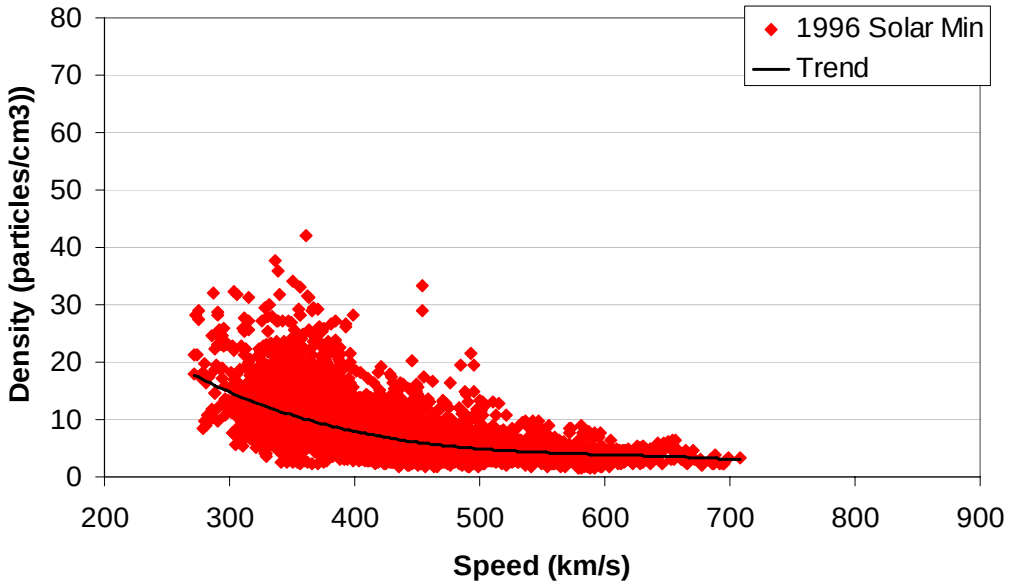

Figure 96. Density vs. speed values for the 1996 solar minimum

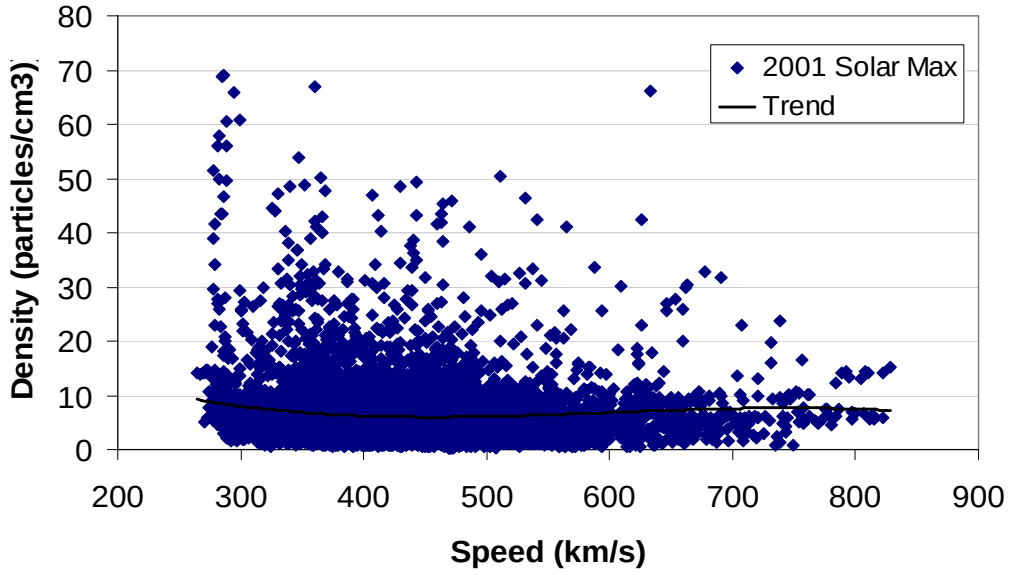

Figure 97. Density vs. speed for the solar maximum 2001

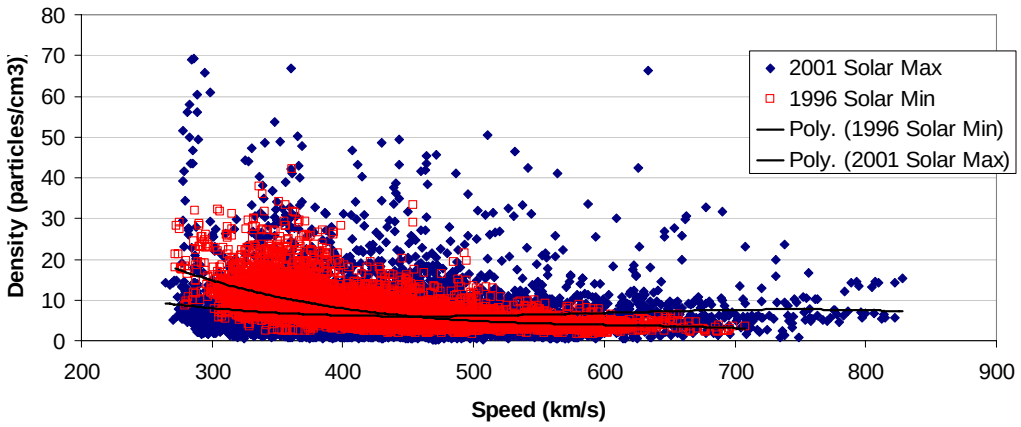

Figure 98. Density vs. speed plot for the 1996 solar minimum and 2001 solar maximum

The combined plot of the density vs. speed values for 1996 and 2001 shows an increase in the extreme values of density across the range of speeds, although most of the highest densities seem to occur at lower speeds. The lower speed streams move at a rate such that the particles within it are crowded together, causing the higher density seen in Figure 98 over the lower speeds. It is also evident again that the solar maximum period exhibits a wider range of all values than the minimum, as it (in diamond-shaped points) shows a wider spread than the relatively condensed form of the data from the 1996 minimum.

Density vs. temperature plots exhibit similar extreme behavior by the solar wind during the maximum. Figures 99 and 100 show plots of the individual years, whereas Figure 58 shows a combination of the plots for comparison purposes.

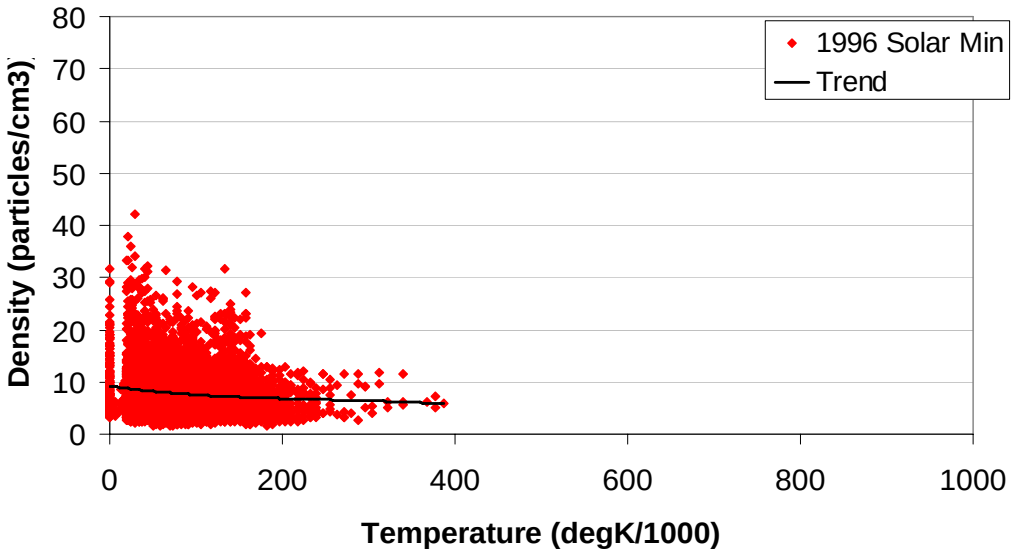

Figure 99. Density vs. temperature for the 1996 solar minimum

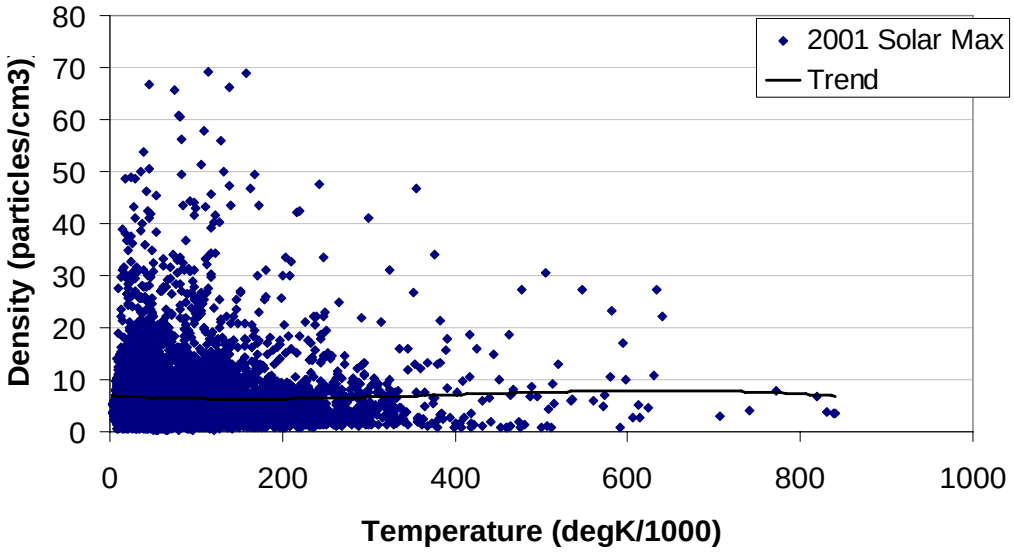

Figure 100. Density vs. temperature for the 2001 solar maximum

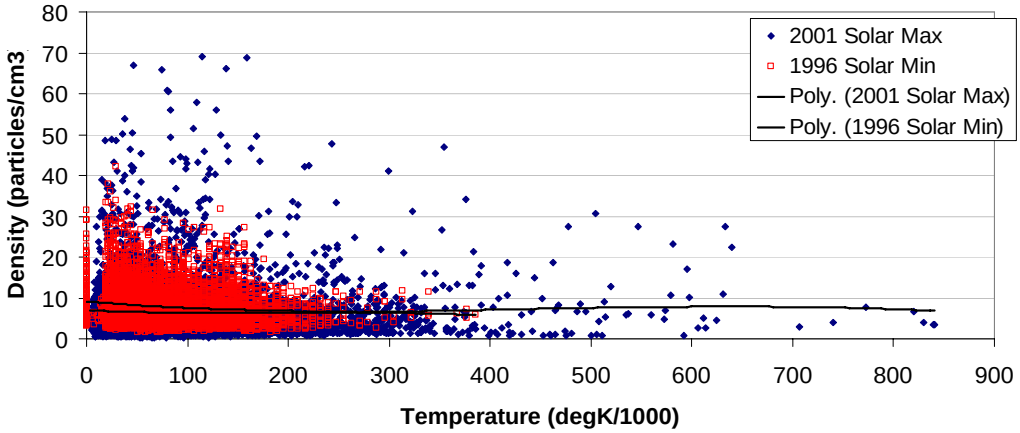

Figure 101. A combined plot of the density vs. temperature values for the minimum and maximum

Figure 101 shows the large difference between extreme occurrences during the maximum and minimum periods. Where the values reach all the way up to 70 p/cm^3 on the density axis and up to about 850,000 K on the temperature axis, the values during the minimum reach to about 40 p/cm^3 at maximum density and to about 400,000 K at maximum temperature. This is a change of 30 p/cm^3 in density and 450,000 K in temperature between the solar maximum and minimum periods.

4.4.5. FINDING THE SOLAR MAXIMUM

Although most of the comparisons between the solar maximum and solar minimum refer to the years 2001 and 1996, the previous solar maximum was actually a double-peak between 2000 and 2001. This can be observed in Figure 3. However, to illustrate that there was little difference between the years, presented here are plots of the solar wind averages for 2000 and 2001 for comparison.

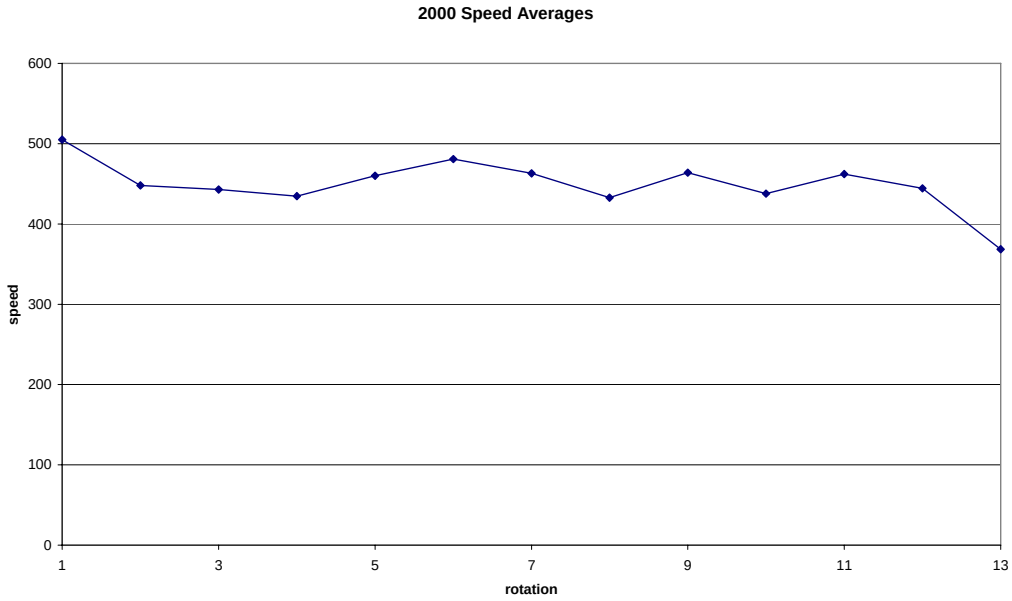

Figure 102. Rotational speed averages for the year 2000

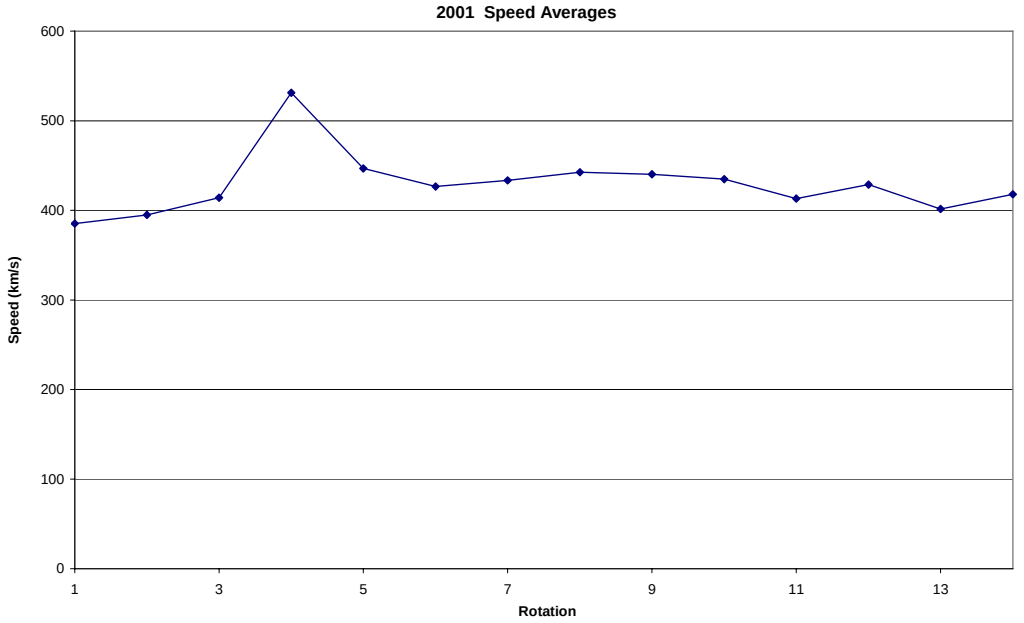

Figure 103. Rotational speed averages for the year 2001

Figures 102 and 103 show that the average speeds in each rotation of 2000 and 2001, respectively, did not vary much outside of the 400 to 500 km/s range.

2001 exhibits slightly more activity in terms of straying from the average than does 2000. Figure 104 shows a combined histogram (in area plot form) to illustrate the differences between the two years.

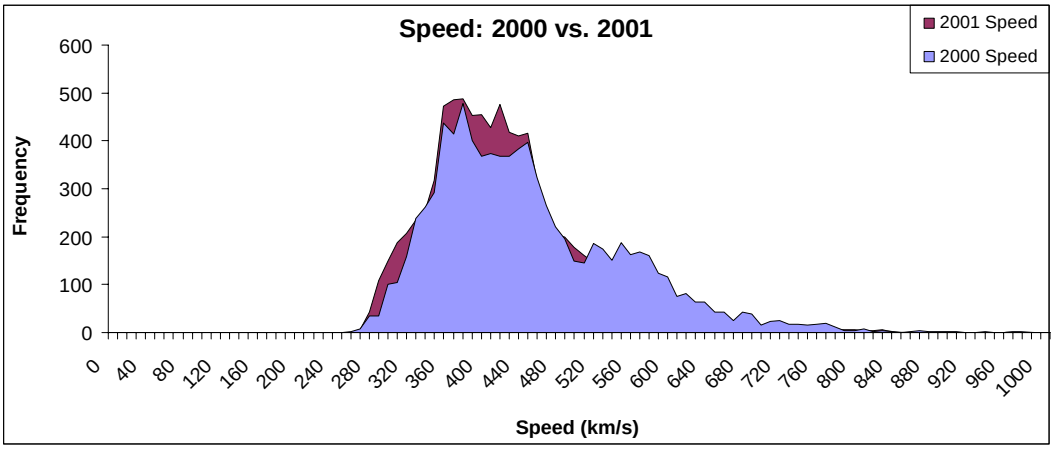

Figure 104. A combined histogram in area-plot form showing similarities between the 2000 and 2001 values for speed

Figure 104 shows that there are only a few differences between the hourly values for all of 2000 and those for all of 2001. The year 2000 shows more hours total at the peak of the curve, but the year 2001 shows a slightly increase number of hours at higher extremes than does 2000.

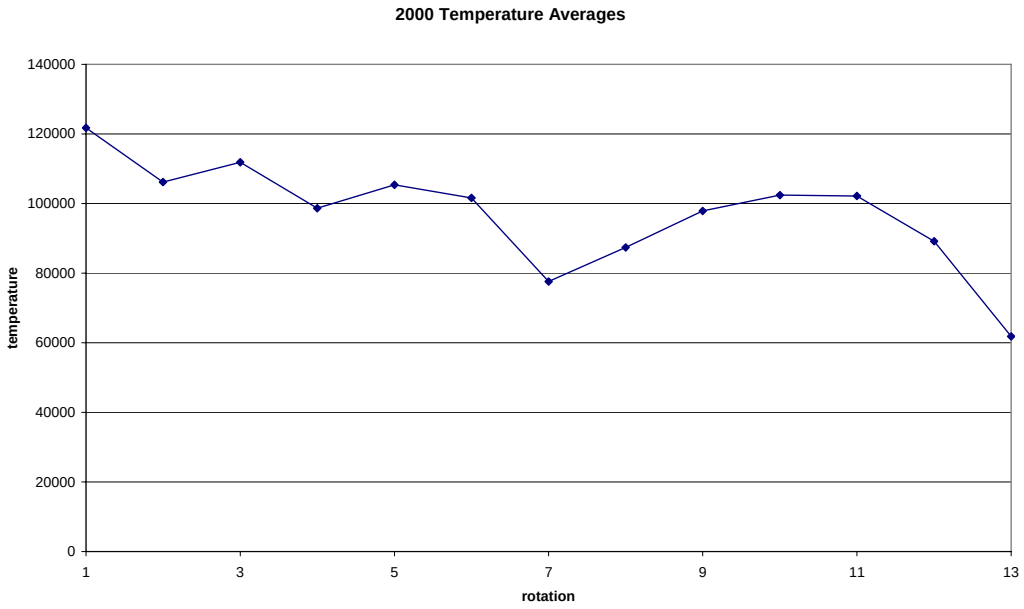

Figure 105. Temperature averages over each rotation of 2000

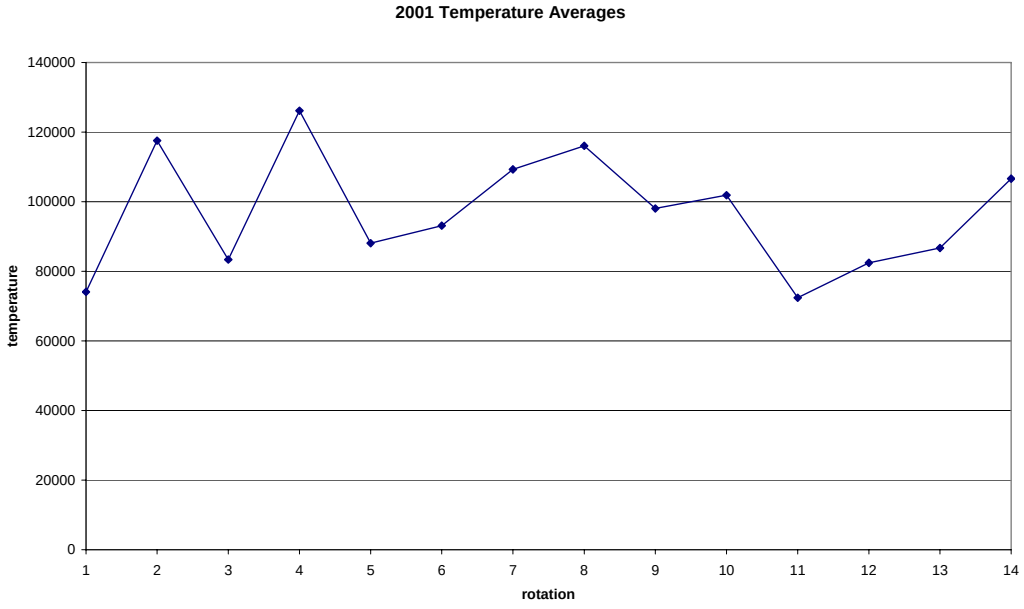

Figure 106. Temperature averages for each Carrington rotation of 2001

Figures 105 and 106 show similar plots for the rotationally averaged temperatures of the solar wind in 2000 and 2001, respectively. Although the plots

appear different, the averages in both plots stay mostly between 80,000 and 120,000 km/s. Again, the 2001 plot appears to show a bit more activity than the 2000 plot. Figure 107 shows a combined histogram in area-plot form to show the similarities between the two years' hourly data.

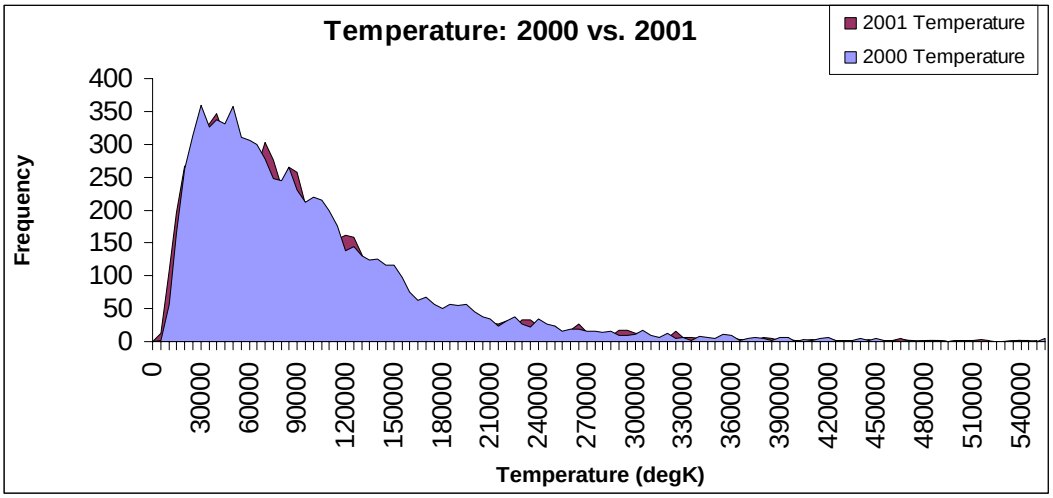

Figure 107. A combined histogram in area-plot form that shows the similar values reached during the 2000 and 2001 double peak maximum

As shown in Figure 107, there are very few differences between the histograms of hourly averages in 2000 and 2001. Both years extend (at low levels) to approximately 540,000 K, but spent most of their time between 25,000 and 150,000 K.

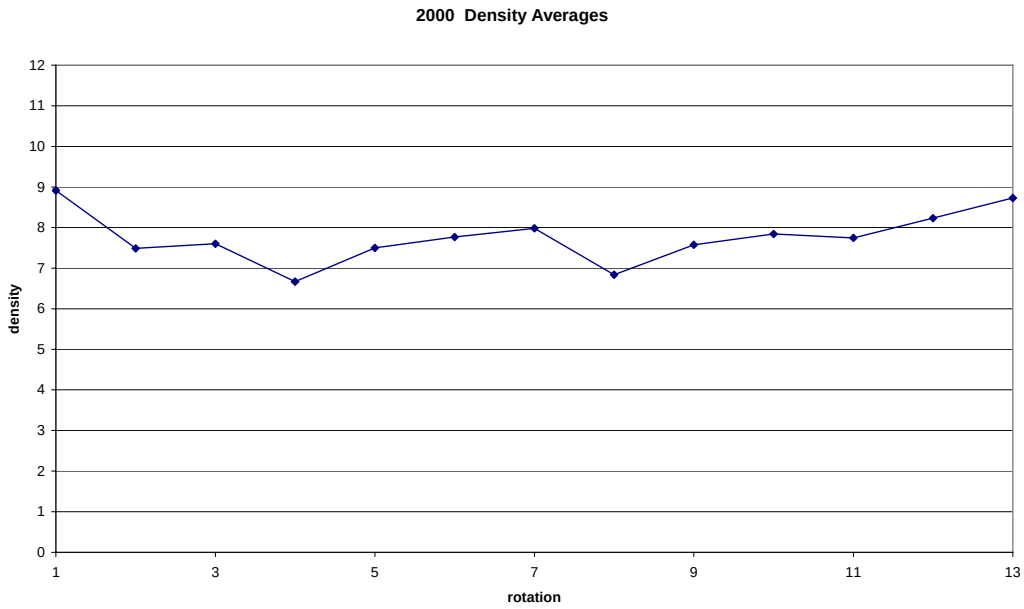

Figure 108. Solar wind particle density averages for each rotation of 2000

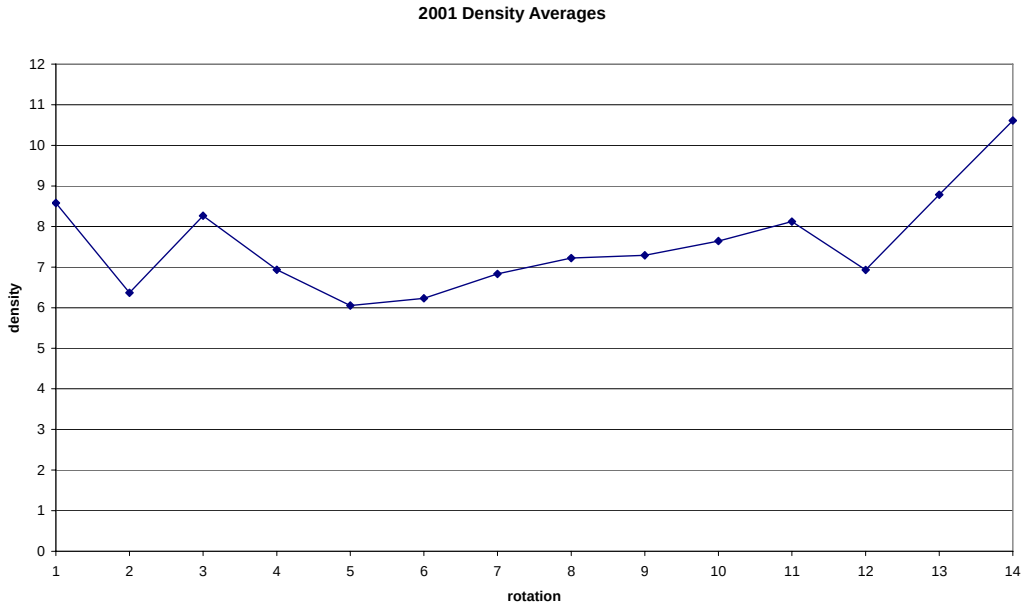

Figure 109. Solar wind density averages for each rotation of 2001

Figures 108 and 109 show similar results from the analysis of the particle densities for 2000 and 2001, with the majority of the density averages in both plots remaining between six and nine p/cm^3. Again, there is a variance in the 2001 plot that suggests further activity than in 2000. In Figure 110, a combined area plot of the density histograms for 2000 and 2001 show that the density values reached in 2000 and 2001 are almost exactly the same. The only real difference is the slightly larger amount of time spent at the two to five p/cm^3 range during 2000 than in 2001.

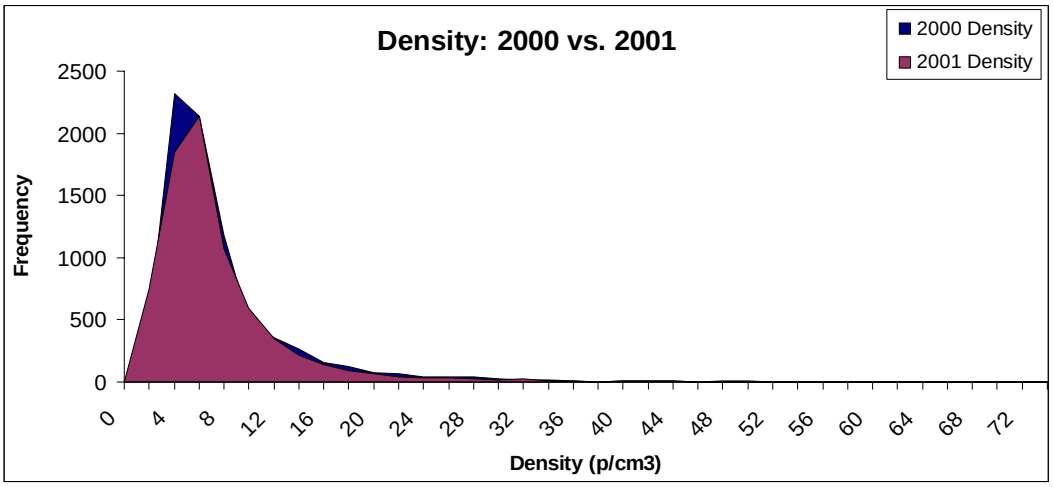

Figure 110. An area plot to compare histograms of density values from 2000 and 2001.

After analyzing these plots and histograms, it was determined that the decision to use the year 2001 as the official solar maximum for this thesis was appropriate, as there were very few differences between the two peak years, and that in fact, the year 2001 showed slightly increased amounts of activity.

4.4.6. THE SUNSPOT CONNECTION

How exactly are the solar minimum and maximum tied to the sunspot cycle? To answer this, we compare plots of sunspot number against the various solar wind parameters measured by the spacecraft. Since NOAA only keeps track of monthly sunspot numbers, i.e. the total number of sunspots per month, we use the rotational averages to plot against these numbers, as there are as many rotations in one year as there are months.

First, in Figure 111, there is a plot of sunspot number against speed in the minimum year 1996 superimposed on the same plot for the maximum year in 2001.

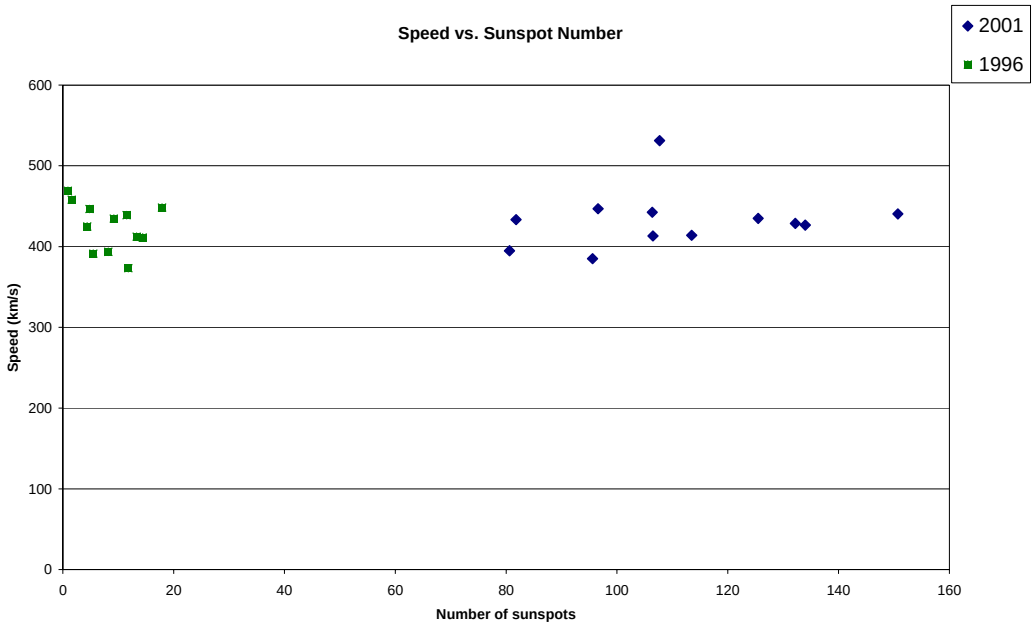

Figure 111. Speed vs. sunspot number for 1996 averages and 2001 averages

In this graph, the solar minimum in 1996 shows values that were more condensed than the spread of values seen in the solar maximum. The values

during the solar maximum are spread out more in both the vertical and horizontal directions. Hence, not only is the extreme behavior of the solar wind during solar maximum shown here, but also the difference between the solar minimum and maximum in terms of sunspot numbers. The solar minimum sunspot number varies between 1 and 20 sunspots per month in 1996, whereas the sunspot number in 2001 varies between 80 and 150 sunspots per month.

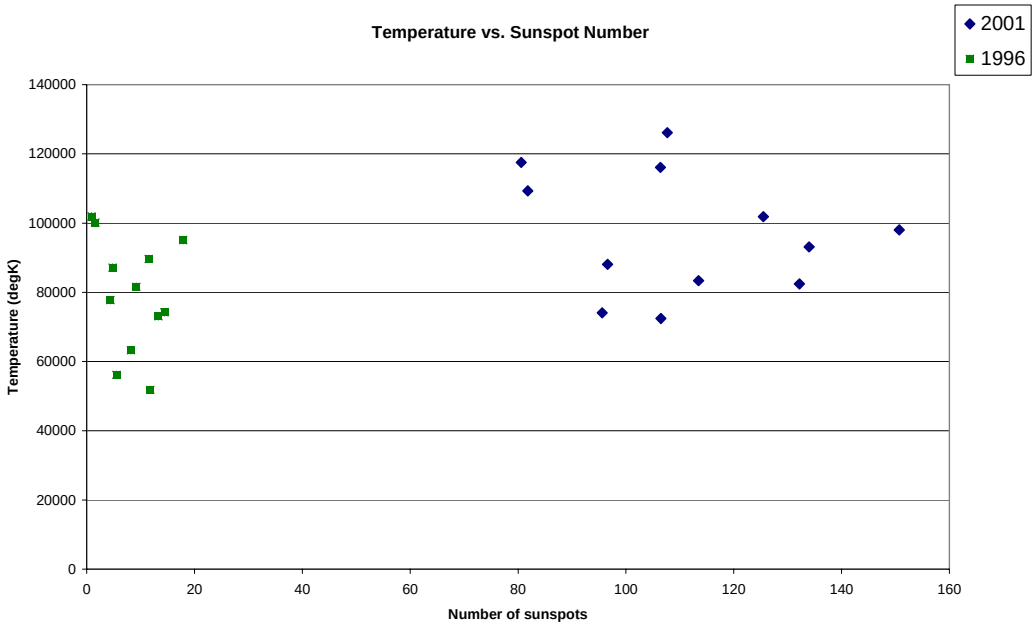

Figure 112. Monthly temperature averages plotted against monthly sunspot numbers for 1996 and 2001

Figure 112, which shows rotational averages of temperature plotted against the monthly sunspot numbers for 1996 and 2001, also exhibits the tendency of the solar maximum to have a larger spread of values for temperature than the solar minimum. The vertical range in average temperatures during the

solar minimum period is approximately 50,000 K, whereas the vertical range in average temperatures in 2001 is approximately 60,000 K.

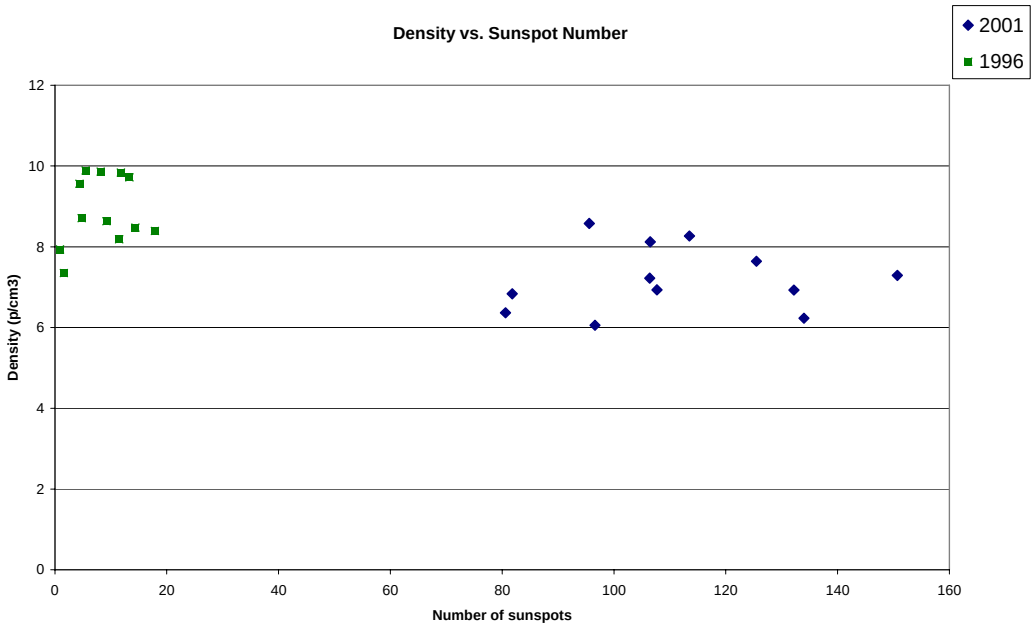

Figure 113. Rotationally averaged density measurements plotted against the monthly sunspot numbers of 1996 and 2001

Figure 113 shows the combined plot of particle density against sunspot number from the years 1996 and 2001. The solar minimum, with its usual condensed values compared with the maximum data, actually exhibits overall higher density than the solar maximum. It ranges between seven and ten p/cm^3, whereas the solar maximum density averages range between six and nine p/cm^3. This is due to the relative number of slow, cold streams exiting the Sun at minimum; there are a lot more of the hotter, fast, tenuous streams leaving the Sun during the solar maximum, causing the observed vertical difference in density averages between 1996 and 2001.

4.5. THE COMPLETE SOLAR CYCLE

Although the STEREO spacecraft is scheduled for a two-year mission and will therefore only experience the solar minimum and rising phase of the solar cycle, it is possible that the mission will be extended and so it is important to study the entire cycle. Plotting the solar wind speeds, temperatures, and densities over the whole cycle gives the results seen in Figure 114.

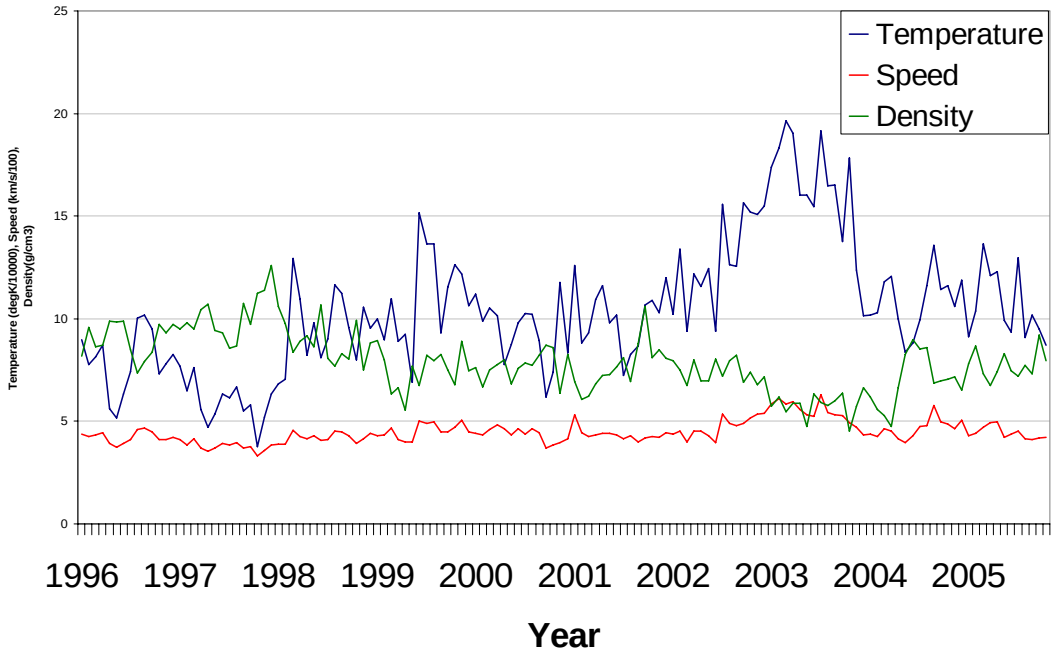

Figure 114. A combined plot of monthly temperature (in K/10000), speed (in km/s/100), and density (in p/cm^3) averages over the complete solar cycle 23 (1996 – 2006)

Figure 114 shows plots of the monthly averages of the solar wind speed, temperature, and density from 1996 to 2006, covering the whole of solar cycle 23. Looking at this plot qualitatively, it can be observed that the density of the solar wind most often acts in the opposite way than the speed and temperature. For

instance, when temperature and speed decrease slightly in the years 1997 and 1998, the density average increases. The same behavior is observed in 2003, as the speed and temperature averages increase and the density decreases, and with good reason. Any time there is a cold, slower stream, the particle density increases; when the stream is hot and fast, the particle density decreases. In fact, it is observed in Figure 114 that the maximal temperatures and speeds of the solar wind occur during the declining phase, and that the maximal densities occur in the rising phase of the cycle. This observation is consistent with that of a recent study by Veselovsky et al.[xli]

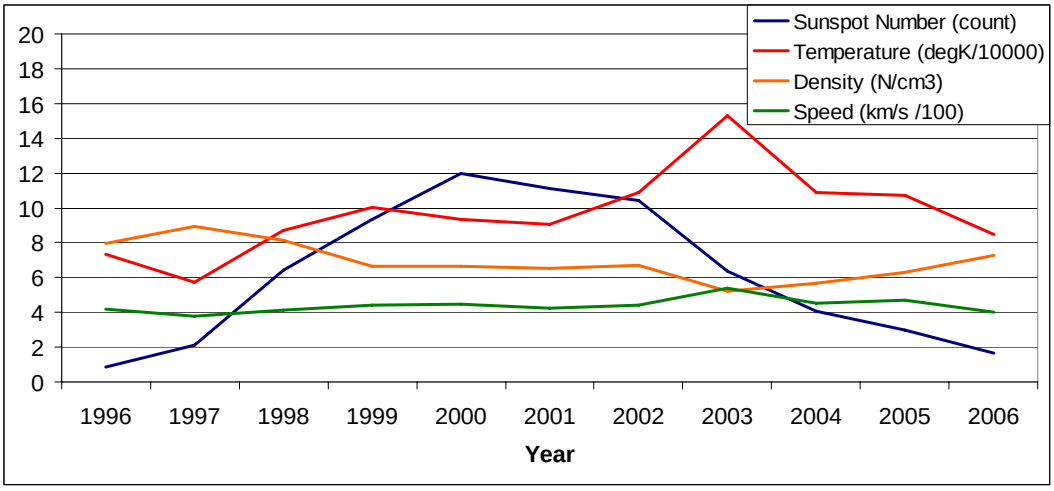

Figure 115. A combined plot of the yearly averages of speed, temperature, and density in addition to the sunspot number for that year

Figure 115 shows a combined plot of speed, temperature, density, and sunspot number over the whole of solar cycle 23. Unlike Figure 114, this figure plots yearly averages, so that big-picture trends can be observed. As noted above, the density also shows an inverse relationship to the temperature and speed here.

The added data of sunspot number in this plot shows the direct correlation of these parameters to the cycle. In this yearly average plot, it is again evident that the highest densities are observed during the rising phase, and conversely, the lowest temperatures and speeds are measured during this period. Alternately, the highest speed and temperatures and lowest densities are observed during the declining phase. To convert the values of temperature, speed, density, and sunspot number to a common scale, temperature is measured here in K/10000, and speed is measured in km/s/100.

To see the overall picture of the solar wind over a solar cycle, Figures 116 through 118 were created to plot histograms of the rotational averages of each year of solar cycle 23. These averages, plotted together as an eleven-year, 143-rotation histogram, show the normal variation of the overall cycle. Using this spread of values, we can then compare individual months to the overall picture of the cycle and find extremes.

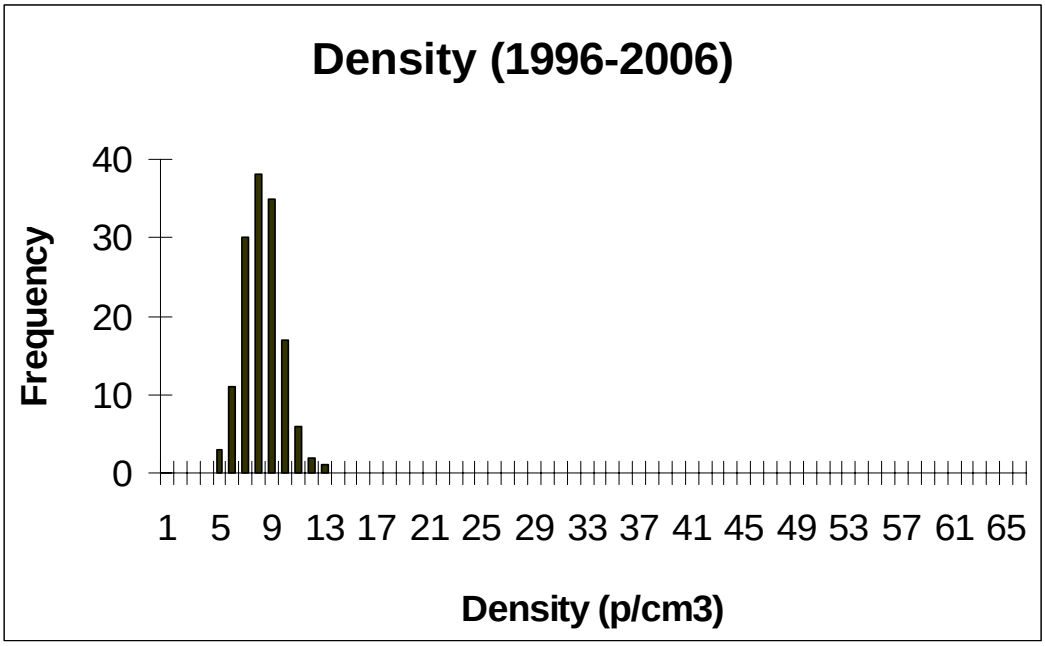

Figure 116. A histogram of 143 rotational density averages (each rotation from January 1996 to 2006)

Figure 116 shows a histogram of the rotational averages for 1996-2006 of the varying density values reached. As shown, the majority of the time during the cycle is spent between six and 9 p/cm^3 particle density. In fact, the average density over the entire cycle never reaches below four p/cm^3 or above 13 p/cm^3, although we do find many individual events during the cycle that surpass these limits.

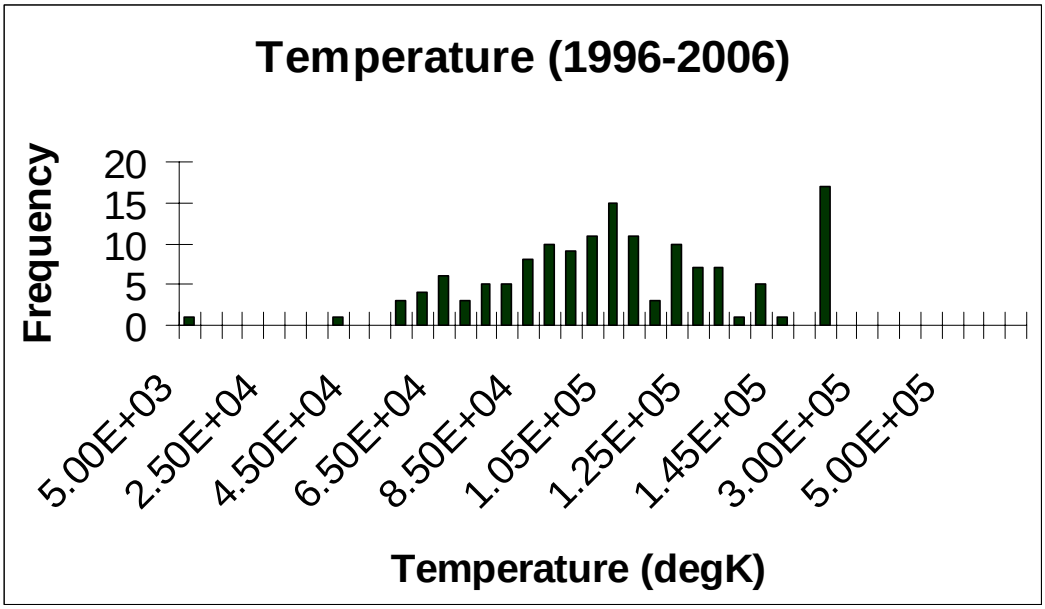

Figure 117. A histogram of rotational temperature averages for all of solar cycle 23

Figure 117 shows a similar histogram, this time with rotational temperature averages plotted. As shown, the majority of the average temperatures occur above 85000 K, and there is a β-peak at 200,000 K. In fact, only a small fraction of the average temperatures occur below 55000 K, and none occur above 200,000 K. Similarly to the density histogram, however, many extremes outside of these limits are measured during individual events.

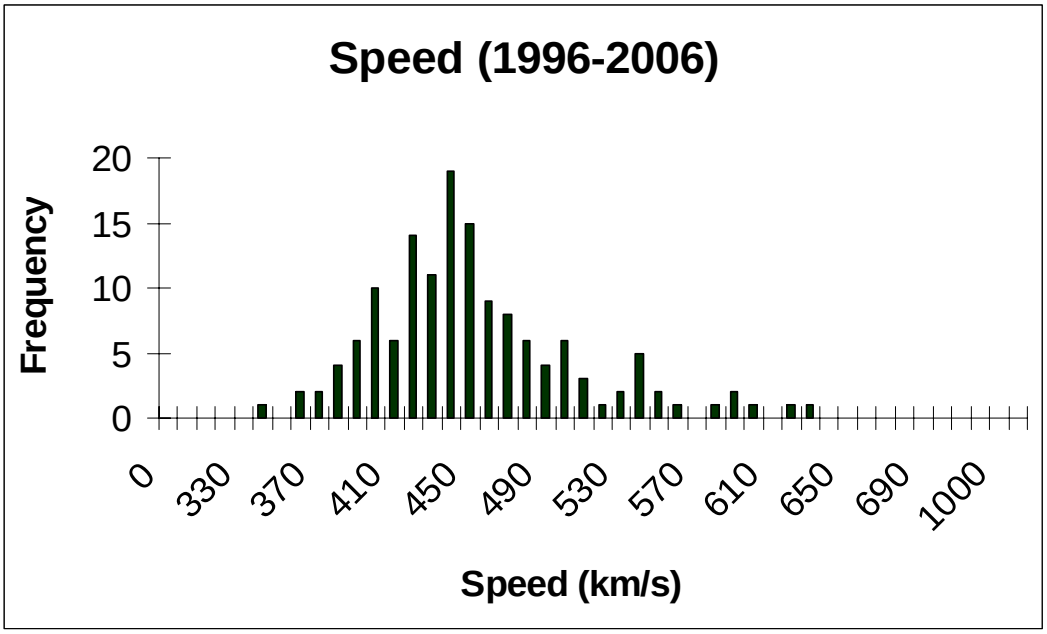

Figure 118. A histogram of solar wind speed rotational averages between 1996 and 2006

Figure 118 shows the corresponding histogram of rotational speed averages. Again, the majority of averages fall between 410 and 480 km/s, with a β-peak representing fast solar wind streams at 550 km/s. Here, no average values fall below 350 km/s, and none fall above 650 km/s, although, like density and temperature measurements, there are many individual events that surpass these limits.

The solar cycle certainly varies with the changing amount of activity on the solar surface, and this is observed through changes in the solar wind. Whole-cycle plots illustrate the true nature of the relationship between the number of sunspot observed on the surface and the ambient solar wind conditions. The STEREO spacecraft, which launched into solar minimum conditions, will most likely experience somewhat calmer conditions as they search for solar wind

origins. The primary objective of the STEREO mission, however, is the study of CMEs. Hence, we ask ourselves, does the number of CMEs vary with the solar cycle, or is it an independent process?

4.6. CORONAL MASS EJECTIONS AND THE SOLAR CYCLE

Are coronal mass ejections (CMEs) connected to the solar cycle? As their origin is not well understood, it is difficult to determine whether or not they will increase or decrease in number as the STEREO spacecraft flies in the solar minimum and eventually in the rising phase of solar cycle 24. To start an analysis of the occurrence of CMEs during the solar cycle, the LASCO instrument on board the SOHO spacecraft has kept a log of all CME events since its launch in 1996. The log, called the LASCO CME Catalog, keeps track of CME events for each day of the years since it has been orbiting. To use this data in a quantitative analysis, I counted the number of CMEs that occurred per day, starting in 1996. After finding the total per day, I averaged these values into monthly averages for each month within solar cycle 23. I used these monthly averages to plot the averages number of CMEs per day per month for solar cycle 23. This plot is shown in Figure 119.

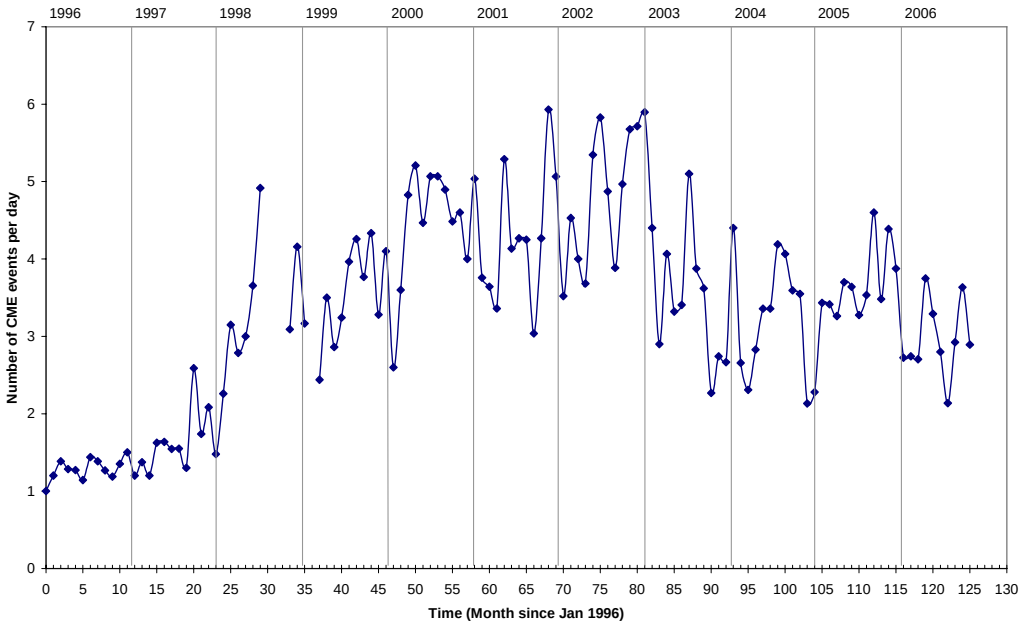

Figure 119. A graph plotting the average number of CME events per day per month for solar cycle 23. Data courtesy of the SOHO LASCO CME Catalog.[xlii]

Missing data from July through August of 1998 and January of 1999 are due to instrument maintenance on the SOHO spacecraft during these periods. The y-axis on this plot shows the number of CME events observed per day, and the x-axis is measured in the number of months since January 1996, when the catalog began. For clarity, these months are broken up into their corresponding years by the vertical lines and year labels at the top of the plot. As shown, the number of CMEs occurring per day varies greatly, even within a single year. When I fit a trendline to the data, I find the observation shown in Figure 120.

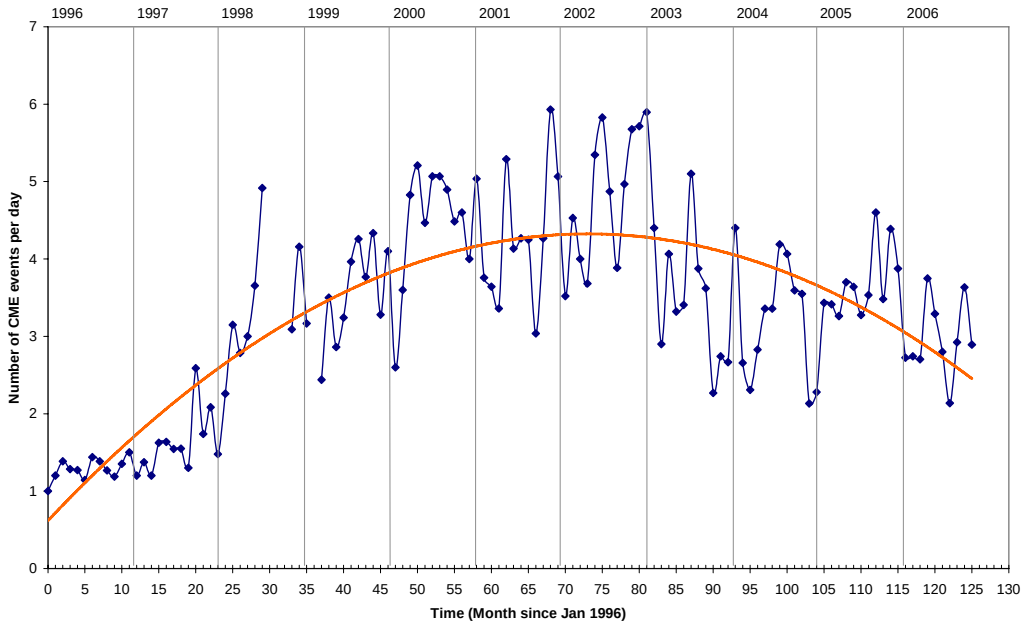

Figure 120. A similar plot to Figure 119, fitted with a trendline.

Figure 120 shows that the trend of this CME data is parabolic. More interesting, however, is the apparent connection between the number of CMEs per day and the solar cycle, as the peak of the trendline (and in the data itself) occurs around 2001, the solar maximum. This result suggests a connection between the cycle and CME events.

4.7. EFFECTS OF A CORONAL MASS EJECTION ON THE AMBIENT SOLAR WIND CONDITIONS

To study the effects of a CME on the measurements taken by a spacecraft of the ambient solar wind environment, as the PLASTIC instrument on STEREO does, I investigate a specific CME event recorded by the ACE and Wind spacecrafts. This CME, the effects of which lasted from May 1 through May 4, 1998, was the first strongly geoeffective CME of the previous solar cycle. Hence,

it is relevant to study it in depth here, as this is the period in which STEREO is flying. The "geoeffectiveness" of a CME has to do with how much it affects Earth as it passes. This particular CME may have been the cause of several power grid shutdowns, and caused several communications satellites, for example the Galaxy IV, to fail, which left 45 million people without pager service – or almost 80 percent of the United States' pager population.[xliii] These satellite failures were caused by the high flux of highly relativistic electrons (HREs) sent forth by the enormous solar storm. This particular CME carried the highest amount of power within it of any in recent history, making it extremely powerful in terms of geoeffectiveness. During this period, the solar surface, solar wind, and geomagnetic conditions around the Earth were highly disturbed. As these events are of great impact on the Earth, and their origins are unknown, the STEREO spacecraft has been launched to investigate. This specific CME is important to study, as it occurred during a similar time to the present in the previous solar cycle, and so it will be similar to what is expected for STEREO observations. Also, as an example of how a CME can affect the overall space environment, it is a prime sample event as its effects are large and relatively easy to see.

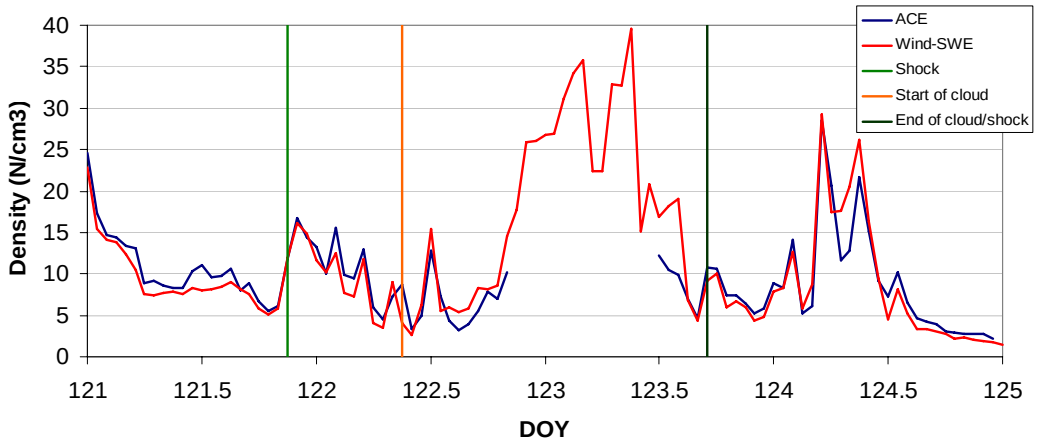

Figure 121. Solar wind density over the period 1-4 May 1998, showing the boundaries of the CME event as they passed the spacecraft. Both ACE and Wind-SWE data is shown to make up for data gaps in each.

Figure 121 shows a plot of the measured particle density for the days 1-4 May 1998. The first line at the left shows the start of the shock that preceded the CME material. This shock is caused by the fast moving CME material running into slower wind streams ahead of it. The next line to the right represents the start of the magnetic cloud within the CME, as the CME material carries magnetic field lines within it. The third line on the right represents the end of the shock and cloud, and therefore the departing edge of the CME as it passes by the spacecraft on its way towards Earth and the rest of the planets.

As shown here in Figure 121, the density begins to increase as the shock moves past the spacecraft. This is understandable, as the fast CME material pushes up behind the ambient solar wind materials. As the fast material is slowed by the ambient wind material, the density initially increases. However, after the initial shock, the density decreases as the slower material speeds up due to the push by the fast CME material behind it. It continues to vary as the faster

material slows and the slow material speeds up, depending on the strength of the stream passing the spacecraft. The amount of fast CME material moving past the spacecraft can measure up to one billion tons of material in a single event. The density again increases slightly at the start of the magnetic cloud due to the increased amount of material around the magnetic field of the CME. There is a major increase in the density in the second half of the cloud. Usually the overall density in a magnetic cloud decreases, but sometimes higher densities are seen - usually at the end of the cloud - and it is assumed these have to do with some solar structure. A big density spike at an end of a cloud, as seen here in Figure 121, is often suspected to be a remnant of the filament (here composition is a key diagnostic). The density increases again slightly at the end of the cloud (and shock) as the last of the fast material pushes slow material out of the way. As shown after day-of-year 124, another much smaller CME passed by the spacecraft a few hours after this CME passed. May of 1998 was an extremely active period in the previous solar cycle.

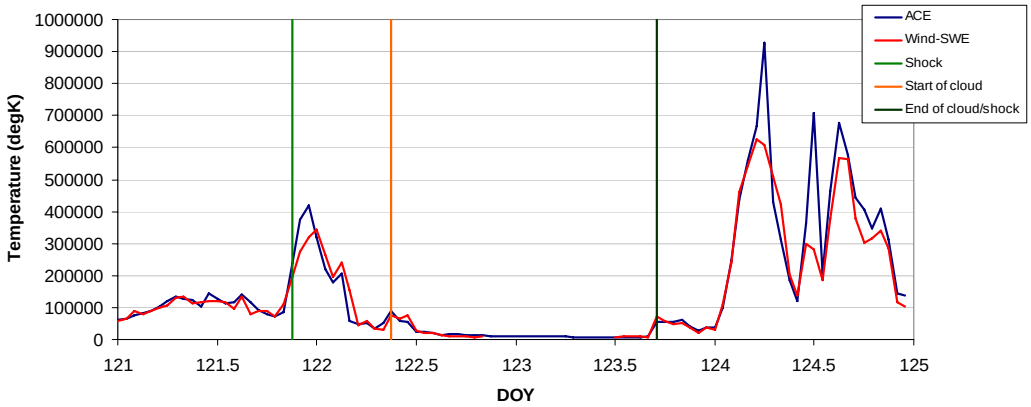

Figure 122. A plot of the measured solar wind environment temperature by the ACE and Wind-SWE spacecrafts during the CME event of 1-4 May 1998.

Figure 122 shows the plot of temperature measurements taken by the ACE spacecraft and the SWE instrument on the Wind spacecraft. As shown, as the shock passed the spacecraft, the temperature increased slightly. This is due to the hot, fast material emitted as CME material by the Sun. However, when the magnetic cloud begins, the temperature drops to extreme lows for the duration of the passage of the magnetic cloud. As will also be shown with speed, and was already shown with density, this is a characteristic sign that a CME is passing a spacecraft. This major decrease in temperature is somewhat complicated. Part of the functional definition of a magnetic cloud is that is exhibit an abnormally low proton kinetic temperature. It is thought to be a consequence of a closed (or quasi-closed) magnetic structure (e.g. flux rope, loops, tongue, bottle) that is expanding faster than a quasi-stationary solar wind (or ambient solar wind) does. The cloud is a low beta plasma - meaning there is a lot of magnetic pressure in the cloud compared to the ambient solar wind - hence the expansion.

As shown, the temperature remains extremely low for the duration of the magnetic cloud, only increasing upon the end of the magnetically charged material. This low temperature measurement corresponds to the high density measurement observed by the spacecraft during this same period and displayed in Figure 121.

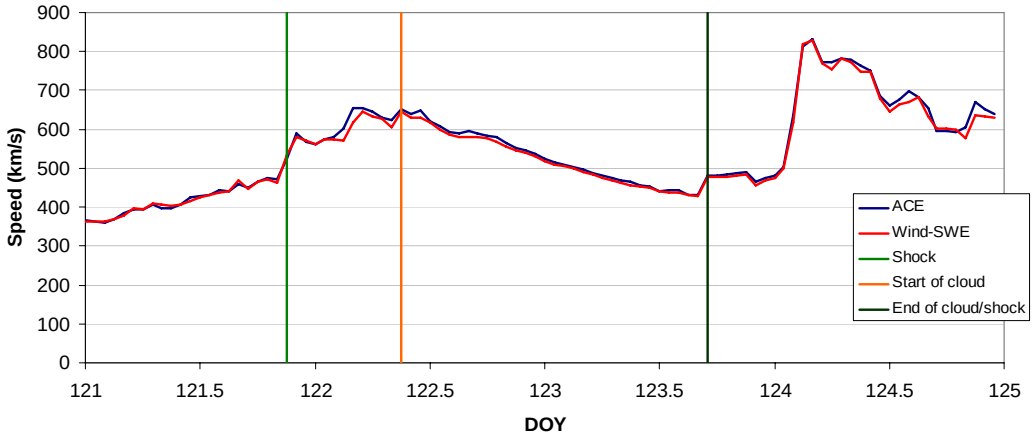

Figure 123. A plot of the solar wind speed measurements by the ACE and Wind-SWE spacecraft during the 1-4 May 1998 event

Figure 123 shows the corresponding plot of solar wind speeds measured during the 1-4 May 1998 event. As shown, the speed increases as the shock passes the spacecraft, since the shock represents the fast CME material moving up behind the slower ambient wind. Between the beginning of the shock and the beginning of the magnetic cloud, the speed varies as the strong stream of CME material pushes the slow stream ahead of it, and is conversely slowed by that slow material. As the magnetic cloud passes the spacecraft, the speed drops, which is a diagnostic trait of a possible CME passage. This stream is slowed by the magnetic field lines that constrain the particles, much like slow solar wind is emitted from closed field lines on the Sun. As the temperature of the material decreases and the density increases, the speed is decreased, as shown in this figure. After the passage of the cloud and end of the shock, the speed recovers to relatively normal conditions.

Though difficult to quantify with histograms like we do with the other parameters, the direction of the solar wind can also be affected by the passage of a CME, a trait that can be used to back-map to possible origin regions on the surface, which will be shown later.

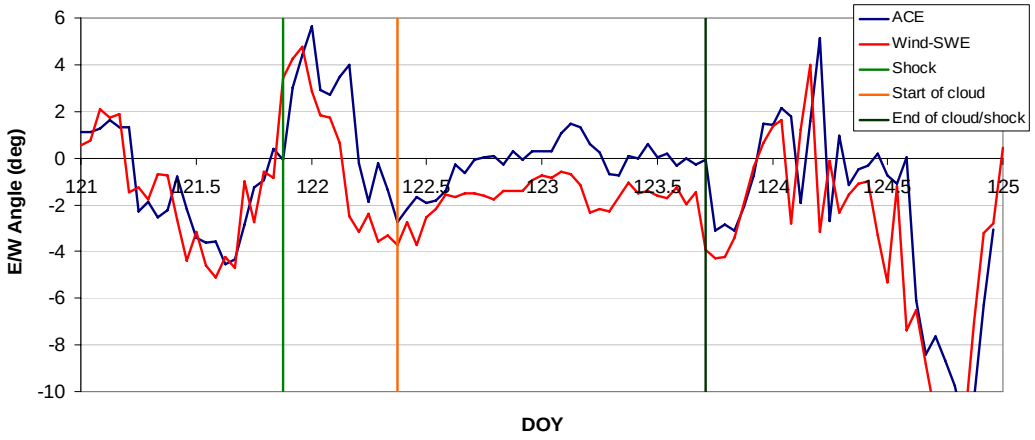

Figure 124. A plot of the E/W angle of the solar wind as measured by the ACE and Wind-SWE spacecraft

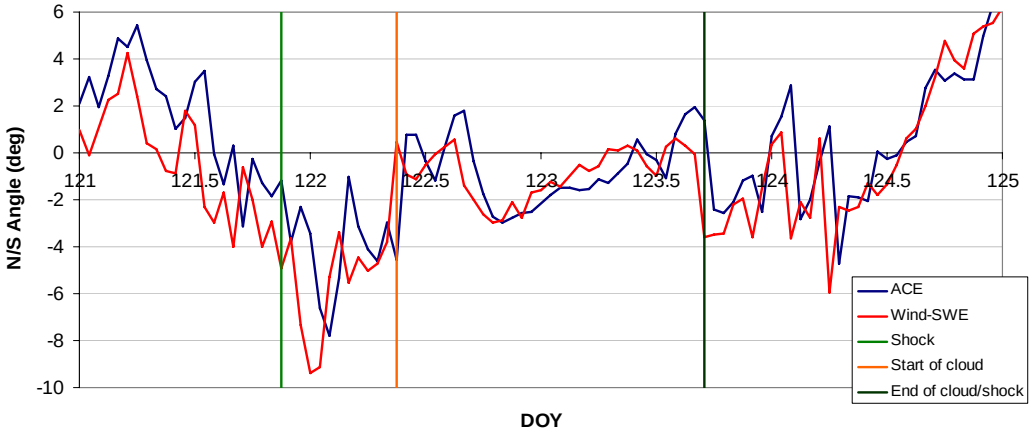

Figure 125. A plot of the N/S angle of the solar wind as measured by the ACE and Wind-SWE spacecraft.

In Figures 124 and 125 the direction components of the solar wind, as measured by the ACE and Wind-SWE spacecraft, are plotted. In Figure 124, the

E/W angle of the streams changes from an easterly wind (i.e. streams coming from the eastern hemisphere of the Sun) to a westerly wind as the shock passes. As the cloud starts, the stream becomes less easterly, and stays relatively close to the center of the Sun until the cloud passes and becomes immediately easterly again. The discrepancy between the two data sets can be attributed to the different locations at which the spacecraft were orbiting – spacecraft located at different longitudes with respect to the Sun will record slightly different angles.

In Figure 125, the wind is equally varying in the N/S direction. As soon as the shock passes the spacecraft, it becomes increasingly angled from the south of the equator of the Sun. It returns to streaming from around the equator when the start of the magnetic cloud passes, and varies, similarly to the E/W angle in Figure 124, around the center of the Sun while the cloud passes. At the end of the cloud, the direction changes drastically again to come from the southern hemisphere.

These results, for both the E/W angle and N/S angle are expected. As the magnetic cloud passes, carrying the highly charged particles of the CME, the direction of this material seems to be from the relative center of the Sun. This makes sense, because these CMEs, from the relative center of the Sun, are the ones that are directed towards the Earth.

The 1-4 May 1998 event was chronicled in the paper by Farrugia et al.[xliv], as it was the most powerful interplanetary coronal mass ejection (ICME) in recent history. Figure 126 shows direct measurements of the Wind-SWE spacecraft of

the solar wind speed for the entire months of April and May 1998 to contrast the normal space environment conditions with the highly disturbed days of May 1-4.

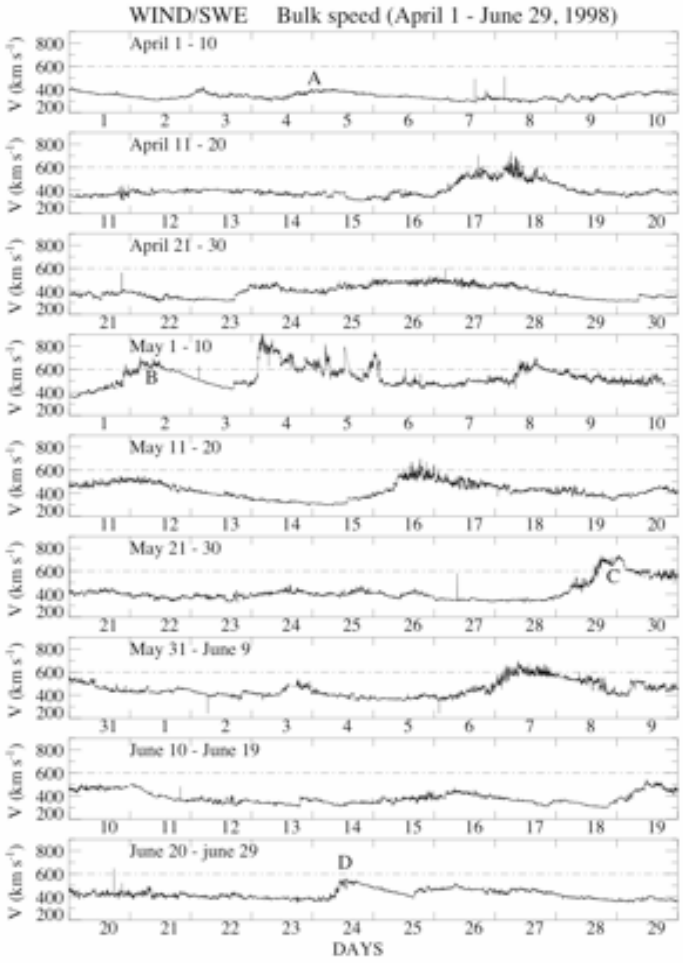

Figure 126. A plot courtesy of C. J. Farrugia et al. of the Wind-SWE measurements of the solar wind speed for April and May 1998. Note the irregularity of the measurements taken starting May 1, and especially of the event on May 4.

The event on May 4, which carried the most power in recent years, seems to have formed from the halo CME observed by SOHO/LASCO (which began April 29) that was associated with an M-class flare observed by the GOES

spacecraft. This radially-expanding CME was observed on May 2-3, and was followed by an exceedingly fast stream on May 4, with speeds surpassing 900 km/s. This is shown in Figure 126 – in fact, the event on May 4 is the only event to have speeds above 600 km/s for all of April and May (the 600 km/s mark is denoted by the dotted line in the plot). Because of this, it was deduced that this interplanetary event was a compound stream containing both transient and corotating aspects. Thanks to energetic particle and composition observations, the events of 1-4 May could be connected to at least two different flare sites in the same active region of the Sun. This marked the first inference of a lower limit to the solar footprint of the magnetic cloud of 10^{10} km^2.[xlv] The STEREO mission may help to make such estimates more precise, more common, and easier to make overall.

The power, or energy deposition, of the ICME of May 1998 was calculated by Farrugia et al. using the Perreault-Akasofu parameter epsilon and computed over three hour periods. In Figure 127, the top panel shows the energy deposition over three days, and the bottom panel shows the rate of energy deposition (i.e. power) computed every three hours.

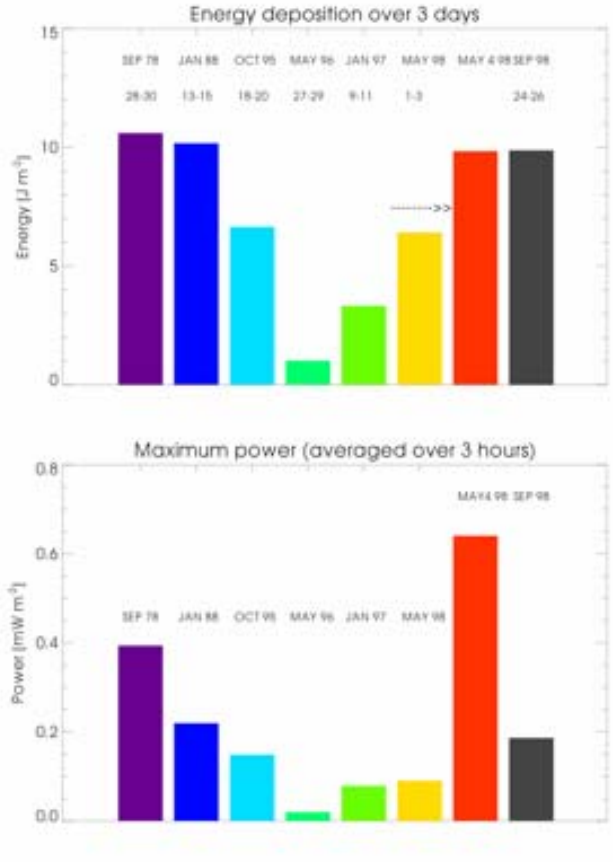

Figure 127. A diagram courtesy of Farrugia et al., showing the energy deposition of the 1-4 May 1998 event compared with other strong geoeffective CME events

While other strongly geoeffective events in the rising phase of solar cycle 23 had comparable energy depositions to that of 1-4 May 1998, the power over a three-hour period on May 4, 1998 exceeded by far that of the other events. The extreme values of the May 4 part of the event can also be observed in the plots in Figures 121 to 125 above, occurring on day-of-year (DOY) 124. This example of how a CME can affect the space weather conditions is an extreme example – this event was classified as an interplanetary coronal mass ejection (ICME) because of

its large size. There are many large CMEs that are not geoeffective as well – the only ones that effect Earth are the "halo CMEs", which are directed at the Earth along the ecliptic.

A sign of the geoeffectiveness of a particular event can be found in the DST index. The DST index is a geomagnetic index which monitors the world wide magnetic storm level. It measures the interaction between the solar wind and the ring current in Earth's magnetosphere. The more negative the DST index, the more intense the storm – these storms are called geomagnetic storms. These "storms" are actually major disruptions of the Earth's magnetic field. A readout of the DST index for the month of May is shown in Figure 128. As shown, the DST index dips low on the interval in question, indicating a large geomagnetic storm occurring in the magnetosphere of the Earth. This is the cause of many power grid and satellite failures.

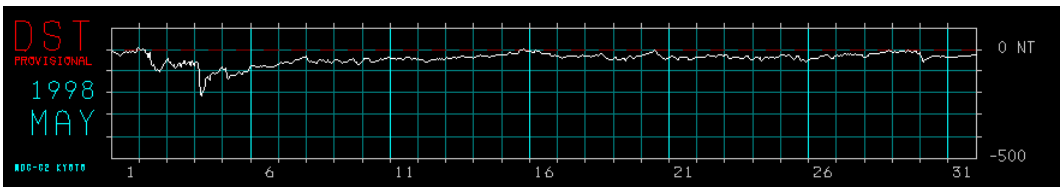

Figure 128. A readout of the DST index for the month of May 1998 shows a large decrease during the 1-4 May period, indicating a geomagnetic storm

A view of the solar surface during the 1-4 May 1998 period is also irregular. Both the solar wind environment and the solar surface were extremely disturbed during this time. Figure 129 shows the Sun over the days April 29 through May 6, 1998.

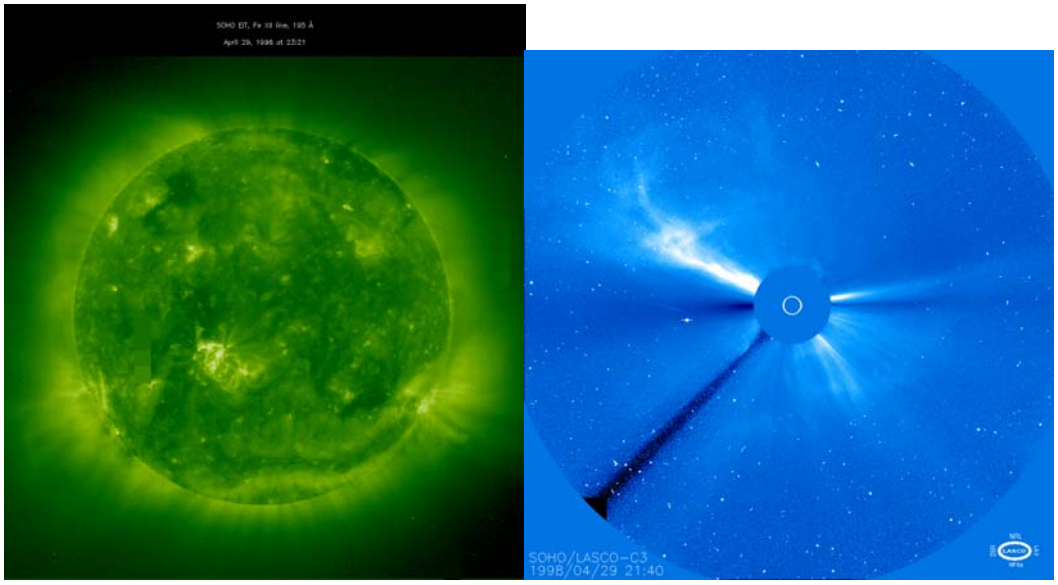

a) April 29, 1998

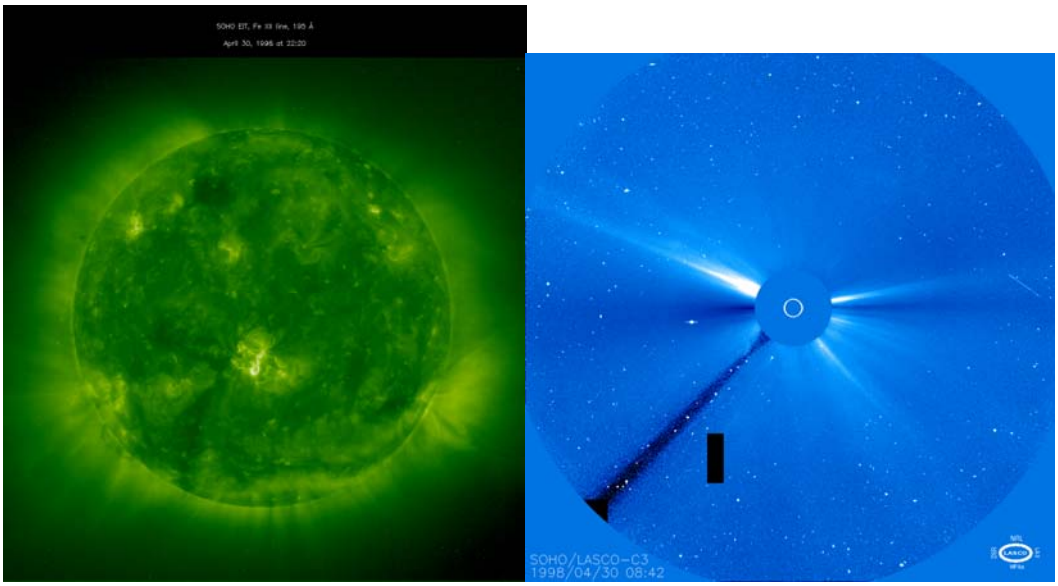

b) April 30, 1998

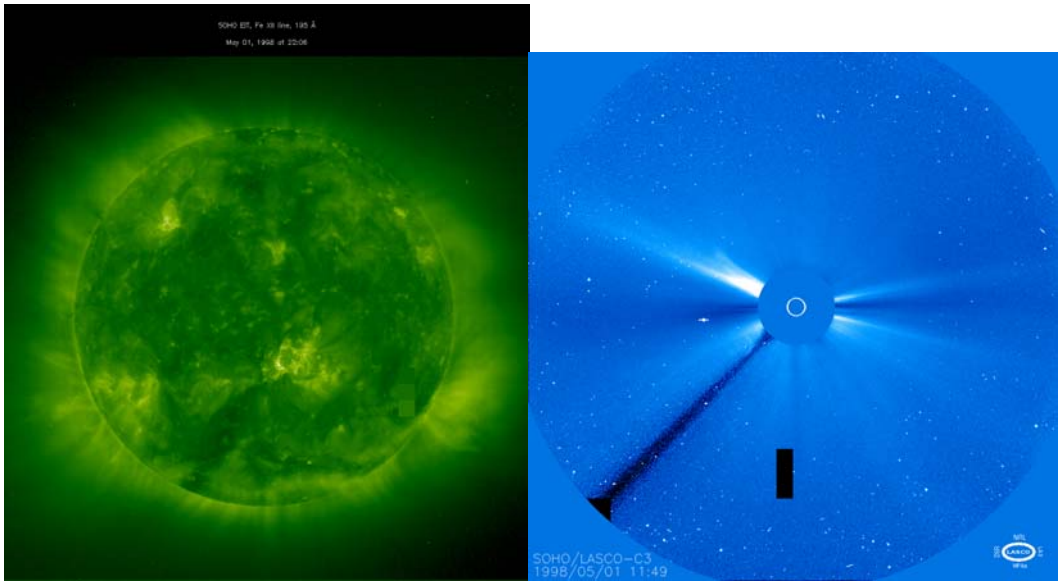

c) May 1, 1998

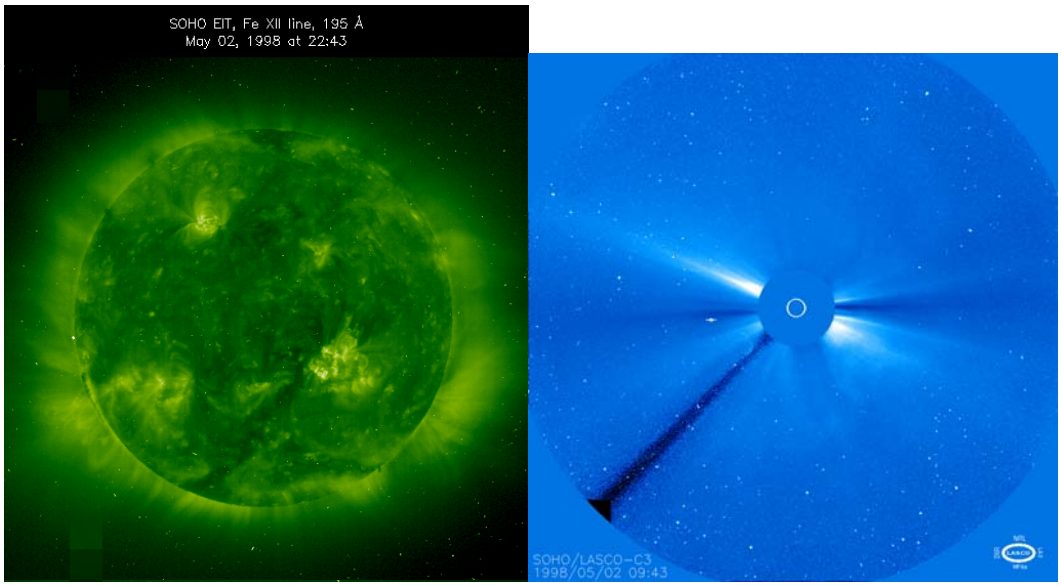

d) May 2, 1998

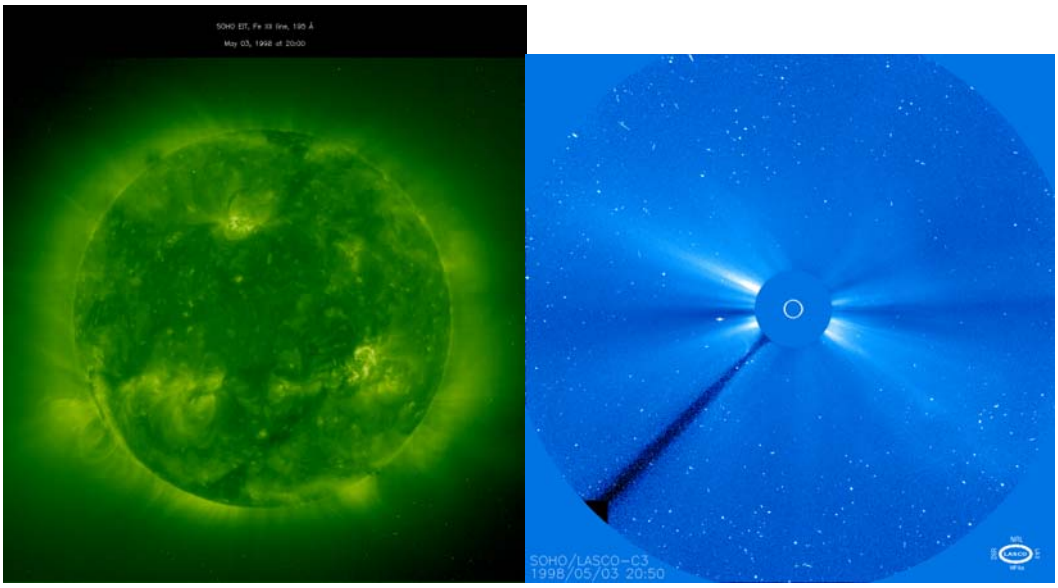

e) May 3, 1998

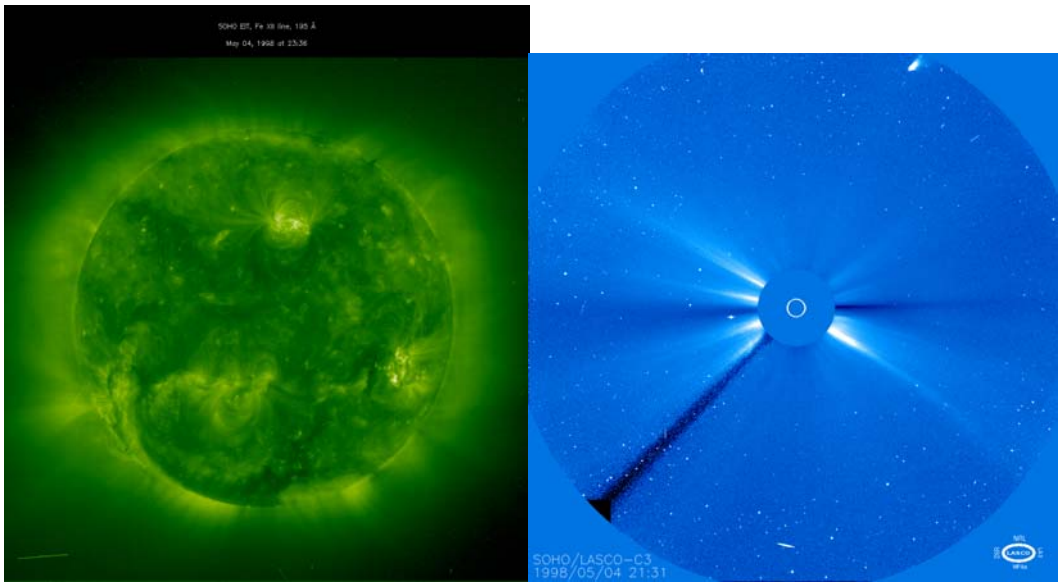

f) May 4, 1998

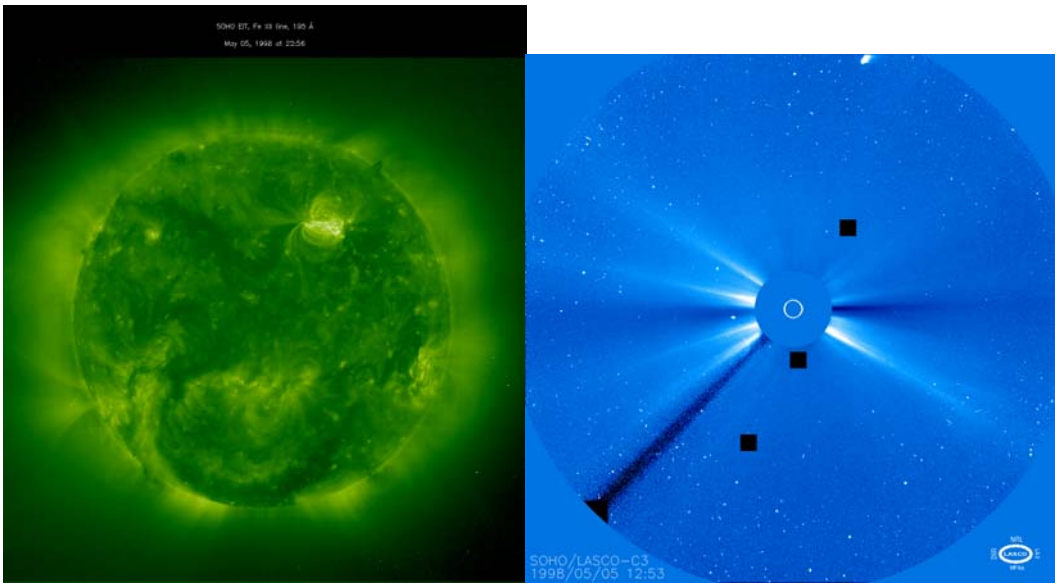

g) May 5, 1998

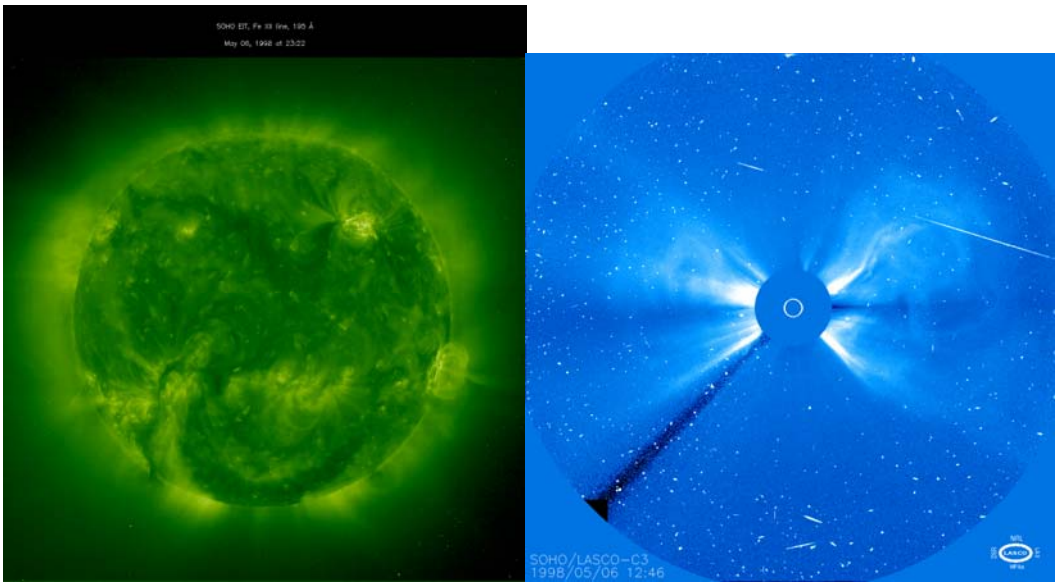

h) May 6, 1998

Figure 129. The 16 images above, from the SOHO spacecraft, show the progression of the solar conditions over April 29 through May 6. The images on the left are from the EIT imaging instrument, which imaged the Sun's surface in ultraviolet (195Å). The images on the right are from the LASCO C3 imaging instrument, showing the outer corona and state of the solar wind out to 1 AU.[xlvi]

As shown in this series of images in Figure 129, the Sun and its surface were extremely perturbed during the period in question. There are many active regions shown as the Sun revolves, and there are three especially prominent regions of activity in the May 1-4 images, all concentrated towards the front and center of the Sun, putting them in good positions to emit material towards the Earth. In the images on the right, a large amount of material can be seen leaving the Sun each day during this period, represented by the white rays extending radially outward.

Since this event occurred during a similar time in the previous solar cycle, it is a good example of what to expect for STEREO observations as we enter the rising phase of solar cycle 24. Although such a large event may not be observed this time around, it provides a good model for the effects of such an event on the ambient solar wind that the STEREO spacecraft will measure.

4.8. CORRELATING THE SPACE WEATHER ENVIRONMENT WITH SUN SURFACE CONDITIONS

As we analyzed the solar surface conditions for the May 1-4 1998 event, we also analyzed SOHO remote sensing data for the entire cycle. In doing so, we can look at the trends we saw in the *in-situ* data and compare those analyses with Sun surface conditions.

The following images show the Sun, at both 196Å and 304Å on the EIT imager, at seven points during the solar cycle: minimum, early rising phase, late rising phase, maximum, early declining phase, late declining phase, minimum.

As the cycle progresses, the Sun's surface clearly changes. This shows that the number of sunspots, though these were the original idea behind the solar cycle, are not the only regions of the surface that increase and decrease in area over the cycle.

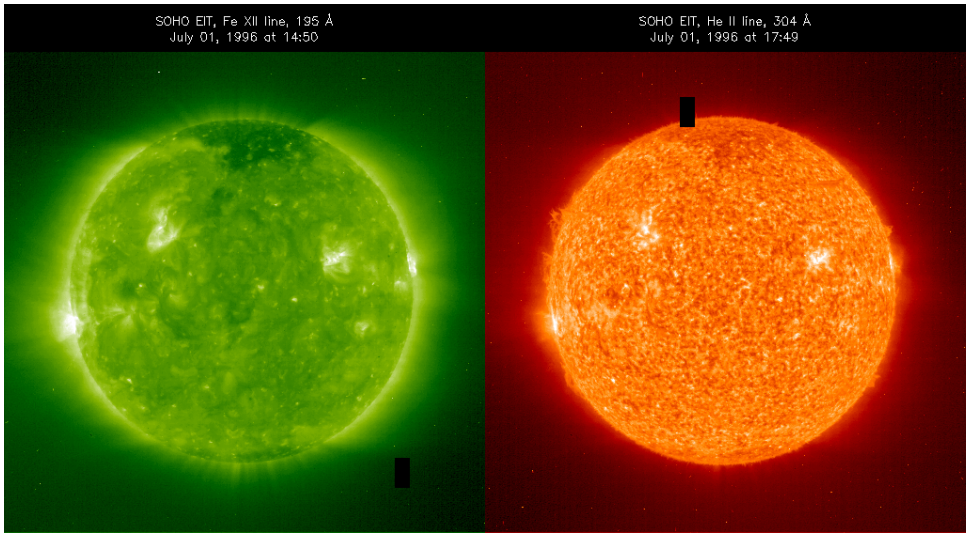

a) July 1996 – Solar Minimum

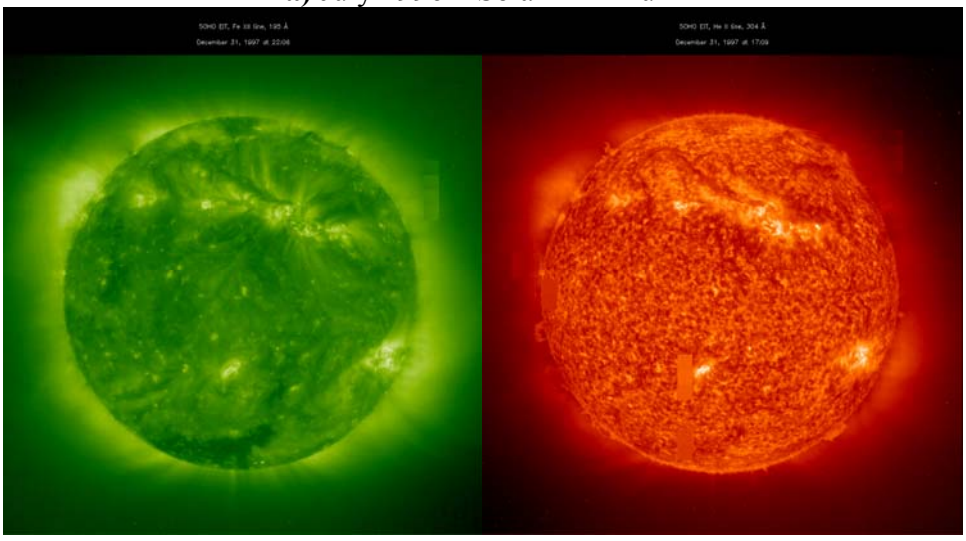

b) December 1997 – Early Rising Phase

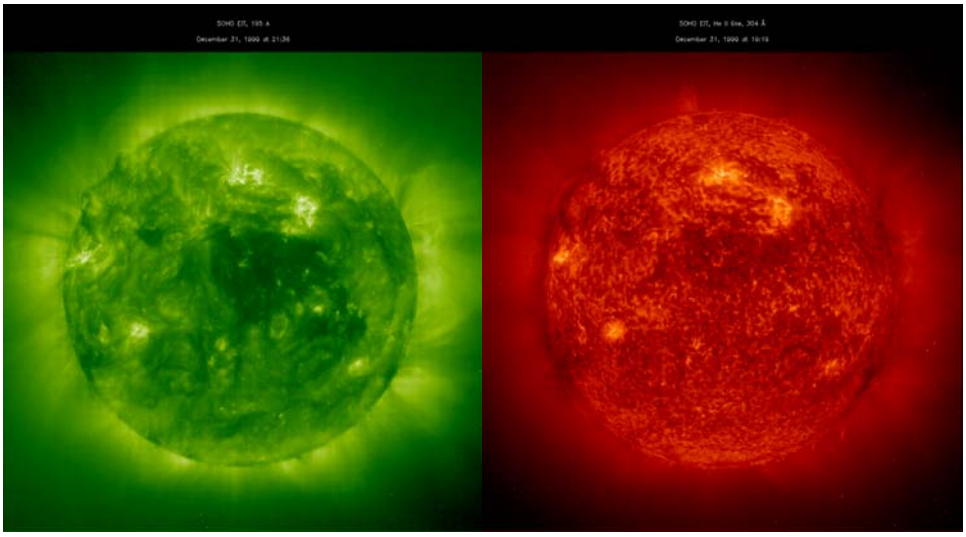

c) December 1999 – Late Rising Phase

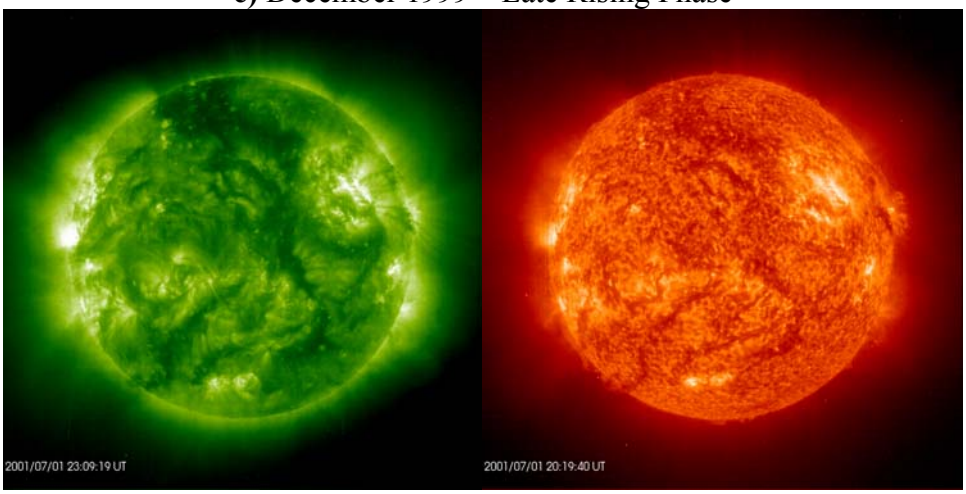

d) July 2001 – Solar Maximum

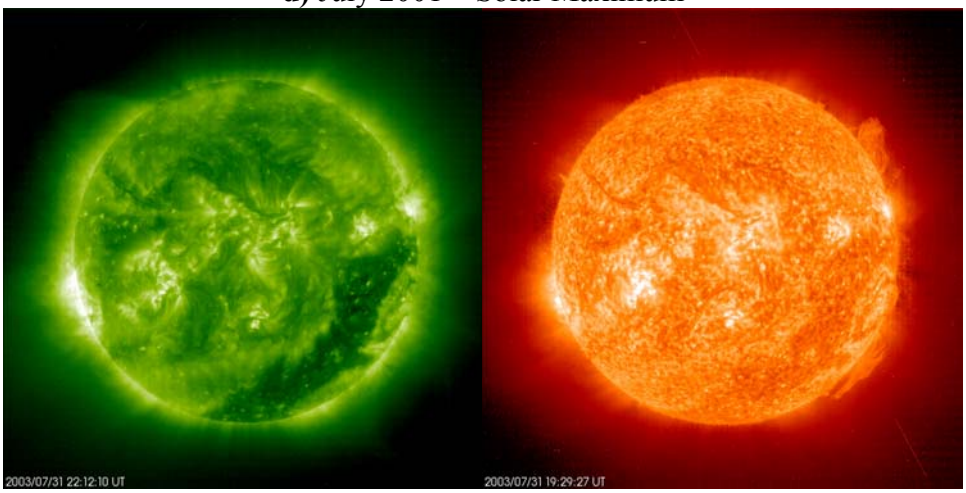

e) July 2003 – Early Declining Phase

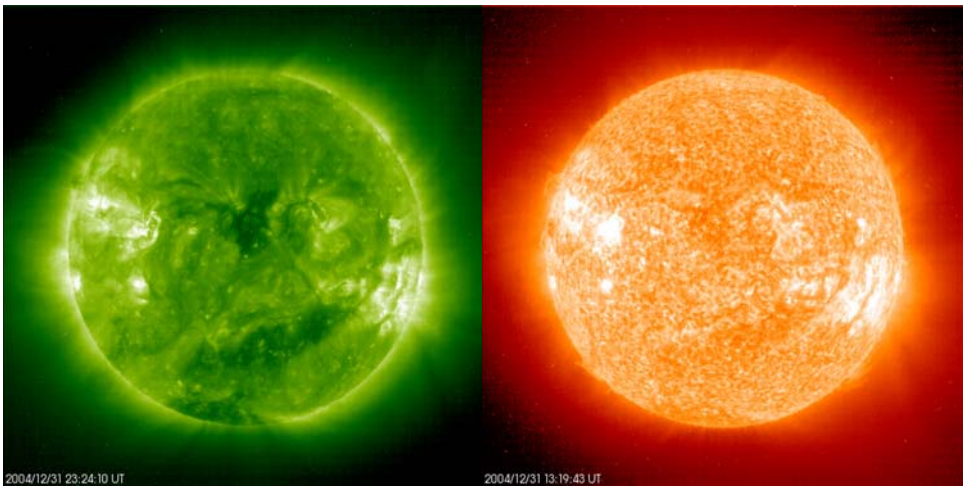

f) December 2004 – Late Declining Phase

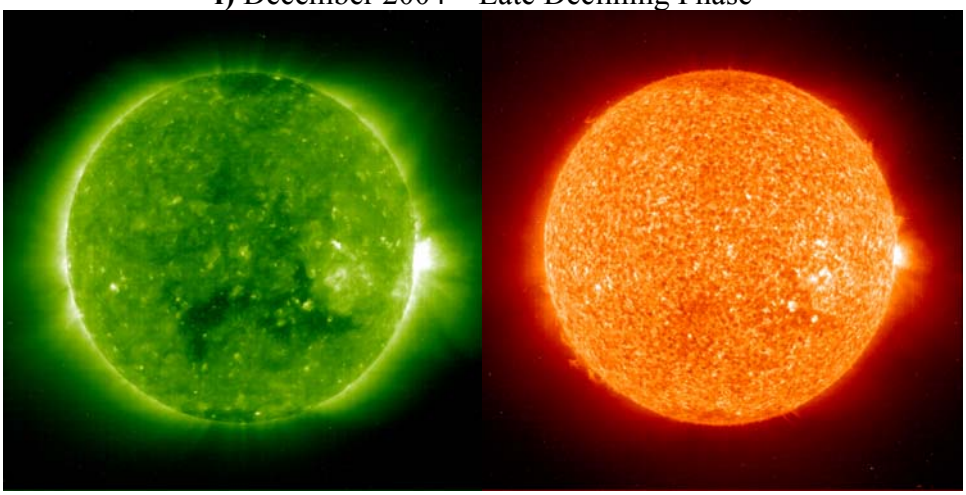

g) December 2006 – Solar Minimum

Figure 130. Figures a through g show various states of the solar surface during the cycle.[xlvii]

When we compare these results to our analyses of the *in-situ* data from solar cycle 23, it is easy to see a connection between the solar wind conditions and these surface conditions. In Figure 130a), from the solar minimum in 1996, there are few active regions, and a coronal hole at the northern pole – a normal occurrence for a solar minimum. The rest of the surface appears relatively calm. In the next image, Figure 130b), more active regions start to appear as the Sun begins the rising phase of the cycle. The polar holes begin to migrate – especially

noticeable is the southern polar hole, which was not visible in the previous image, but has moved up in latitude in this image. Figure 130c) was taken in December 1999, well into the rising phase of the cycle. Clearly, the polar hole has moved into the center of the sun, and there are also many more active regions. Also visible in silhouette around the edge of the disk are the increasingly perturbed field lines, illuminated by energetic particles flowing around them. This increase in active regions and perturbed field lines looping out of the Sun is the cause of the trend noticed in the *in-situ* data, where the lowest speeds and temperatures were observed during the rising phase. These looped field lines trap particles and cause the streams off of the Sun to be slower and cooler, and hence, as seen in the *in-situ* data, the highest densities are observed in the rising phase.

Figure 130d) was taken in July 2001, in the middle of the solar maximum. The coronal holes have moved in and taken over much of the surface, mixed in with many active regions. This is the point at which the magnetic field lines of the Sun are the most perturbed, and hence, the surface exhibits an extremely disturbed appearance. This violent atmosphere lends itself to emitting a large range of extreme solar wind values. The next image, in Figure 130e), was taken during the declining phase. A later period of the declining phase is shown in Figure 130f). These images show the coronal holes toward the center of the Sun, and a decreased number of active regions during this period. Both of these factors lend themselves to agree with the trend noted in the in-situ data, where the declining phase showed the highest temperatures and speeds of the solar wind for

the whole cycle. This is because, with fewer active regions and increased coronal holes aimed at Earth, more fast streams are emitted. These hot, fast streams make it such that the lowest densities are recorded during this time.

Figure 130g) shows the most recent solar minimum, in December 2006. The Sun's surface has returned to a relatively calm environment, exhibiting the trademark polar holes and very few active regions. Although this is a big picture overview of how remote sensing data can be used along side *in-situ* data to diagnose solar conditions both on and around the Sun, it is a good model for how we used this kind of relationship to assess several individual events[xlviii], for example, the event that occurred on 1-4 May 1998.

CHAPTER 5

CONCLUSION

The plasma that flows outward from the Sun is actually a continuation of the solar atmosphere into interstellar space. This solar wind, which passes by each planet in the solar system and affects them each as it does so, ends its dominating influence at the heliopause, or interstellar boundary. At this point, the solar wind particles are slowed enough to be subsonic, and therefore are overpowered by the interstellar winds that move through space – or more accurately, as the heliosphere moves through interstellar space. The heliosphere is constantly changing shape, its interstellar boundary constantly growing and shrinking. Though this has long been theory, it has since been proved as the Voyager 2 spacecraft passed by the boundary, and was later passed by the boundary as it once again expanded. The Interstellar Boundary Explorer (IBEX) mission will study this effect in-depth, and is currently in the testing phases at the University of New Hampshire. This boundary fluctuates due to changes in the solar wind output by the Sun, and so it is important to understand the changes that the Sun experiences during its 11-year cycle.

The changes in activity on the surface of the Sun cause variations in the solar wind output by the corona. During the solar cycle, the ambient solar wind consists of fast solar wind, measuring between 600 and 800 km/s, and slow solar wind, measuring between 200 and 600 km/s. Transient solar winds, which are spontaneous and somewhat unpredictable, include coronal mass ejections (CMEs), flares, and solar energetic particle (SEP) events. The causes of these sudden solar storms are relatively obscure, and hence the Solar Terrestrial Relations Observatory (STEREO) mission has been launched to study their origins, using two identical spacecraft in order to achieve stereo observations of the solar environment. The goal of the mission is to improve space weather forecasting by gaining knowledge of CME origins.

The most recent solar minimum occurred in 1996, and the Sun is now experiencing a minimum. The last solar maximum occurred in 2001 (with a possible double maximum in 2000). The solar wind has been shown to vary over these years. Although the changes between individual years are somewhat small, when comparing the solar maximum year and solar minimum year, large differences in activity are observed. The increased number of active regions on the Sun cause more violent conditions in the space environment. Generally, although the fast and slow solar winds are always present, the wind exhibits a much larger range during the years surrounding the solar maximum than those around the solar minimum. In addition, in this thesis it was observed that the number of CMEs per day occurring in the solar maximum followed a cyclic

pattern, suggesting that the origins may be connected to active regions and largely perturbed magnetic fields.

Studying the effects of a CME on the ambient solar wind showed characteristic appearances of a passing CME on data instruments. Using a highly geoeffective ICME that occurred during a similar time period in the previous solar cycle (solar cycle 23) allowed us to prepare for possible similar occurrences during STEREO's flight in the early rising phase of solar cycle 24. Using data from the first five months of the previous solar cycle, we were also able to predict space weather conditions for the STEREO spacecraft, which were then used to calibrate the instrument during testing – especially angle measurements. Using angle measurements from the previous solar cycle, we were able to predict probable angle ranges of the solar wind this time around, such that PLASTIC instrument engineers could angle the Wide Angle Partition (WAP) to get the most particles into the instrument as possible. We made our predictions for each parameter using histograms of the first five Carrington rotations of solar cycle 23, combining this data with averages, ranges, and modal values to find the following predictions for space weather conditions for STEREO's first few months of operation.

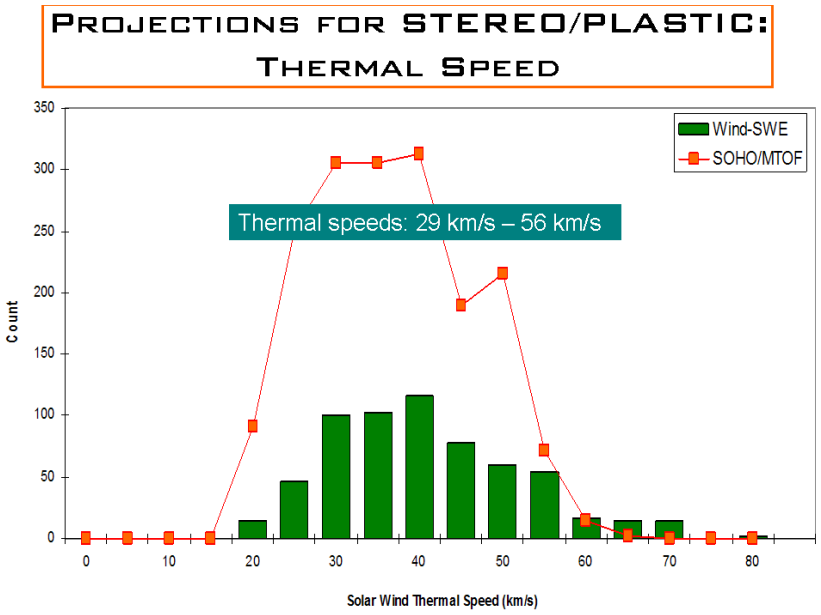

Figure 132. Based on data from the Wind spacecraft and SOHO spacecraft over the first five Carrington rotations of solar cycle 23, STEREO should normally experience thermal speeds between 29 and 56 km/s in the first few months of its flight into the rising stage of solar cycle 24.

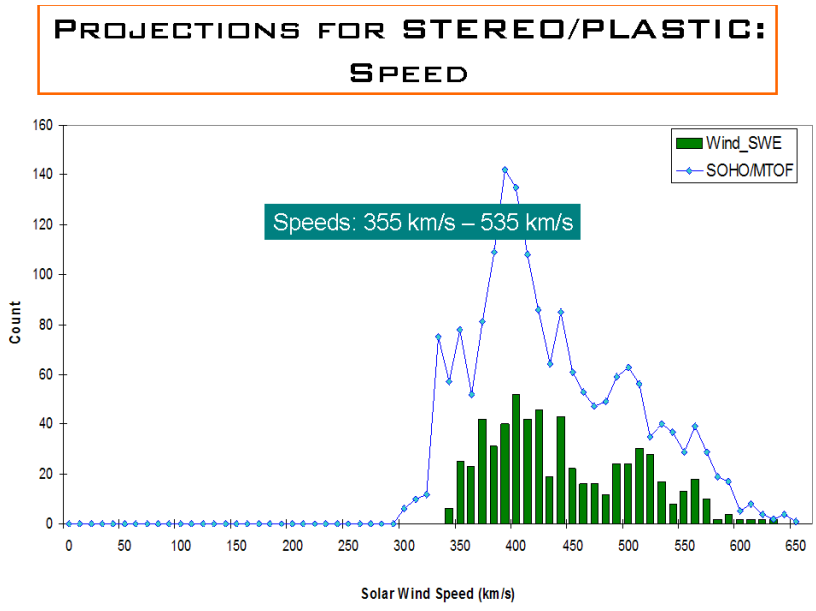

Figure 133. STEREO should normally find solar wind speeds between 355 and 535 km/s during its first few months in flight.

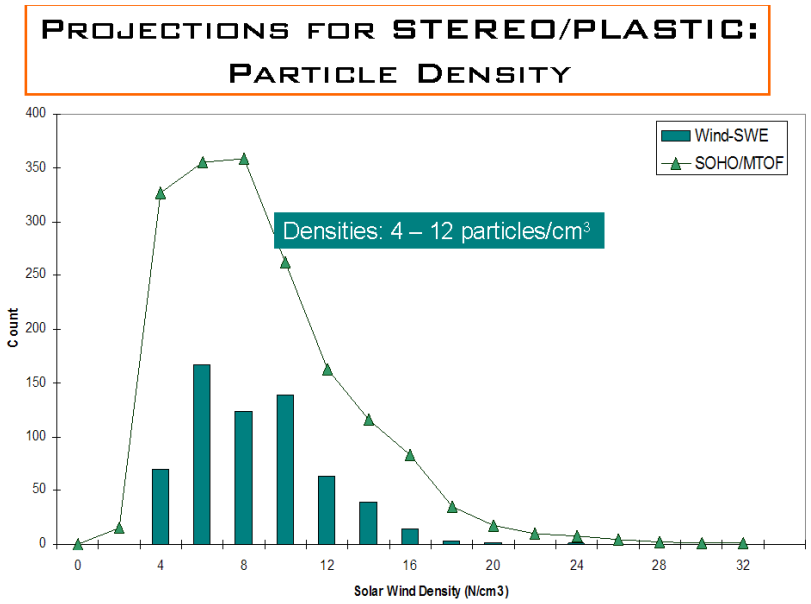

Figure 134. The density range that STEREO may experience on an average day will be between 4 and 12 p/cm3.

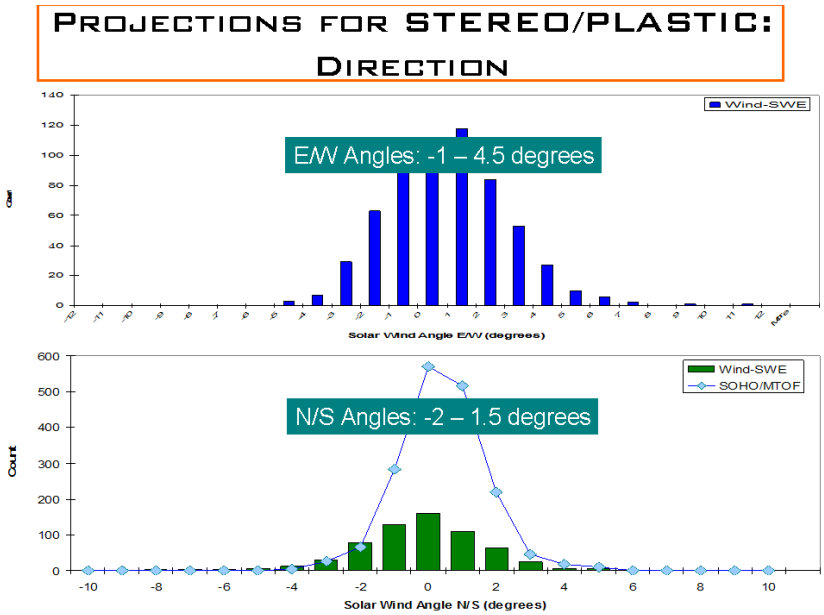

Figure 135. The E/W component of the solar wind will most likely vary between -1° and 4.5°. The N/S component should vary between -2° and 1.5°.

These predictions, although they may be somewhat rudimentary, help PLASTIC scientists to make sure that the data being returned is on par with previous studies.[xlix]

Indeed, STEREO has launched into an interesting time during the solar cycle. At the beginning of its mission, the Sun is at its calmest, and hence the instruments can be calibrated and checked, and scientists can take their time in processing the fewer amount of CMEs exploding of off the Sun for the first few months. As the mission goes on, however, STEREO will observe the Sun becoming increasing entangled in its own magnetic field. This will produce increasingly violent events in the corona, which STEREO will be able to image and catch in three dimensions. Not only will STEREO assist in future space weather prediction, but in its quest to find the origins of coronal mass ejections, it will make interplanetary space safer for those of us here on Earth, satellites, and future manned space missions that will travel beyond the reaches of Earth's protective magnetosphere.

ADDITIONAL RESOURCES

Benz, A.O., *Plasma Astrophysics: Kinetic Processes in Solar and Stellar Coronae*, Luwer Academic Publishers, Dordrecht, Netherlands, 1993

Cho, K.S. et al., *A statistical comparison of interplanetary shock and CME propagation models*, Journal of Geophysical Research, Vol. 108, No. A12, 1445, 2003

Galvin, A.B., Turco, S., *Phase A Concept Study Technical Report: Plasma and Suprathermal Ion Composition (PLASTIC) Investigation on STEREO*, Volume 1: Technical Section, Final Report for NASA Contract NAS5-00132, University of New Hampshire, 2000

Gosling, J. et al, *Anomalously low proton temperatures in the solar wind following interplanetary shock waves - Evidence for magnetic bottles?,* Journal Geophysical Research, Vol. 78, pg. 2001, 1973

Jackson, B.V. et al., *Preliminary three-dimensional analysis of the heliospheric response to the 28 October 2003 CME using SMEI white-light observations*, Journal of Geophysical Research, Vol. 111, A04S91, 2006

Kataoka, R. et al., *Downstream structures of interplanetary fast shocks associated with coronal mass ejections*, Geophysical Research Letters, Vol. 32, L12103, 2005

Kim, R.S. et al., *Forecast of the coronal mass ejection (CME) geoeffectiveness using halo CMEs from 1997 to 2003*, Journal of Geophysical Research, Vol. 110, A11104, 2005

Ko, Y. et al., *Abundance variation at the vicinity of an active region and the coronal origin of the slow solar wind*, The Astrophysical Journal, 646:1275-1287, 2006 August 1

Kuwabara, T. et al., *Geometry of an interplanetary CME on October 29, 2003 deduced from cosmic rays*, Geophysical Reserach Letters, Vol. 31, L19803, 2004

Lepri, S.T. et al., *Iron charge distribution as an identifier of interplanetary coronal mass ejections*, Journal of Geophysical Research, Vol. 106, No. A12, pgs. 29,231-29,238, 2001

Puhl-Quinn, P.A. et al., *Cluster Observations of Enhanced Convection in the Ring Current Region*, Journal of Geophysical Research, submitted July 2004

Rastatter, L. et al., *Magnetic field topology during July 14-16 2000 (Bastille Day) solar CME event*, Geophysical Research Letters, Vol. 29, No. 15, 1747, 2002

Richardson, I.G., et al., *Solar cycle variation of low density solar wind during more than three solar cycles*, Geophysical Research Letters, Vol. 27, No. 23, pgs. 3761-3764, 2000

RESOURCES CITED

[i] Steigerwald, B., *Feature: Voyager Enters Solar System's Final Frontier*, NASA Goddard Space Flight Center, May 24, 2005

[ii] National Aeronautics and Space Administration, World Book Encyclopedia, *The Sun*, http://www.nasa.gov/worldbook/sun_worldbook.html

[iii] Phillips, K.J.H., *Guide to the Sun*, Rutherford Appleton Laboratory, Oxfordshire, UK. Cambridge University Press 1992. p. 47

[iv] Meyer, J.P., *Solar-stellar Outer Atmosphere and Energetic Particles, and Galactic Cosmic Rays*. *Astrophysical Journal 57: 173-204.* 1985

[v] Phillips, K.J.H., *Guide to the Sun*, Rutherford Appleton Laboratory, Oxfordshire, UK., Cambridge University Press, 1992. p. 67-68

[vi] Tandberg-Hanssen, E., *Solar Activity*, High Altitude Observatory, National Center for Atmospheric Research, Blaisdell Publishing Company, Waltham, MA. 1967 p. 220

[vii] Howe, Rachel. *The Beat Goes On – Inside the Sun*. National Optical Astronomy Observatories, Release Number 00-03. March 30, 2000.

[viii] Phillips, K.J.H., *Guide to the Sun*, Rutherford Appleton Laboratory, Oxfordshire, UK., Cambridge University Press, 1992. p. 68

[ix] Hale, G.E., Nicholson, S.B., *The Law of Sun-Spot Polarity*, Astrophysical Journal, vol. 62, p.270, November 1925

[x] Tandberg-Hanssen, E., *Solar Activity*, High Altitude Observatory, National Center for Atmospheric Research, Blaisdell Publishing Company, Waltham, MA. 1967 p. 173

[xi] Phillips, K.J.H., *Guide to the Sun*, Rutherford Appleton Laboratory, Oxfordshire, UK., Cambridge University Press, 1992. p. 70

[xii] Ibid. p.12

[xiii] Jursa, A.S., ed., *Handbook of Geophysics and the Space Environment*, Air Force Geophysics Laboratory, Air Force Systems Command, Unites States Air Force, 1985, Document Accession Number: ADA 167000, p. 1-18

[xiv] Phillips, K.J.H., *Guide to the Sun*, Rutherford Appleton Laboratory, Oxfordshire, UK., Cambridge University Press, 1992. p. 187

[xv] Tandberg-Hanssen, E., *Solar Activity*, High Altitude Observatory, National Center for Atmospheric Research, Blaisdell Publishing Company, Waltham, MA. 1967. p.239-313

[xvi] Phillips, K.J.H., *Guide to the Sun*, Rutherford Appleton Laboratory, Oxfordshire, UK., Cambridge University Press, 1992. p.188

[xvii] Phillips, K.J.H., *Guide to the Sun*, Rutherford Appleton Laboratory, Oxfordshire, UK., Cambridge University Press, 1992. p. 152

[xviii] Marsch, E., Chuanyi, T., *Solar Wind Origin in Coronal Funnels*, Max Planck Institute of Solar System Research, April 2005

[xix] Ibid.

[xx] Kojima, M., Tokumaru, M., Fujiki, K., Itoh, H., and Murakami, T., *Origins of fast and slow solar wind*, Solar-Terrestrial Environment, Nagoya University, 2005

[xxi] Ibid.

[xxii] Ibid.

[xxiii] Ibid.

[xxiv] Akasofu, S.I., & Kamide, Y., *The Solar Wind & the Earth*, Terra Scientific Publishing Co., Tokyo, 1987, p. 25

[xxv] Phillips, T., *Sickening Solar Flares*, STEREO Science Writer's Guide, NASA Science Mission Directorate,

[xxvi] NASA Science Mission Directorate, *STEREO Instruments*, STEREO Science Writer's Guide

[xxvii] Galvin, A.B. "The Plasma and Suprathermal Ion Composition Investigation: PLASTIC Science Goals and Firsts with STEREO"

[xxviii] Ibid.

[xxix] Ibid.

[xxx] Galvin, A.B. et al., "The Plasma and Suprathermal Ion Composition Investigation: PLASTIC Science Goals and Firsts with STEREO", COSPAR, Paris, 2004

[xxxi] Ibid.

[xxxii] Galvin, A.B. et al., "The Plasma and Suprathermal Ion Composition Investigation", Turtle Bay 2005

[xxxiii] We thank the ACE SWEPAM instrument team and the ACE Science Center for providing the ACE data.

[xxxiv] Data courtesy of CELIAS/MTOF experiment on the Solar Heliospheric Observatory (SOHO) spacecraft. SOHO is a joint European Space Agency, United States National Aeronautics and Space Administration mission.

[xxxv] Data courtesy of WIND-SWE team, led by K.W. Ogilvie (NASA-GSFC), A.J. Lazarus (MIT), and M.R. Aellig (MIT).

[xxxvi] Stern, D.P., Peredo, M., "Lagrangian Points", The Exploration of Earth's Magenetosphere, NASA-GSFC, p. 21

[xxxvii] This CME catalog is generated and maintained at the CDAW Data Center by NASA and The Catholic University of America in cooperation with the Naval Research Laboratory. SOHO is a project of international cooperation between ESA and NASA.

[xxxviii] Data courtesy of the National Geophysical Data Center (NGDC), NOAA Satellite and Information Service, Solar Data Services

[xxxix] Britt, R.R., *Natural Sunblock: Sun Dims in Strange Ways*, Space.com, 2 August 2004

[xl] Data courtesy of the National Geophysical Data Center (NGDC), NOAA Satellite and Information Service, Solar Data Services

[xli] I. S. Veselovsky et al., *Solar Wind Variation with the Cycle*, Indian Academy of Sciences, J. Astrophys. Astr. (2000) 21, p. 423-429

[xlii] Data courtesy of the LASCO CME catalog

[xliii] D. N. Baker, J. H. Allen, S. G. Kanekal, G. D. Reeves, *Pager Satellite Failure May Have Been Related to Disturbed Space Environment,* American Geophysical Union, Space Physics, www.agu.org/sci-soc/articles/eisbaker.html

[xliv]Farrugia, C.J., Popecki, M.A., et al., *Wind and ACE observations during the great flow of 1-4 May 1998: Relation to solar activity and implications for the magnetosphere*, Journal of Geophysical Research, Vol. 107, No. A9, 1240

[xlv] Farrugia, C.J., et al., *Power to the Magnetosphere: May 4, 1998*, Advances in Space Research, Volume 31, Issue 4, p. 1117-1122

[xlvi] Images courtesy of SOHO/EIT, a joint mission between the ESA and NASA.

[xlvii] Ibid.

[xlviii] Walker, C., Popecki, M.A., Galvin, A.B., Farrugia, C.J., *Variations of Solar Wind Parameters: Implications for STEREO Observations*, American Geophysical Union, December 2006

[xlix] A.B. Galvin, et al., *First Results from the STEREO Plasma and Suprathermal Ion Composition Investigation*, International Union of Geodesy and Geophysics (IUGG), July 2007